Engineering protein self-assembly for biosensing applications

by

Suna Jo

B.S., Jeonbuk National University, 2014
M.S., University of Science and Technology, 2016

AN ABSTRACT OF A DISSERTATION

submitted in partial fulfillment of the requirements for the degree

DOCTOR OF PHILOSOPHY

Tim Taylor Department of Chemical Engineering
Carl R. Ice College of Engineering

KANSAS STATE UNIVERSITY
Manhattan, Kansas

2024

Abstract

Protein self-assembly is a promising bottom-up approach to create biological materials with programmable functionalities, particularly for biotechnological applications. This approach leverages engineering recombinant protein building blocks, derived from natural or artificially designed proteins, that possess distinct properties to mediate self-assembly and genetically encode specific functions. In this dissertation, we present a modular system that employs building blocks based on various protein domains and motifs that exhibit self-assembling properties or biosensing capabilities. Functional protein biomaterials were assembled through controlled protein-protein interactions and genetically encoded biosensing functionalities tailored for biomedical and environmental applications.

First, we demonstrate a protein coating self-assembly strategy that modularly incorporates functional protein domains. This system exploits the high-affinity coiled-coil interactions and liquid-liquid phase separation of proteins into coacervates. We further investigated the self-assembly conditions to enhance the density and stability of protein coatings and validated this approach across multiple substrate types. By incorporating a fluorescent calcium indicator protein GCaMP into the coating, we demonstrated calcium sensing, enabling the monitoring the calcium levels in biological fluids relevant to hypercalcemia.

Second, we explored the cooperative self-assembly of hybrid protein cages designed to encapsulate nanoparticles to control their optical properties for enhanced fluorescent biosensing of calcium ions. We employed temperature-responsive inverse phase transition of proteins to induce the formation of vesicle-like protein cages and investigated the cooperativity between the cage assembly and simultaneous encapsulation of polymer or inorganic nanoparticles. This process resulted in the formation of hybrid spheres with high-density nanoparticle encapsulation. The

hybrid cages incorporating the fluorescent calcium indicator protein OGECO-1 exhibited enhanced fluorescent signal intensity and increased sensitivity to calcium ions.

Lastly, we engineered protein-based fluorescent biosensors for nitrite detection, employing a Förster Resonance Energy Transfer (FRET) system. A nitrite-binding protein complex, NasS-NasT, was coupled with a fluorescent protein FRET pair, and the dissociation of this complex in response to nitrite binding was used to generate FRET signals for nitrite sensing in live bacteria. We extended this system into a cost-effective nitrite sensing platform by creating coating materials. Molecular docking simulations were performed to understand the binding interactions between NasS and nitrite, guiding the introduction of mutations to enhance sensitivity. Additionally, structural modeling identified promising mutations to further refine the FRET sensor, extending its applicability to detect relevant targets such as hydroxylamine.

Overall, this work demonstrates the application of protein self-assembly for constructing protein-based biomaterials and tools for biosensing. The modular self-assembly platform was designed and investigated to integrate various biosensor proteins, enabling the detection of ions relevant to healthcare and environmental monitoring. This research establishes a solid foundation for advancing in recombinant protein self-assembly for innovations in biosensor technology across diverse fields.

Engineering protein self-assembly for biosensing applications

by

Suna Jo

B.S., Jeonbuk National University, 2014
M.S., University of Science and Technology, 2016

A DISSERTATION

submitted in partial fulfillment of the requirements for the degree

DOCTOR OF PHILOSOPHY

Tim Taylor Department of Chemical Engineering
Carl R. Ice College of Engineering

KANSAS STATE UNIVERSITY
Manhattan, Kansas

2024

Approved by:

Major Professor
Won Min Park

Copyright

© Suna Jo 2024.

Abstract

Protein self-assembly is a promising bottom-up approach to create biological materials with programmable functionalities, particularly for biotechnological applications. This approach leverages engineering recombinant protein building blocks, derived from natural or artificially designed proteins, that possess distinct properties to mediate self-assembly and genetically encode specific functions. In this dissertation, we present a modular system that employs building blocks based on various protein domains and motifs that exhibit self-assembling properties or biosensing capabilities. Functional protein biomaterials were assembled through controlled protein-protein interactions and genetically encoded biosensing functionalities tailored for biomedical and environmental applications.

First, we demonstrate a protein coating self-assembly strategy that modularly incorporates functional protein domains. This system exploits the high-affinity coiled-coil interactions and liquid-liquid phase separation of proteins into coacervates. We further investigated the self-assembly conditions to enhance the density and stability of protein coatings and validated this approach across multiple substrate types. By incorporating a fluorescent calcium indicator protein GCaMP into the coating, we demonstrated calcium sensing, enabling the monitoring of the calcium levels in biological fluids relevant to hypercalcemia.

Second, we explored the cooperative self-assembly of hybrid protein cages designed to encapsulate nanoparticles to control their optical properties for enhanced fluorescent biosensing of calcium ions. We employed temperature-responsive inverse phase transition of proteins to induce the formation of vesicle-like protein cages and investigated the cooperativity between the cage assembly and simultaneous encapsulation of polymer or inorganic nanoparticles. This process resulted in the formation of hybrid spheres with high-density nanoparticle encapsulation. The

hybrid cages incorporating the fluorescent calcium indicator protein OGECO-1 exhibited enhanced in fluorescent signal intensity and increased sensitivity to calcium ions.

Lastly, we engineered protein-based fluorescent biosensors for nitrite detection, employing a Förster Resonance Energy Transfer (FRET) system. A nitrite-binding protein complex, NasS-NasT, was coupled with a fluorescent protein FRET pair, and the dissociation of this complex in response to nitrite binding was used to generate FRET signals for nitrite sensing in live bacteria. We extended this system into a cost-effective nitrite sensing platform by creating coating materials. Molecular docking simulations were performed to understand the binding interactions between NasS and nitrite, guiding the introduction of mutations to enhance sensitivity. Additionally, structural modeling identified promising mutations to further refine the FRET sensor, extending its applicability to detect relevant targets such as hydroxylamine.

Overall, this work demonstrates the application of protein self-assembly for constructing protein-based biomaterials and tools for biosensing. The modular self-assembly platform was designed and investigated to integrate various biosensor proteins, enabling the detection of ions relevant to healthcare and environmental monitoring. This research establishes a solid foundation for advancing in recombinant protein self-assembly for innovations in biosensor technology across diverse fields.

Table of Contents

List of Figures xi
List of Tables xiii
Acknowledgements xiv
Dedication xvi
Chapter 1 - Introduction 1
1.1 Principles of Protein Self-Assembly 1
1.2.1 Building Blocks for Stochastic Self-Assembly 3
1.2.2 Building Blocks for Deterministic Self-Assembly 5
1.3 Application of Protein Self-Assembly 7
1.3.1 Overview 7
1.3.2 Biosensors 8
1.3.3 Bionanocatalysts 9
1.3.4 Drug Delivery 11
1.4 Fluorescence Protein Biosensors 11
1.4.1 Overview 11
1.4.2 Calcium Indicators 12
1.4.3 Sensors for Nitrogen Compounds 13
1.5 Motivations and Objectives 15
1.6 Overview of the Dissertation 16
Chapter 2 - Self-Assembly of Microstructured Protein Coatings with Programmable Functionality for Fluorescent Biosensors 18
2.1 Background and Motivation 18
2.2 Materials and Methods 21
2.2.1 Materials 21
2.2.2 Cloning 22
2.2.3 Protein Expression and Purification 22
2.2.4 Protein Coating Assembly 23
2.2.5 Microscopy 24
2.2.6 Smartphone Imaging and Fluorescence Analysis 24

2.2.7 FT-IR characterization 25
2.2.8 Statistical Analysis 25
2.3 Results and Discussion 26
2.3.1 Self-Assembly of a Microstructured Functional Coating using Recombinant Proteins 26
2.3.2 Improvement in the Protein Coating Density and Stability for Portable Fluorescence Sensing 34
2.3.4 Calcium Sensing for the Detection of Hypercalcemia 42
2.4 Conclusion 49
Chapter 3 - Cooperative Assembly of Nanoparticle-Encapsulating Protein Cages 51
3.1 Background and Motivation 51
3.2 Materials and Methods 54
3.2.1 Materials 54
3.2.2 Cloning, Protein Expression, and Purification 54
3.2.3 Turbidity Measurement 55
3.2.4 Fluorescence Microscopy 55
3.2.5 Photocatalytic Activity Measurement 55
3.2.6 UV-Transmittance Measurement 56
3.2.7 Fluorescence Measurement 56
3.3 Results and Discussion 57
3.3.1 Encapsulation of Nanoparticles into the Vesicle-like Protein Cages 57
3.3.2 Correlation between Cage Size and Number of Nanoparticles 57
3.3.3 Kinetics of Nanoparticle Encapsulation 61
3.3.4 Encapsulation of Titanium Dioxide (TiO_2) 63
3.3.5 Enhancement of Biosensing Signals through Nanoparticle Encapsulation 65
3.4 Conclusion 67
Chapter 4 - Development of a Nitrite Sensor Based on Fluorescent Proteins 69
4.1 Background and Motivation 69
4.2 Materials and Methods 72
4.2.1 Materials 72
4.2.2 Cloning and Protein Expression 73

4.2.3 Fluorescence Measurement 73
4.2.4 Coating Fabrication 74
4.2.5 Image Analysis 74
4.2.6 *In silico* Molecular Modeling of Nitrite Sensor 74
4.3 Results and Discussion 75
4.3.1 FRET-based Measurement of Nitrite Quantification from Live Bacteria 75
4.3.2 Self-Assembly of Nitrite Sensor Coating 78
4.3.3 Molecular Docking of Nitrate and Sensor Proteins 79
4.3.4 Molecular Insights for the Design of a Hydroxylamine Sensor 82
4.4 Conclusion 87
Chapter 5 - Conclusions and Future Outlook 89
5.1 Conclusions 89
5.2 Future Outlook 90
5.2.1 Clinical Test using a Protein-Based Calcium Sensing Coating 90
5.2.2 Encapsulation of Various Types of Nanoparticles 90
5.2.3 Developing NH_2OH Sensor for Environmental Monitoring 91
References or Bibliography 92
Appendix A - Copyrights Permissions 116
Appendix B - Protein Sequences 117
Appendix C - DNA Sequences and Plasmid Maps 119
C.1 pQE60-GCAMP6m-Z_E 119
C.2 pQE60-O-GECO1-Z_E 124
C.3 pQE60-CFP-NasT/NasS-YFP 129
C.4.pQE60-CFP-NasS-YFP (CNasSY) 135

List of Figures

Figure 1.1 Illustration of strategic self-assembly approaches for highly ordered protein nanostructures.[5] 2
Figure 2.1 Schematic illustration of the self-assembly of a microstructured protein coating. 21
Figure 2.2 SDS-PAGE analysis of Z_R-ELP and GCaMP6m-Z_E. 27
Figure 2.3 A bright field micrograph of Z_R-ELP coating prepared at 42°C. 29
Figure 2.4 The microstructured protein coating assembly on the glass surfaces. 29
Figure 2.5 Confocal micrographs of mCherry-Z_E/Z_R-ELP coatings. 30
Figure 2.6 Microstructure morphology of the mCherry-Z_E/Z_R-ELP coating. 31
Figure 2.7 Relative fluorescence units (RFU) changes from mCherry-Z_E/Z_R-ELP coatings incubated in PBS at 22°C. 32
Figure 2.8 FT-IR spectrum of protein coating. 33
Figure 2.9 Protein density and stability of self-assembled EGFP-Z_E/Z_R-ELP coatings. 35
Figure 2.10 Relative fluorescence intensities from EGFP-Z_E/Z_R-ELP coatings before normalization. 36
Figure 2.11 Comparison of EGFP-Z_E/Z_R-ELP coatings from 3 and 4 cycles. 38
Figure 2.12 Cross-sectional fluorescent intensity profiles from one cycle (blue) and three cycles of protein deposition on glass substrates (red). 38
Figure 2.13 The effect of the Z_R-ELP on the protein coating assembly. 39
Figure 2.14 Quantification of protein coating using a calibration curve 40
Figure 2.15 Absorbance and fluorescence changes of soluble GCaMP6m-Z_E upon calcium ion binding. 43
Figure 2.16 The self-assembled GCaMP6m-Z_E/Z_R-ELP coating. 45
Figure 2.17 The $\Delta F/F_0$ response under hypercalcemia-related physiological conditions. 47
Figure 2.18 ΔF/F0 response from FBS with DMEM solution under hypercalcemia-related physiological conditions. 48
Figure 3.1 Cooperative self-assembly of hybrid protein cages encapsulating nanoparticles simultaneously. 53
Figure 3.2 The morphology of protein cage encapsulating PS nanoparticles. 59

Figure 3.3 Relationship between protein cages and nanoparticles 60
Figure 3.4 Absorbance changes during protein cage formation 62
Figure 3.5 Photocatalytic activity of protein-titanium dioxide (TiO_2) nanoparticle hybrid 63
Figure 3.6 Optical microscope images of TiO_2 nanoparticles coated by mCherry-Z_E/Z_R-ELP cage, Microscope images of TiO_2 nanoparticles surrounded by engineered protein cages.. 65
Figure 3.7 Analysis of OGEO1-Z_E 66
Figure 3.8 Fluorescent intensity of Z_R-ELP and OGECO1-Z_E complex with/without TiO_2..... 67
Figure 4.1 Schematic representation of aerobic ammonia oxidation during nitrification under an oxygen limiting condition. AMO, ammonia monooxygenase; HAO, hydroxylamine oxidoreductase. 70
Figure 4.2 Scheme of the FRET-based nitrite sensor development..... 72
Figure 4.3 Fluorescent intensity analysis of nitrite sensor..... 76
Figure 4.4 Fluorescent intensity analysis of CNasSY at excitation 410 nm..... 77
Figure 4.5 Analysis of nitrite protein sensor images 79
Figure 4.6 Structural analysis of NO_2^-/NO_3^- binding proteins..... 81
Figure 4.7 Modeling and molecular docking studies of the NasS-H145A mutant..... 82
Figure 4.8 Molecular docking simulation of NasS with NH_2OH 84
Figure 4.9 Molecular docking simulation of NasS mutants with hydroxylamine (NH_2OH)..... 87

Appendix Figure A.1 Copyrights for Chapter 1 from ACS Publications..... 116
Appendix Figure C.1 Plasmid map of pQE60-GCaMP6m-Z_E 119
Appendix Figure C.2 Plasmid map of pQE60-OGECO1-Z_E..... 124
Appendix Figure C.3 Plasmid map of pQE60-CFP-NasT/NasS-YFP..... 129
Appendix Figure C.4 Plasmid map of pQE60-CFP-NasS-YFP 135

List of Tables

Table 4.1 Mutation details with predicted stability change from DynaMut2. 85
Table 4.2 Affinity binding value between NasS and NH_2OH from Autodock Vina. 86

Acknowledgements

First and foremost, I extend my deepest gratitude to my Ph.D. advisor, Dr. Won Min Park. His unwavering guidance, encouragement, and support have been instrumental in the completion of this research. His mentorship and insightful advice from the inception of this project have profoundly influenced my growth as a scientist. I feel incredibly fortunate to have benefited from his expertise and dedication.

I also wish to thank my graduate committee members—Dr. John Tomich, Dr. Robert DeLong, and Dr. Ryan Hansen—for their invaluable feedback and constructive recommendations throughout my research journey. Your contributions have greatly enriched this work.

My heartfelt appreciation goes to the exceptional team of undergraduate and graduate students in the Park's Lab, as well as to collaborators such as Dr. Supreme Das, and Dr. Jeongdae Im. Working alongside such talented individuals has been a rewarding experience. Additionally, I wish to acknowledge the generous funding provided by the National Science Foundation (grant number 2239927) and the Johnson Cancer Research Center at Kansas State University. Their support has been crucial in advancing this research, and I am sincerely appreciative of their investment in this work.

I am profoundly grateful to the friends, faculty, and staff at the Tim Taylor Department of Chemical Engineering at Kansas State University for their steadfast support and for making this academic journey possible.

To my family—especially my parents, Samsik Jo and Nanchim Choi; my sister Suhyun Jo, her husband Seunggyu Kim, and their children Esol Kim; and my dearest husband, Sak Lee—I extend my deepest gratitude for your boundless love, support, and encouragement. Mom and Dad,

your sacrifices and unconditional love have been my foundation. Sak, your unwavering support has been my anchor throughout graduate school; thank you for loving and understanding me as I am and for providing invaluable answers to life's many questions to make me a better person. I am also profoundly grateful to my wonderful in-laws, Bermjae, Mikyung, Sae, Youngman, and Janghong, for their warmth and support. Being part of your family is a true blessing, and I am deeply thankful for it.

Lastly, I want to acknowledge my friends who have made my time in Kansas so meaningful. Special thanks to the Peters family (Don, Marsha, Sarah, Jay), Cassidy Booth, Bayley, and Kirby Krumsick for their steadfast companionship through all of life's ups and downs. I also appreciate Hyejin Lee and Jiyeon Kim for their sincere friendship. To my friends in South Korea, especially Bitnara Kim and Seung Joo Beak, your unwavering support and encouragement have been invaluable.

Thank you all for being an integral part of this journey.

Dedication

This thesis is dedicated to my God

To my dearest parents,

Samsik Jo and Nanchim Choi

To my beloved husband,

Sak Lee

Without whom this day would never come

Chapter 1 - Introduction

1.1 Principles of Protein Self-Assembly

Proteins are fundamental building blocks of living organisms, composed of polypeptide chains that fold into specific conformations. The folding patterns vary according to amino acid sequences, resulting in a diverse array of supramolecular architectures.[1,2] The final folded structure of a protein has intrinsic properties that drive self-assembly. For instance, hydrophobic regions within the protein tend to cluster to avoid contact with water, while hydrophilic regions remain exposed to the aqueous environment. These interactions guide the protein in forming higher-order structures or complexes. Protein folding enables the self-assembly of hierarchically organized structures[3], imparting stability, mechanical properties, and diverse biological functions.[4,5] Consequently, self-assembly is essential in biological processes that rely on constructing complex structures from simple molecular building blocks.

Protein self-assembly is primarily driven by non-covalent interactions, such as van der Waals forces, ionic interactions, and hydrophobic interactions, [6–9] These interactions work together intricately to shape the self-assembly process. As a "bottom-up approach", self-assembly is one of the two main strategies for fabricating nanomaterials, the other being the "top-down" approach.[10] While top-down methods, often associated with lithographic techniques, are widely used in microelectronics and nanostructure fabrication[11], the bottom-up approach excels in constructing complex biomolecular structures.[12–14] This method offers biocompatibility as well as exceptional precision and control over size, shape, and function, enabling the fine-tuning of bio-nanomaterial properties inherent to individual assembling molecules. Due to these advantages, protein self-

assembly has been utilized across a range of fields, including biosensors,[15,16] biocatalytic nanomaterials,[17] and disease treatment (Figure 1.1).[18,19]

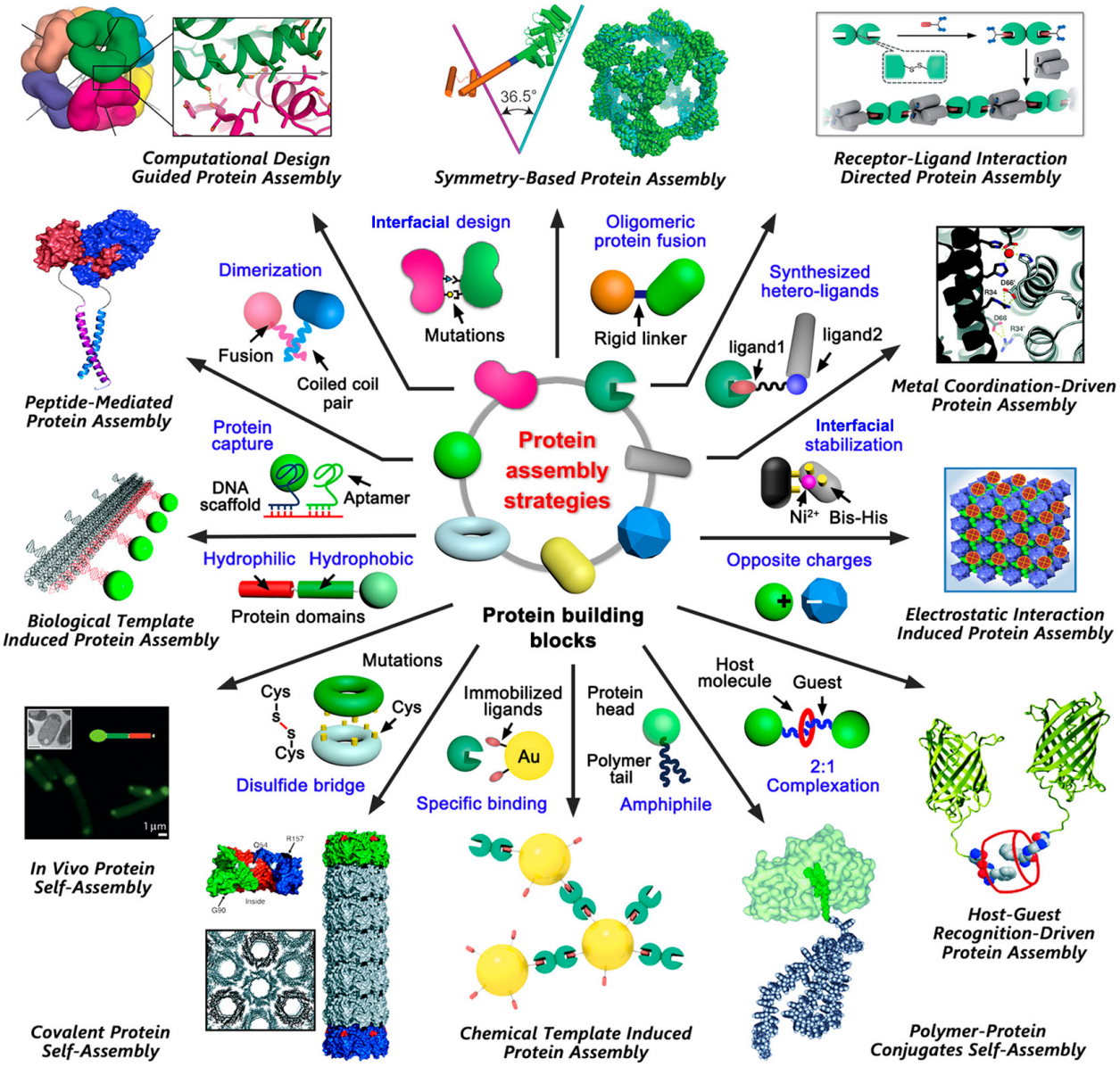

Figure 1.1 Illustration of strategic self-assembly approaches for highly ordered protein nanostructures.[5]

[Reproduced with permission from ACS Publishers; Luo et al. (2016) 8, Chem. Rev, 116, 13571-13632., © 2018]

1.2.1 Building Blocks for Stochastic Self-Assembly

Researchers have previously categorized protein-based molecular self-assembly into two main types: stochastic and deterministic.[20] Stochastic self-assembly includes various design strategies where the self-assembling protein molecules exhibit significant flexibility, leading to the formation of extended and irregular nanostructures.[21] An example of the building blocks for stochastic protein self-assembly is elastin-like polypeptides (ELPs), which are derived from endogenous human tropoelastin.[22–25] They consist of repeating V-P-G-X-G pentapeptide sequence, where X represents a variable residue. The self-assembly of ELPs depends on the transition temperature (T_t), which is influenced by factors such as solubility, hydrophobicity, and the charge of amino acid residues in the sequences.[26–28] ELPs exhibit inverse phase transition behavior in aqueous solutions: they remain as soluble below T_t, but above T_t, they undergo self-assembly to form coacervates, micelles, or vesicle structures.[29–31] This phase-transition-induced self-assembly behavior of ELPs offers promising opportunities for designing functional materials with temperature-responsive properties.

ELPs are generally biocompatible and non-toxic, making them suitable for biomedical applications, such as drug delivery systems[32], tissue engineering[33], and regenerative medicine.[34,35] Enhanced functionality can be achieved by incorporating additional biofunctional motifs into ELPs.[36,37] For example, a recombinant protein composed of keratinocyte growth factor (KGF) fused with ELPs, known as KGP-ELP, has been developed for chronic wound treatment.[36] This fusion protein self-assembles into nanoparticles, facilitating easy administration to wounds while preserving the functional characteristics of each protein domain. As a result, KGF-ELP has shown promising outcomes in enhancing wound healing in genetically diabetic mice, leading to improved epithelialization and granulation compared to controls. Similarly, the incorporation of ELPs into

other biopolymers demonstrates their versatility. For example, a conjugate of ELP with polyethylene glycol (PEG), ELP-PEG, enhanced transparency for better imaging of cells.[38] ELP-collagen, a fusion of ELP with collagen peptides, was designed to create bioactive scaffolds that can be used in tissue engineering and wound healing.[39] These ELPs leverage the unique properties of elastin, such as elasticity and temperature sensitivity, for a broad range of biomedical and industrial applications.

Drawing inspiration from natural protein motifs, amyloid-based protein building blocks have received significant interest due to relative simplicity in their sequences. They provide a biocompatible platform for the development of functional nanomaterials.[40] Amyloids and amyloid-like fibrils, characterized by their β-sheet structures, exhibit remarkable resilience to extreme conditions, including high temperatures, organic solvents, and other harsh environments.[41] A compelling example of their application is the use of a curli protein (CsgA), for microfluidic bacterial sensors after engineering it as a fusion protein. A microfluidic sensor incorporating a fusion of CsgA and DNA-binding domain (CsgA-DBD) was deposited within a microchannel. Notably, this CsgA fusion enhanced a strong signal from fluorescent bacteria detection probes upon interaction with *Escherichia coli*. Additionally, various types of amyloid-based protein building blocks were employed across diverse fields, including cell scaffolds[42], amyloid adhesives[43], and amyloid-mediated hybrid materials.[44]

Similar to amyloid-based proteins, fibrous silk structures have attracted considerable attention due to their relatively simple and synthetically accessible peptide building blocks, which are essential for both intracellular and extracellular processes.[45] These self-assembling systems, prevalent in nature, provide excellent targets for designing self-assembling peptides.[46] Silk, a structural protein produced by Lepidoptera larvae such as silkworms, spiders, and other insects,

have been extensively studied. Recombinant spider silk proteins, derived from dragline spider silk, have been studied by the Kaplan group. Their research has focused on engineered spider silks to demonstrate their unique features such as strong mechanical properties and stability compared to silkworm protein.[47,48] Spider silk exhibits exceptionally high tensile strength and remarkable toughness, often surpassing the performance of advanced artificial fibers.[49]

Another notable application of recombinant silk proteins is their use in functionalization of implant material through chemical-free, bioactive coatings. The Hedhammer group demonstrated the application of recombinant spider silk protein 4RepCT, derived from *Euprosthenops australis,* to create functional coatings on various biomaterial surfaces.[50] Protein coatings made from these recombinant silk fusion proteins exhibited cytocompatibility and stability even after exposure to organic solvents. Furthermore, when fused with a cell-binding motif, the protein promoted cell proliferation, and when combined with an antimicrobial peptide, it exhibited antimicrobial properties. The hierarchical fiber assembly of spider silk suggested that integrating it with inorganic nanoparticles could yield silk-based hybrid materials with diverse functionalities.[51] These spider silk-based hybrids showed enhanced biological and therapeutic properties, making them valuable for applications in drug delivery, cancer therapy, and tissue replacement.[48] A comprehensive understanding of spider silk could further improve the manipulation and utilization of this versatile fibrous material.

1.2.2 Building Blocks for Deterministic Self-Assembly

Deterministic self-assembly involves adopting a quaternary structure to produce distinct and precise 3D structures through either naturally evolved or precisely designed protein interfaces. Protein assemblies, naturally occurring or *de novo* designed, form through highly specific binding

interactions with various symmetries, including cyclic, helical, cubic, and lattice configurations. Among these, coiled coils are extensively studied structural protein motifs in biological systems, known for their remarkable range of geometric diversity.[52–54] Coiled coils are prevalent in transcription factors and fibrous proteins such as keratin, myosin, epidermin, and fibrinogen, and are used to construct complex protein architectures.[55] Their unique superhelical structures and programmable binding specificity have been exploited to engineer higher-order protein assembly.[56,57]

Coiled coils typically consist of a repeating pattern of hydrophobic (H) and polar (P) residues, denoted as HPPHPPP in a heptad repeat sequence (abcdefg). Most coiled coils contain four or more of these repeating units. Hydrophobic residues at the a and d positions contribute significantly to the binding affinity, which is further enhanced by ion-pairing or hydrogen-bonding interactions between polar residues at the opposing e and g positions, flanking the hydrophobic core and providing electrostatic complementarity.[53,58] The b, c, and f positions are located away from the interface. When arranged into an α-helix, the hydrophobic residues at positions a and d align to form an amphipathic structure. These amphipathic α-helices interact to sequester the hydrophobic surface (at a and d) within the helices.[59] This interaction induces a slight mismatch in periodicity between the hydrophobic residues and the α-helix structure, leading to left-handed supercoiling as the helices wind around each other.[60] This supercoiling results in a distinctive knobs-into-holes side-chain packing arrangement, which contributes significantly to the stability and structural integrity of the coiled-coil assembly.[58,61,62]

Coiled coils have been employed to build various protein structures. The method termed “coiled-coil protein origami” exploits the specific dimerization interactions between coiled coils to assemble well-defined nanostructures, such as triangles or tetrahedra.[63–65] Vesicle-like hollow

cages were also created by genetic fusion of heterodimeric coiled coils to ELPs and fluorescent proteins, followed by thermally triggered self-assembly.[29] Chemical conjugation between coiled coils was also exploited to generate self-assembled peptide nanocages (SAGEs).[66,67] In SAGEs, heterodimeric and homotrimeric coiled coils were covalently linked by disulfide bonds into peptide conjugates,[68] which initially formed a 2D hexagonal lattice structure that evolved into a well-defined hollow 3D spherical cage upon mixing. Coiled coils have also been combined with inorganic materials, such as quantum dots (QDs)[69] or metal nanoparticles.[70] Introducing QDs into hierarchical protein self-assembly enabled precise modulation of QD-based hybrid nanocarriers' properties, including size and surface potential.[69] The integration coiled coils with inorganic material holds significant potential for biomedical applications, particularly in medical imaging and targeted drug delivery.

1.3 Application of Protein Self-Assembly

1.3.1 Overview

Protein self-assembly has emerged as a groundbreaking technology with diverse applications spanning medicine to biomaterials science. By leveraging the inherent ability of proteins to spontaneously form well-defined structures, self-assembled protein biomaterials provide exceptional control over their properties and functions. In nanotechnology, they are utilized to develop high-precision nanoscale devices and sensors, taking the advantage of proteins' natural capacity to create functional nanostructures. The versatility and adaptability of self-assembled protein biomaterials for specialized applications hold great promise significant technological advancements and innovation.

Protein assemblies with diverse structures and distinct properties offer a versatile platform such as cage[71], hydrogel[72], and nanofiber.[40] By incorporating various functional components, these assemblies can be tailored for a broad range of biosensing applications.[5] An effective approach includes direct integration of specific amino acid sequences of sensor proteins into peptides or protein building blocks to program biosensing functionalities. For example, the fusion of a bacteria-binding peptide with a tetrameric coiled-coil domain, accompanied by an environment-sensitive fluorophore unit, allowed for the detection of bulky and multivalent bacterial entities.[73] This fusion protein transforms from flexible peptide chains to a rigid, rod-like helical coiled-coil conformation upon binding to bacteria. This transformation not only highlights the versatility of the technique but also demonstrates enhanced thermostability, underscoring the potential for engineering specific and robust molecular recognition. As illustrated by these examples, self-assembled proteins offer significant advantages for biosensor applications across fields. Advancements in protein self-assembly strategies will enable the development of protein-based biosensors for a broader range of biological and chemical analytes.

1.3.2 Biosensors

Biosensors are advanced technologies that integrate biological responses with electronics or optics to detect and measure specific substances or conditions. They typically consist of three key components: probe-target recognition, transduction, and physical output.[74] Transducers convert biological information into signal outputs,[75] enabling detection and monitoring through the transfer of electrons, light, or energy.[5] Biosensors are categorized based on their biological elements: affinity-based biosensors (which use receptors, antibodies, etc.) and catalysis-based biosensors (which utilize enzymes, tissues, or cells).[76] Self-assembled protein biosensors are

employed in various fields, including medical diagnostics[77], environmental monitoring[78], food safety[79], and biotechnology[80], to provide rapid, accurate, and often real-time information.[50]

For example, the Gerrard group demonstrated the application of a self-assembled nanofibril glucose biosensor application using whey proteins.[15] Post-assembly modification of whey protein nanofibrils (WPNFs) involved two chemical surface modification chemistry: biotinylation and thiolation. Biotinylated WPNFs were developed with streptavidin-coated glucose oxidase (GOx) through biotin-streptavidin interaction, known for their strong bonding in nature.[81] A glucose biosensor platform was created utilizing glucose oxidase (GOx) functionalized WPNFs as nanoscaffolds to immobilize enzymes on gold electrodes. Electrochemical characterization revealed an enhanced response with surface modification, indicating a promising increase in the biosensor's sensitivity.

An additional example of protein self-assembly for biosensing involves the fusion of two distinct coiled-coil pairs in a dimeric configuration, which is further linked to a bioluminescent enzyme, luciferase.[82] This approach based on luciferase led to the development of a genetically encoded protease sensor, utilizing protein fragment complementation techniques. This biosensor specifically targeted protease, caspase-3, employing an autoinhibitory coiled-coil strategy that resulted in an impressive 1000-fold enhancement of luminescence upon protease activation.

1.3.3 Bionanocatalysts

Designing and engineering of well-ordered protein architectures used as biocatalytic domains, particularly in facilitating enzymatic functions. The Tezcan group, for example, reported a genetically engineered metallo-β-lactamase that features an interfacial catalytic site.[83] This protein was designed through the metal-directed self-assembly of monomeric proteins into

tetramers, incorporating catalytic zinc sites at their interfaces. An engineered variant of cytochrome cb562 (RIDC), a four-helix-bundle redox protein[84], was utilized as a building block. This variant self-assembled via Zn(II) coordination, hydrophobic interactions, and disulfide bonds.[85] Some of these variants demonstrated hydrolytic activity towards ampicillin, showing *in vivo* β-lactamase activity. Further mutants of this tetrameric RIDC can be constructed to enhance enzymatic activity, with the potential applications in biomedicine.

Biological nanoreactors formed from amphiphilic protein with enzymatic activity have also been developed. Bioengineers have created a variety of self-assembling protein cages that function as biosynthetic nanoreactors.[86] These nanoreactors, employed in biocatalysis and synthetic biology, mimic natural systems to establish unique microenvironments within cells. This strategy offers several advantages, such as protecting catalyst cargo and enhancing turnover rates.[87]

A notable example of artificial protein nanoreactors inspired by natural organelles involves ketohydroxyglutarate aldolase from *Thermotoga maritima*.[88] In this case, an industrial biocatalyst, (+)-γ-lactamase, was used as a model catalyst. When fused with the engineered aldolase, the catalyst self-assembled into a dodecahedral protein nanocage. These encapsulated enzymes demonstrated enhanced pH stability compared to their unprotected counterparts and were protected from deactivation by polar organic solvents and proteolysis. Overall, this nanoreactor-based encapsulation improves the stability and efficiency of biocatalysts, making them more effective in microbial cell factories for green manufacturing.

1.3.4 Drug Delivery

Self-assembled protein biomaterials hold significant potential in biomedical applications due to their unique architecture, mechanical properties, and biocompatibility. Protein nanocontainer, with their sophisticated hollow and spherical structures, exemplify this potential.[89,90] These nanocontainers can be utilized to deliver molecular cargo, such as drugs, to cells with improved targeting capabilities.[91]

The Chilkoti group has reviewed elastin-like peptides (ELPs) as candidates for thermally triggered drug-delivery conjugates, suitable for both systemic and local administration.[92] Systemically delivered ELP–drug nanoparticles often accumulate preferentially at tumor sites due to the enhanced permeability and retention (EPR) effect, which helps reduce toxicity and improves treatment efficacy.[93] Additionally, ELP–drug conjugates can be administered with mild hyperthermia applied externally to the tumor. This approach induces ELP coacervation, which increases the local drug concentration within the tumor vasculature.[92,94]

1.4 Fluorescence Protein Biosensors

1.4.1 Overview

Fluorescent protein biosensors are biological fluorophores that change their intensity or wavelength in response to analytes, enabling imaging and real-time monitoring of molecular dynamics across both spatial and temporal dimensions.[95] These capabilities provide precise, quantitative insights into biochemical interactions and environmental changes, which are crucial for understanding and regulating complex cellular processes[96], environmental conditions[97], and medical diagnostics.[98] Fluorescent proteins have become indispensable tools across various fields, facilitating sensitive and selective detection of target analytes.[95,99–101] Nevertheless, a modular,

systematic approach to protein self-assembly using fluorescent protein biosensors would open new opportunities for enhancing their performance and versatility in various applications.

1.4.2 Calcium Indicators

Calcium ions play a critical role as intracellular and intercellular signaling messengers,[102] influencing various biological functions, including muscle contraction[103] and neuronal migration.[104] Fluorescent calcium indicators are essential for imaging of calcium ions within biological systems, providing valuable insights into cellular processes. A significant advancement in fluorescence biosensing is the development of genetically encoded calcium indicators (GECIs), which serve as fluorescent reporters in conjunction with microscopy techniques.[105,106] The GCaMPs[107,108] are prominent examples of GECIs, known for their effective calcium sensing capabilities. GCaMPs exhibit an enhanced signal-to-noise ratio due to their improved Ca^{2+} binding affinity.[109] When Ca^{2+} binds to GCaMP, the interaction between the fluorophore and the calcium-binding domain induces a conformational change in the protein, altering the chromophore's chemical environment and increasing fluorescence intensity.[110] While GCaMPs are typically green, they can be engineered to emit various colors such as red, orange, and blue, facilitating spectral multiplexing with different purposes.[106,111,112]

Another notable GECI is calcium-measuring organelle-entrapped protein indicators (CEPIA). CEPIA proteins are developed through site-directed mutagenesis in the calcium-binding domain,[113] with substitutions such as glutamate to non-acidic amino acids (E31A or E31Q) to adjust their calcium binding affinity and dynamic range. CEPIA proteins are used for simultaneous Ca^{2+} imaging, enabling researchers to monitor calcium dynamics in the endoplasmic reticulum and cytosol with high dynamic range and spatiotemporal resolution. These indicators are applicable to

various cell types, including intact neurons, providing valuable insights into cellular processes and signaling pathways.[114,115]

Aequorin is a photoprotein found in jellyfish, consisting of an apoprotein and a prosthetic group called coelenterazine, luciferin, which reacts with calcium ions.[116,117] The binding of Ca^{2+} to aequorin, which contains three EF-hand motifs typical of Ca^{2+} binding sites, induces a conformational change that leads to the oxidation of coelenterazine through an intramolecular reaction.[118] Although aequorin offers a good signal-to-background ratio, its detection can be challenging due to its low light quantum yield, meaning it emits relatively few photons per protein bound to Ca^{2+}.[119] The utility of Aequorin has been greatly enhanced by fusing it with green fluorescent protein (GFP), creating a construct known as GFP–Aequorin Protein (GAP).[120] In GAP, aequorin transfers its energy to a GFP without emitting blue light. This energy transfer occurs through radiationless excitation of GFP by activated oxyluciferin. The GFP-aequorin fusion results in a significant increase in the emitted light, which has been successfully detected in single neuroblastoma cells using an intensified charge-coupled device (CCD) camera.[121]

1.4.3 Sensors for Nitrogen Compounds

Plants display signs of nutrient deficiency when levels fall below the necessary threshold, while excessive nutrient uptake can lead to toxicity and weakness.[122] Maintaining a balanced nutrient supply is therefore crucial for optimizing crop yields. Nitrogen (N) is a vital macronutrient, often supplied in the form of nitrate (NO_3^-).[123] This process typically involves the conversion of urea to ammonium, which is then oxidized to nitrate and nitrite.[124] To be incorporated into amino acids, NO_3^- initially reduced to nitrite (NO_2^-) in the cytosol by nitrate reductase.[125,126] Subsequently, nitrite (NO_2^-) is further reduced to ammonium (NH_4^+) in plastids or

chloroplasts by nitrite reductase. Both NO_3^- and NO_2^- serve as physiological sources of nitric oxide (NO), a key biological signaling molecule.[127] The uptake and distribution of nitrate and nitrite are crucial for even human health, such as NO homeostasis and related cardiovascular functions.[128] However, tracking NO_3^- and NO_2^- molecules within plant tissue remains challenging due to insufficient spatial resolution. [129] To address this, Förster resonance energy transfer (FRET)–based genetically encoded non-invasive NO_3^-/NO_2^- biosensors have been developed.[101,129,130]

FRET is a distance-dependent phenomenon that allows detection of interactions within a Förster distance range of 1–10 nm.[131] These FRET sensors typically consist of a cyan fluorescent protein (CFP) and a yellow fluorescent protein (YFP) acting as donor and acceptor, respectively. The sensor includes a sensory domain that induces conformational changes in the protein, leading to alterations in fluorescence.[132] For example, the Uchida group developed a FRET indicator named sNOOOpy that visualizes NO_3^-/NO_2^- dynamics, providing insights into their roles in various organisms.[130] The sNOOOpy utilizes two proteins fused to different fluorescent proteins (CFP and YFP), whose spectra overlap and dissociate upon binding to target analytes. The sensitivity of sNOOOpy is not affected by small fluctuations in pH or temperature, making it reliable for quantifying NO_3^- concentrations. Another example is FLIP-NT, which monitors NO_3^- uptake in living cells in real-time with high spatiotemporal resolution.[101] The FLIP-NT nanosensor employs the popular FRET pair CFP-YFP with NrtA, the solute-binding component of the high-affinity NO_3^- ABC transporter.[133] NrtA undergoes conformational changes upon NO_3^- binding, leading to an increase in YFP fluorescence and a decrease in CFP fluorescence, enhancing FRET efficiency.

1.5 Motivations and Objectives

The field of biosensing plays a pivotal role in advancing various scientific and technological domains, ranging from healthcare to environmental monitoring. In recent years, protein self-assembly strategies have paved the way for innovative biosensing platforms with enhanced performance characteristics. Protein self-assembly can enhance functionality compared to using individual protein molecules. By combining multiple protein units into micro- or nano-architectures, these assemblies can offer improved stability, specificity, and sensitivity, making them more suitable for diverse biosensing applications.

A modular self-assembly system is essential to enable the customization and adaptation of protein biomaterials for detecting various target molecules or analytes. Additionally, challenges remain in processing proteins into materials through chemical conjugation or modification, which often have limited specificity and can cause misfolding or destabilization, leading to functional loss or aggregation. To address these issues, the projects in this dissertation focus on the rational design of recombinant proteins through genetic and modular fusion. This approach leverages protein-protein interactions for self-assembly and harnesses protein functions to create highly specific and sensitive biosensors, potentially overcoming the limitations of conventional methods.

The overall goal of the proposed work is to engineer recombinant protein self-assembly systems and apply them in the creation of biosensor platforms. This focus is on developing modular and generalized systems that integrate functional sensing protein domains into protein assemblies, which will be used for detecting metal ions and small molecules relevant to healthcare and environmental applications. To achieve the goal, three objectives are established: (Objective 1) Design and produce recombinant protein building blocks that self-assemble into functional protein coating and demonstrate fluorescent sensing of calcium ions, (Objective 2) Investigate protein-

hybrid self-assembly to enhance biosensing performance, and (Objective 3) Expand protein self-assembly in both cells and coatings for environmental monitoring applications.

1.6 Overview of the Dissertation

This dissertation describes the approaches to engineering protein self-assembly for biosensor applications. Three independent studies were designed and conducted, each aligned with the overarching goal of demonstrating protein self-assembly to create protein biomaterials with genetically programmed functionalities for biosensing.

Chapter 2 introduces a microstructured coating self-assembly platform for calcium sensing. This method leverages the modular design of recombinant proteins to create protein coatings with programmable functionalities. By utilizing these self-assembled coatings, we developed a portable fluorescent biosensor device capable of smartphone-based detection of calcium levels, particularly relevant to hypercalcemia. **Chapter 3** describes a fundamental study of the self-assembly of protein cages that encapsulate high-density nanoparticles with enhanced performance for calcium sensing. The cooperative interaction between cage assembly and nanoparticle encapsulation was investigated to elucidate the underlying mechanism. This system was designed to improve the optical properties of fluorescent protein cages, enhancing their utility in biosensor applications. In **Chapter 4**, a biosensing strategy using genetically encoded FRET sensor proteins is described for nitrite detection in environmental monitoring. Utilizing the sensor proteins, we measured nitrite levels within live *E. coli* cells, and cell extracts were further employed to develop a cost-effective, straightforward protein coating for nitrite sensing. Molecular docking simulations were also conducted to examine nitrite-protein interactions, providing insights into improving binding affinity and tailoring specificity for related targets.

Overall, this dissertation provides a comprehensive examination of the design and application of self-assembled protein biomaterials, showcasing their versatility and potential to address key challenges in science and industry.

Chapter 2 - Self-Assembly of Microstructured Protein Coatings with Programmable Functionality for Fluorescent Biosensors*

2.1 Background and Motivation

Proteins have been exploited to build coating materials for a variety of applications in food packaging,[134,135] drug delivery,[136–139] tissue engineering,[140–142] biosensors,[41,143–145], biological adhesives,[146] and regenerative medicine.[136] Protein coatings offer a promising approach for creating functional surfaces with tailored properties such as antifouling activity[147,148], selective binding affinity[149], and controlled release of therapeutics,[150,151] controlled interactions of nanoparticles with cell membrane,[138,139] and modulation of energy transfer for biosnesing.[145] Such functional coatings include amyloid-based genetically modified protein coatings created via self-assembly, whose functionalities were programmed for biotemplating,[152] biocatalysis,[153] and bacterial sensors.[41] Recombinant curli nanofibers were engineered to create biofilms with biocatalytic functions, where the curli nanofibers enabled modular and site-specific enzyme immobilization.[154,155] In coating fabrication, microstructure formation has a significant impact on functionality and performance. Mechanical or physical properties of protein coating materials have been modulated through the control of microstructures, [41,156–158] which are influenced by the conformation, binding interaction, and topology of protein building blocks. An example is thin solid films of protein-block copolymer conjugates in which microphase-separated structures yielded high protein loading and biocatalytic activity.[159,160] Another example includes a

* Reproduced with permission from Jo, Suna, Erin Pearson, Donghoon Yoon, Jungkwun Kim, and Won Min Park. "Self-assembly of microstructured protein coatings with programmable functionality for fluorescent biosensors." *bioRxiv* (2024): 2024-05.[269] Copyright 2024.

superhydrophobic coating with microstructures, which were manipulated by the phase transition of lysozyme.[158] This coating presented excellent mechanical and thermal stability and the capability to drive protein crystallization.

Recombinant proteins have been used as versatile building blocks that present excellent programmability to self-assemble biomaterials, including coating materials.[159,161] Multiple genes can be recombined genetically and modularly to introduce self-assembling properties as well as a variety of functionalities, followed by protein expression and purification using well-established protocols.[161] Despite their genetic programmability, processing protein materials is often required through chemical modifications using organic solvents[162–164] or chemical reagents for covalent substrate attachment or cross-liking or conjugation with block copolymers.[159,164].[159,164] These additional steps along with additional washing or functionalization in protein coating fabrication present challenges in manufacturing process development and may limit functionality due to potential protein denaturation. Moreover, production of recombinant curli nanofibers is challenging, particularly when multiple functional domains need to be introduced.[154,155] Thus, a system of recombinant protein coating assembly under biocompatible conditions would be desirable for highly functional coating material development.

In this study, we demonstrate the self-assembly of modular, biocompatible protein coatings with genetic programming of functions and properties. We exploited two distinct protein motifs, an elastin-like polypeptide (ELP) and high-affinity coiled coils, to achieve coating assembly on a variety of substrate materials, manipulate microstructured morphology for high surface area, and incorporate globular functional domains to protein coatings. ELPs are tropoelastin-derived biomimetic peptides that undergo a thermally triggered liquid-liquid phase separation. The inverse phase transition results in the formation of insoluble coacervates from soluble proteins in an

aqueous solution.[165] Coiled coils are the α-helices that bind to each other to form a super-helical bundle. Because of their exceptional binding affinity and specificity, coiled coils have been used to program protein assemblies in various systems.[63–65] We recombined ELP, coiled coils, and functional protein modules into fusion protein building blocks that form a coating material through a simple, chemical-free, and water-based process under biocompatible conditions (Figure 1).

We used this coating platform to fabricate a smartphone-based biosensor device for the detection of hypercalcemia. Current calcium biosensors, include photonic polymers and[166,167] functionalized nanoparticles[168,169] which provide millimolar resolution, as well as chemical fluorescence indicators[170–172] and microelectrodes.[173] While chemical fluorescent indicators like fura-2[170] and rhod-5N[171] are widely used to quantify Ca^{2+} in micromolar concentrations, they often experience non-specific binding and interference from other cations such as Na^{+}, K^{+}, Mg^{2+}. Microelectrodes, although capable of a wide dynamic range and stable voltage readings with a sub-nanomolar resolution,[173] are limited by their slow response to calcium changes and susceptibility to fouling, which may hinder real-time monitoring.[174,175] To address these limitations, we exploited a genetically encoded fluorescent calcium ion indicator, GCaMP, which provides high specificity for calcium ions and rapid response times.[108] We integrated GCaMP into a protein coating such that the coating exhibits fluorescence dependent upon the concentration of Ca^{2+}. Employing a light-emitting diode (LED) transilluminator and smartphone camera, we measured the fluorescence from the protein coating and quantified the Ca^{2+} concentrations in biological fluids (0.5 to 3 mM) that are relevant to mild and moderate hypercalcemia. This approach offered a simple and low-cost solution suitable for resource-limited settings.

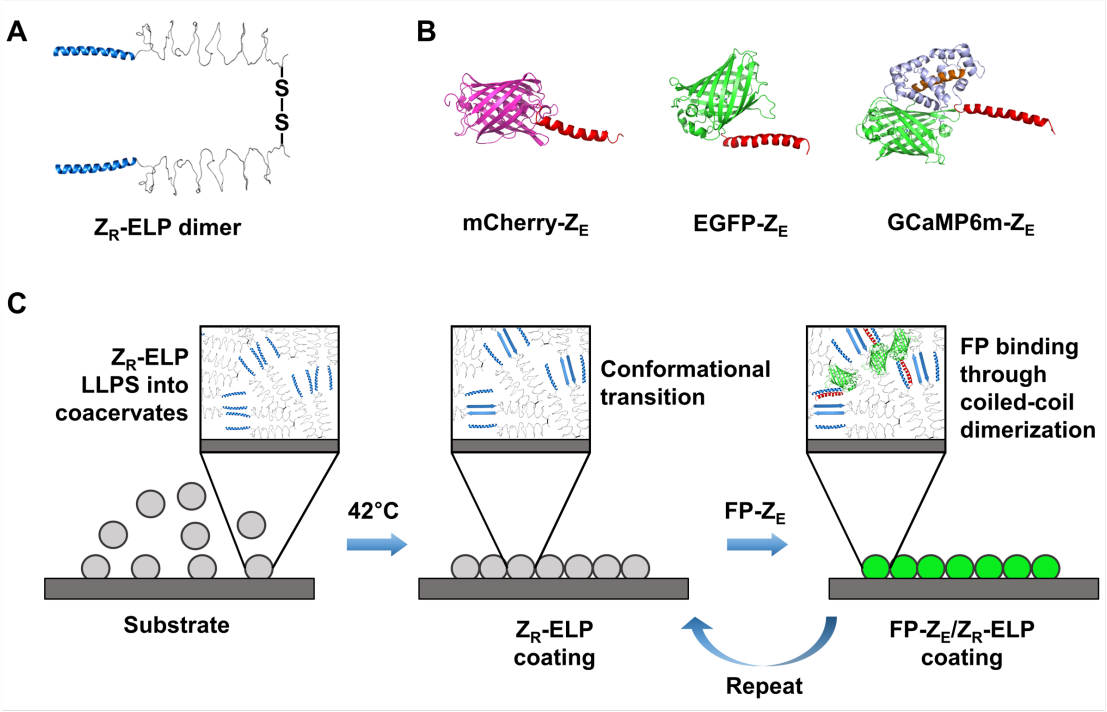

Figure 2.1 Schematic illustration of the self-assembly of a microstructured protein coating.

(A) The dimeric topology of Z_R-ELP formed through a disulfide bond. (B) Three recombinant fluorescent proteins fused with a coiled-coil tag (FP-Z_E): mCherry-Z_E, EGFP-Z_E, and GCaMP6m-Z_E. (C) Coating self-assembly process: The microstructures are initially formed through the liquid-liquid phase separation (LLPS) of the Z_R-ELP protein. These coacervates from LLPS adhere to surfaces and become interconnected. The structural changes associated with the transition of coiled-coil α-helices (Z_R) to β-sheets at 42°C stabilize the microstructures of the coating. Upon incubation, FP-Z_E binds to the Z_R domains within the microstructures through strong coiled-coil dimerization of Z_E and Z_R, resulting in fluorescent protein coatings. This process is repeated to control the density of proteins within a coating.

2.2 Materials and Methods

2.2.1 Materials

The *E. coli* strain T7 Express *lysY/I*^{q} (BL21 derivative) was purchased from New England Biolabs. The plasmids, pQE60_Z_E/Z_R-ELP, pQE60_mCherry-Z_E, and pQE60_EGFP-Z_E, were kindly provided by Prof. Julie Champion at the Georgia Institute of Technology. Nickel nitrilotriacetic acid resin (Ni-NTA, HisPur™) was purchased from Thermo Scientific. $CaCl_2$ was

purchased from EMD Millipore Corporation. PBS (1X, pH 7.4) containing NaCl (137 mM), KCl (2.7 mM), NaH_2PO_4 (10 mM), KH_2PO_4 (1.8 mM), and TBS (1X, pH: 7.4) containing tris base (50 mM) and NaCl (150 mM) were prepared in the lab. Tyrode's solution was made from lab containing NaCl (135 mM), KCl (2.8 mM), $CaCl_2$ (2 mM), $MgCl_2$ (1 mM), NaH_2PO_4 (400 μM), $NaHCO_3$ (12 mM), Glucose (5.5 mM), HEPES (10 mM) and BSA. BSA, FBS, and DMEM were purchased from Thermo Scientific. The substrate materials of glass (0.14 mm thick), PET (0.125 mm thick), and PMMA (1.0 mm thick) were purchased from Globe Scientific Inc., Calpalmy, and Langaelex, respectively.

2.2.2 Cloning

The DNA sequences encoding GCaMP6m [110,111] and the Z_E domain[176] were recombined to create a construct encoding GCaMP6m-Z_E. The gene fragment was synthesized, ligated into the *NcoI* and *BglII* restriction sites of the pQE60 vector (3.4kbp), and sequence-verified by GenScript. The resulting plasmid pQE60_GCaMP6m-Z_E was inserted into T7 Express chemically competent cells.

2.2.3 Protein Expression and Purification

The sequence of recombinant fusion proteins, Z_R-ELP, mCherry-Z_E and EGFP-Z_E are available in Table S1. The recombinant proteins mCherry-Z_E, EGFP-Z_E, and GCaMP6m-Z_E were expressed and purified as previously described.[177,178] Briefly, the cells transformed with the plasmids pQE60_mCherry-Z_E, pQE60_EGFP-Z_E, or pQE60_GCaMP6m-Z_E were grown at 37°C overnight in 2X yeast extract and tryptone media supplemented with 200 mg/L ampicillin. Overnight protein expression (for 18 hours) was induced at the optical density of 0.8 (at 600 nm)

by adding 1.0 mM of isopropylthio-β-galactoside. After the harvest, cells were lysed with a buffer containing 50 mM Na_2HPO_4, 300 mM NaCl, and 10 mM imidazole and went through a freeze-thaw cycle and sonication. Insoluble parts were removed by centrifugation (10,000 rpm) and the cleared lysate was incubated with Ni-NTA. Then, the recombinant proteins mCherry-Z_E, EGFP-Z_E, or GCaMP6m-Z_E were eluted in a buffer containing 250 mM imidazole after washing. The eluted solution was dialyzed in the 1X TBS. Z_R−ELP was expressed following the same protocol described above and then purified under a denaturing condition using Ni-NTA.[177,178] The expressed complex of His_6Z_E and Z_R-ELP from harvested cells was resuspended in a buffer containing 6 M urea, and the cleared lysate was incubated with Ni-NTA resin. After washing, 6 M guanidine hydrochloride was used to elute Z_R-ELP from His_6-Z_E bound on the resin. Purified Z_R-ELP was dialyzed into deionized water. The purity and molecular weight of proteins were confirmed by sodium dodecyl sulfate-polyacrylamide gel electrophoresis, followed by time-of-flight mass spectrometry (Waters Xevo G2/XS coupled with nano-ESI). Fluorescence of purified mCherry-Z_E, EGFP-Z_E, and GCaMP6m-Z_E and turbidity of Z_R-ELP coacervates were analyzed by BioTek SYNERGY H1 microplate reader.

2.2.4 Protein Coating Assembly

Micropillar arrays were fabricated by ultraviolet light emitting diode (UV-LED) lithography, which was made using a photosensitive polymer resin.[179] Substrates (glass, PET, PMMA, and aluminum), as well as the microfabricated micropillar arrays, were prepared on a heating block at 42℃. A 20 µl drop of Z_R-ELP (1.7 mg/ml) was placed and dried on the substrates, followed by incubation with a solution containing 6µM of mCherry-Z_E, EGFP-Z_E, or GCaMP6m-Z_E. These steps were repeated up to three times. The substrates were washed twice with 2X PBS.

For a coating of GCaMP6m-Z_E/Z_R-ELP, a solution of GCaMP6m-Z_E was prepared in 100 μM NaCl solution containing 100 μM EDTA. All coatings were dried at room temperature and rinsed with TBS twice for use. For GCaMP6m-Z_E/Z_R-ELP, we stored dried protein coatings at 4°C overnight before use.

2.2.5 Microscopy

Protein coatings were imaged by Olympus IX-73 or Axio Carl Zeiss Observer.Z1 fluorescent microscope with a 40X objective at filter settings of excitation 532 nm/emission 610 nm (mCherry-Z_E) and excitation 488 nm/emission 526 nm (EGFP-Z_E). Confocal microscope images were captured using a Zeiss LSM 510Vis system with a 100X oil immersion objective with laser wavelengths of 543 nm, using a BP 565−615 emission filter. The surface morphology of mCherry-Z_E/Z_R-ELP coating was imaged with a Zeiss Ultra60 FE-SEM. The coating samples were fixed on a glass substrate using 1.0% glutaraldehyde for 1 hour, washed twice with deionized water, and subsequently freeze-dried and sputter-coated with gold and imaged at 5 kV.

2.2.6 Smartphone Imaging and Fluorescence Analysis

The coatings of GCaMP6m-Z_E/Z_R-ELP or EGFP-Z_E/Z_R-ELP were placed under an LED transilluminator (BT Lab Systems) and excited at the wavelength of 470 nm. An iPhone 13 (Apple, Inc.) smartphone with a rear camera (4000x3000 pixels) was used to record fluorescence images, which were analyzed by ImageJ. Fluorescence intensity in the green channel of the images was quantified and subtracted by the intensity of background fluorescence. The quantified intensities were normalized by the background intensity and averaged by area. An equally sized area from

each image was selected for the analysis. The relative changes in fluorescent intensity of the protein coating samples in response to Ca^{2+} exposure is calculated using the following equation:

$$\Delta F/F_0 = (F - F_0) / F_0$$

where F_0 represents the initial fluorescent intensity of the protein coating, and F denotes the fluorescent intensity after the addition of Ca^{2+}.

2.2.7 FT-IR characterization

The FT-IR spectra were recorded on an Agilent Cary 630 FT-IR spectrometer. A 10 µL of Z_R-ELP coacervate solution in PBS was deposited on a glass substrate at 42°C. After drying, the Z_R-ELP coating was directly applied to the attenuated total reflection diamond crystal, with the glass substrate serving as a background. Data were analyzed using Agilent MicroLab software, followed by baseline correction and spectrum deconvolution of the amide I peak (1590–1710 cm^{-1}) performed using Microsoft Excel.

2.2.8 Statistical Analysis

Fluorescence recovery responses ($\Delta F/F_0$) were analyzed by one-way analysis of variance (ANOVA) with Tukey's post-hoc multiple comparisons or student t-test for two-group comparison. All statistical analysis was conducted using Microsoft Excel. The p values ≤ 0.05 were considered statistically significant (*$p \leq 0.05$, **$p \leq 0.01$, ***$p \leq 0.005$, ****$p \leq 0.001$, N.S.; not significant).

2.3 Results and Discussion

2.3.1 Self-Assembly of a Microstructured Functional Coating using Recombinant Proteins

We exploited two distinct types of protein-protein interactions to self-assemble microstructured coating materials and genetically program functionality. A pair of heterodimeric coiled-coil proteins (Z_E:Z_R, colon denotes heterodimerization) with a high-affinity binding interaction (dissociation constants $K_D \sim 10^{-15}$ M) [176,178] were fused to fluorescent proteins (FPs) or an ELP to construct recombinant fusion proteins, Z_R-ELP and FP-Z_E (Figures 2.1.A and 2.1.B).[178] While an ELP triggers the self-assembly of protein-rich coacervates through a thermally responsive inverse transition,[26,178,180] the coiled coils Z_E and Z_R mediate strong binding between FP and ELP coacervate. This self-assembly system using FP-Z_E and Z_R-ELP has been exploited to create protein particles in a hydrogel,[177] hollow protein vesicles[178,181,182], and sheet structures.[183]

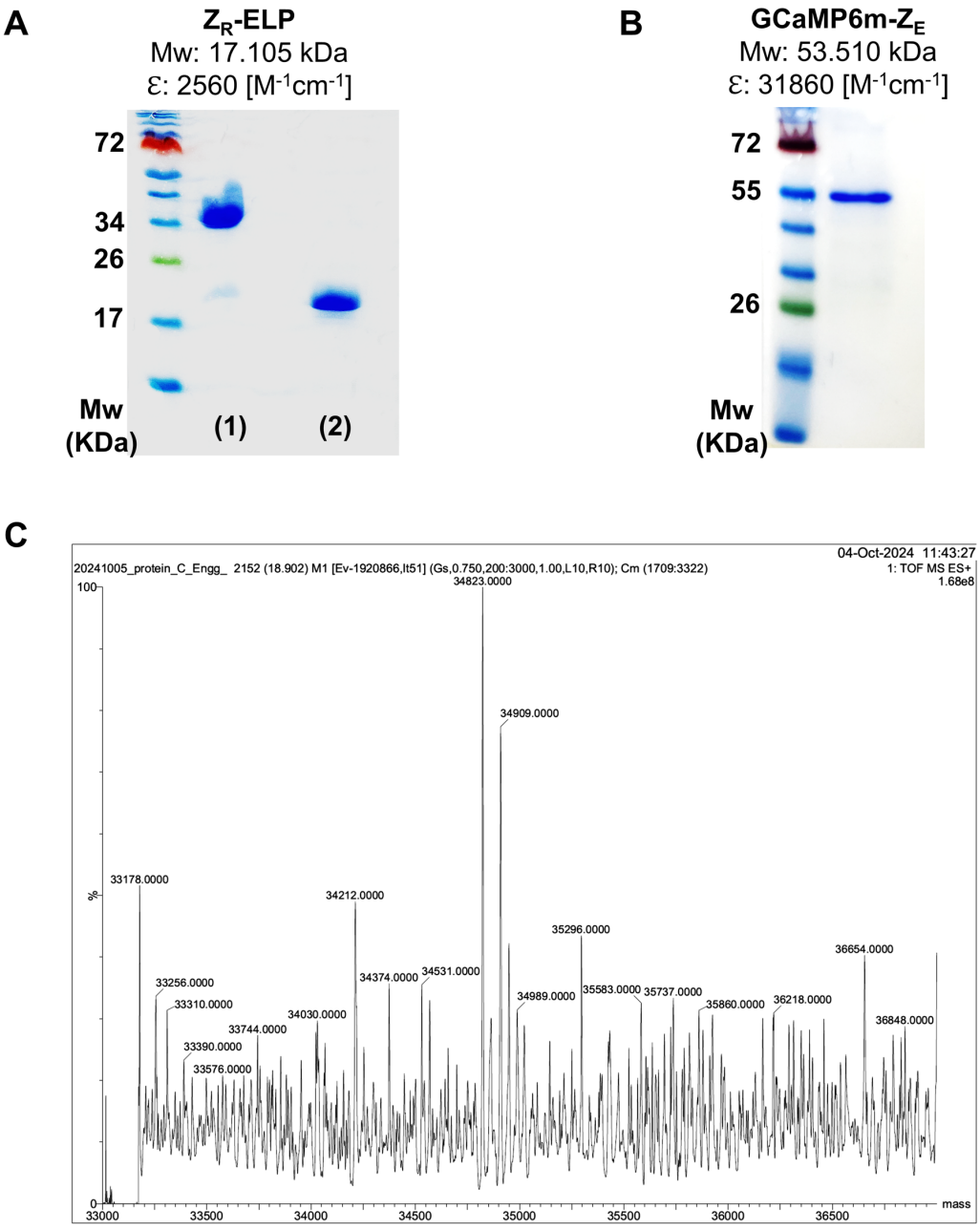

Figure 2.2 SDS-PAGE analysis of Z_R-ELP and GCaMP6m-Z_E.

(A) The gel of Z_R-ELP samples prepared in the absence (1) or presence of the reducing agent β-mercaptoethanol (2). (B) The gel of purified GCaMP-Z_E. The theoretical molecular weights (Mw) and extinction coefficients (ε) are provided on top of each gel image. (C) Mass of covalently conjugated Z_R-ELP dimer shown in lane (1) of the gel (A) measured by TOF mass spectroscopy.

We expressed and purified a covalently linked Z_R-ELP dimer for protein coating self-assembly (Figure 2.1A and Figure 2.2). A disulfide bond at the C-terminal of ELP joins the fusion protein Z_R-ELP to one another, linking the two Z_R domains through an ELP_2 linker (Z_R-ELP_2-Z_R). We hypothesized that this topology is essential for the interconnection of Z_R-ELP coacervates, which can grow into microstructured coating layers. First, we demonstrated the self-assembly of a fluorescent coating using a red fluorescent protein, mCherry. Fluorescent proteins are robust and easy to characterize, thus ideal for characterizing the self-assembly process. Additionally, many genetically encoded fluorescent biosensors, such as GCaMP, share structural similarities with mCherry, making them excellent model proteins to demonstrate the general applicability of our system. The Z_R-ELP coacervates prepared in phosphate-buffered saline (PBS) at 25°C were first placed on a glass substrate, incubated at 42°C, and dried. The turbidity of the glass substrate measured at the wavelengths from 300 nm to 500 nm indicates the formation of a microstructured protein coating, which was stably adhered to the glass surface after an hour of incubation with PBS (Figure 2.4.A and 2.3). Then, the coating of Z_R-ELP was further incubated with a solution of recombinant fusion protein mCherry-Z_E and washed. The fluorescence emission at 610 nm (excited at 532 nm) indicates the incorporation of mCherry-Z_E into the protein coating (Figure 2.4.B), which was through the affinity binding interaction between Z_E and Z_R domains. The fluorescent and confocal micrographs (Figure 2.4.C and Figure 2.5) showed the interconnection between coacervates, which resulted in the formation of microstructures adhered to glass. The fluorescence in the images (emission: 610 nm, excitation: 532 nm) further confirmed the attachment of mCherry-Z_E to the microstructured coating.

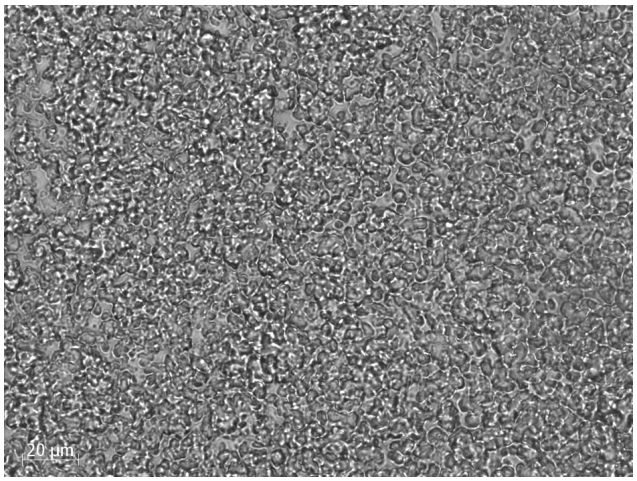

Figure 2.3 A bright field micrograph of Z_R-ELP coating prepared at 42°C.

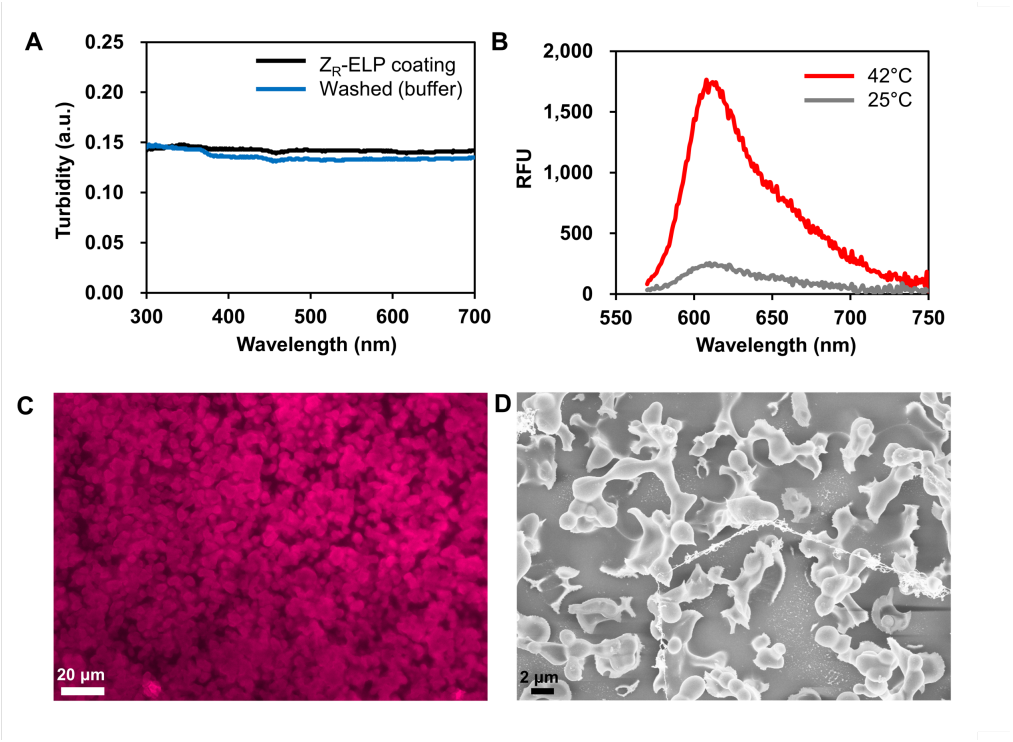

Figure 2.4 The microstructured protein coating assembly on the glass surfaces.

(A) Turbidity profile of Z_R-ELP coating on glass (black) and incubated in buffer for 1 hr (blue). (B) Relative fluorescence unit (RFU) of mCherry-Z_E/Z_R-ELP coating prepared at 42°C (red) and 25°C (gray). (C) A fluorescence micrograph of mCherry-Z_E/Z_R-ELP coating prepared at 42°C. (D) A FESEM image of mCherry-Z_E/Z_R-ELP coating from panel C.

A high-resolution image acquired using a field emission scanning electron microscope (FESEM) also shows the microstructured morphology of the protein coating on glass (Figure 2.4.D and Figure 2.6.A). The morphology of interconnected microspheres at the size of 1.6 ± 0.5 μm was observed according to the image analysis (Figure 2.6.B). This length scale was slightly higher than the hydrodynamic diameter of mCherry-Z_E/Z_R-ELP coacervates measured in an aqueous solution (~ 0.8 μm, Figure 2.6.C), which would be due to coalescence and growth of the coacervate microspheres on substrates. The result evidences that the microstructures evolved from the partial coalescence between the coacervate microspheres. We hypothesize that while the phase-separated coacervates undergo complete coalescence process in solution phase,[184,185] those deposited on surfaces may experience kinetic hinderance, resulting in the formation of interconnected microstructures. The microstructured protein coating was stably deposited on glass without covalent conjugation or any pretreatment of the glass surfaces.

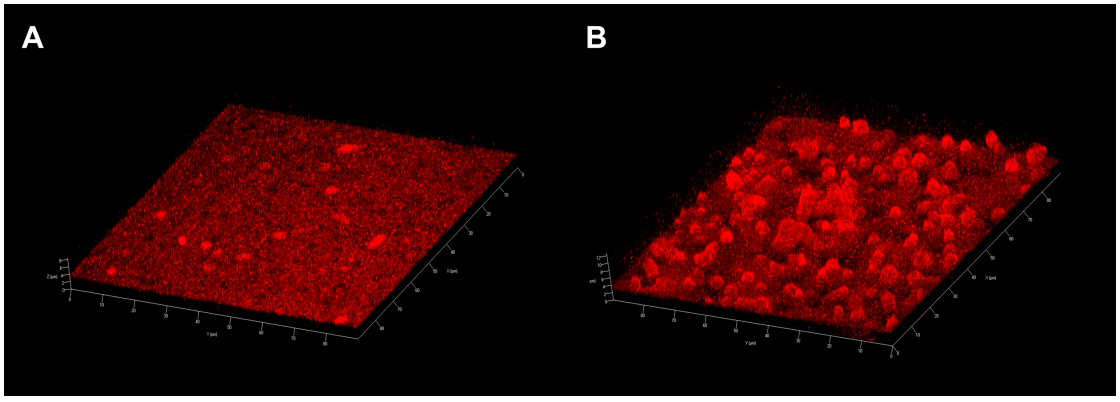

Figure 2.5 Confocal micrographs of mCherry-Z_E/Z_R-ELP coatings.
Images of mCherry-Z_E/Z_R-ELP coatings on glass substrate were obtained from protein incubation at 25°C (A) and at 42°C (B).

The formation of microstructures was critically influenced by temperature. In the coating sample prepared at 25°C, the formation of microstructures was not observed (Figure 2.5). Moreover, a remarkably lower fluorescence intensity was measured from the coating (Figure 2.4.B). The microstructures are initially formed through the liquid-liquid phase separation of Z_R-ELP in solution, which adhere to surfaces and become interconnected (Figure 1). While this process is driven by reversible hydrophobic interactions in the ELP domain, the interconnected microstructures remained stable over time.

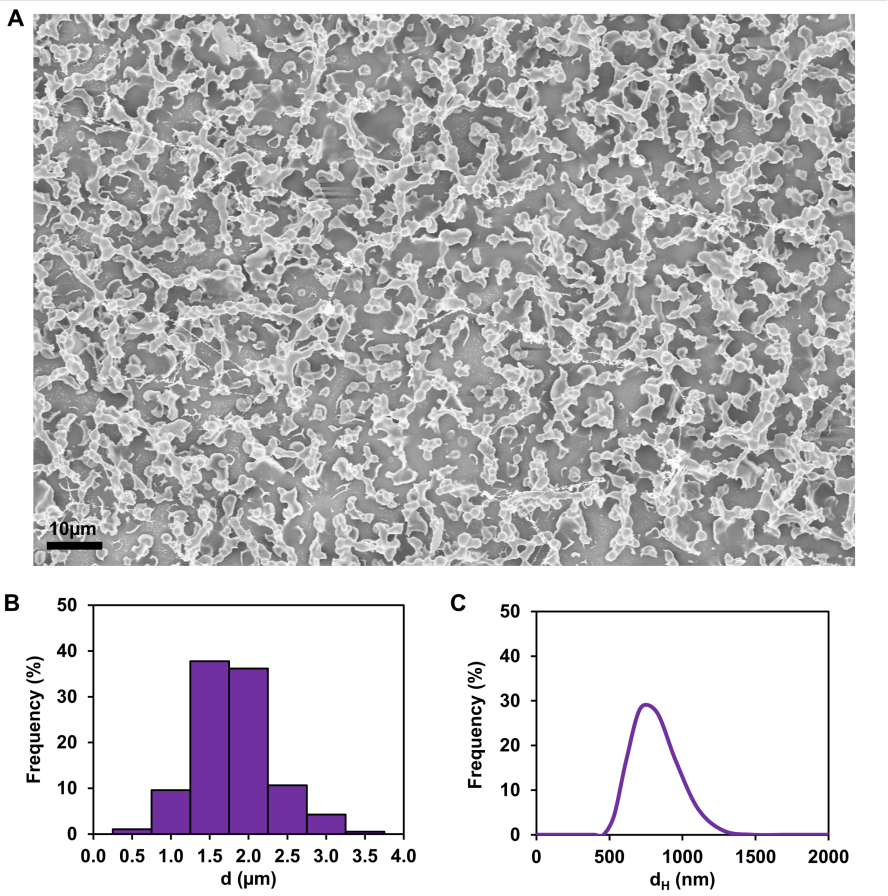

Figure 2.6 Microstructure morphology of the mCherry-Z_E/Z_R-ELP coating.

(A) A FESEM image. (B) The size distribution of the coating microstructures is shown in panel (A). (C) The size distribution of mCherry-Z_E/Z_R-ELP coacervates in solution measured by dynamic light scattering.

This could be due to a significant reduction in the surface area of the coating as a result of no microstructure formation. This is likely caused by structural transformation from α-helix to β-sheet within the coiled coils (Z_R), a change previously observed during heating, drying, or long-term storage of coiled coils in buffer solutions.[186] This transformation is irreversible and helps stabilize the microstructures of the coating (Figure 2.7). In the absence of β-sheet formation, the microstructures may revert to a soluble protein phase. Therefore, we hypothesize that the conformational transformation is facilitated near the melting temperature of Z_R homodimer (44°C)[176], serving a critical role in stabilizing the interconnected coacervates.

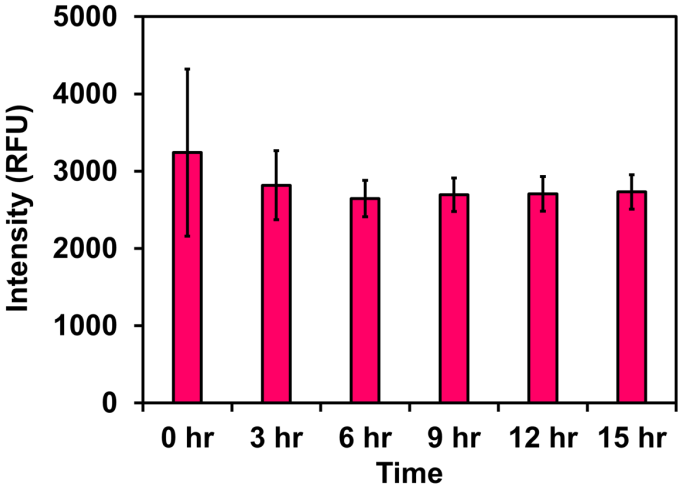

Figure 2.7 Relative fluorescence units (RFU) changes from mCherry-Z_E/Z_R-ELP coatings incubated in PBS at 22°C.

The Fourier Transform infrared (FT-IR) spectrum of the Z_R-ELP coating showed reduced α-helix content and an increased fraction of β-sheet structures, indicating the transition of the secondary structure (Figure 2.8). The deconvoluted FT-IR spectrum in the amide I region (1600-1700 cm^{-1})[187] exhibits a peak at around 1657 cm^{-1}, with a relative area of 0.917, indicate the presence of 13% α-helix structures. The peaks at 1622 cm^{-1} and 1635 cm^{-1} indicate 30% β-sheet structures, with relative areas of 0.962 and 1.185, respectively. In contrast, according to the circular

dichroism spectra of soluble Z_R-ELP at 25°C, the α-helix content is 35.1% and the β-strand is 13.5%, respectively.[177] The results evidence the structural transformation of Z_R during the coating assembly. (Figure 2.8.B)

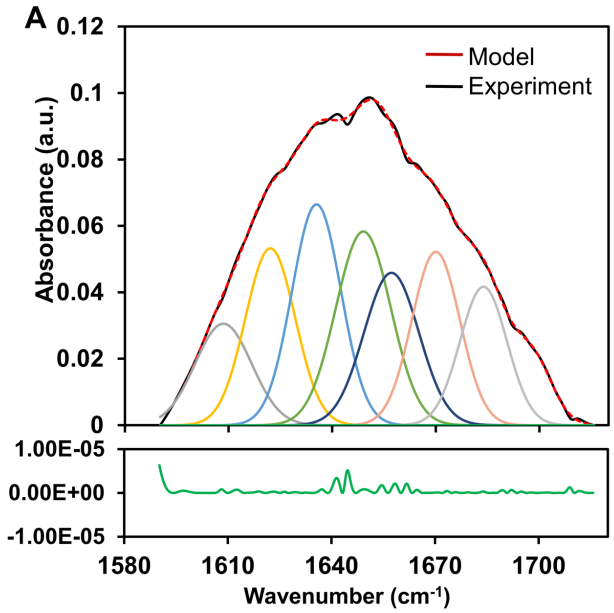

Secondary structure	Peak position (cm^{-1})	Relative area
β-sheet aggregates/extended strand	1608	0.627
β-sheet	1622	0.962
β-sheet	1635	1.185
Random coil	1649	1.161
α-helix	1657	0.917
3(10)-helix/β-turn	1670	0.910
β-turn	1683	0.711
β-sheet/ β-turn	1698	0.270

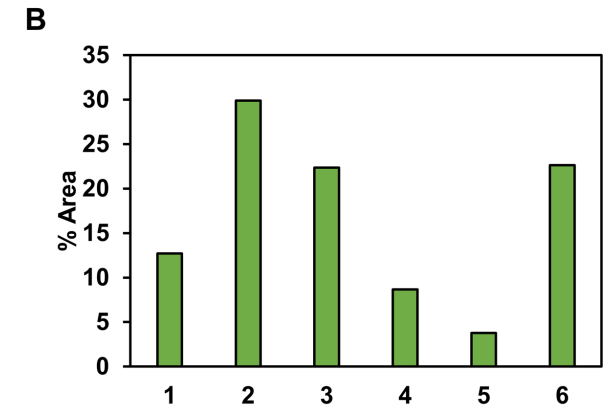

#	Secondary structure	% area
1	α-helix	12.7
2	β-sheet	29.8
3	Random coil	22.3
4	β-sheet aggregates/extended strand	8.6
5	β-sheet/ β-turn	3.7
6	β-turn	22.6
	sum	100

Figure 2.8 FT-IR spectrum of protein coating.

(A) Deconvolution of amide I band in FT-IR spectrum of Z_R-ELP coating **at 42°C** (1600 -1700 cm^{-1} region) using a model fit (shown in red). The fitting error is below the spectrum (green) and individual components are assigned to secondary structures and relative areas are indicated in the table (right). (B) The secondary structure of Z_R-ELP coating was analyzed from the deconvolution data.

2.3.2 Improvement in the Protein Coating Density and Stability for Portable Fluorescence Sensing

As confirmed in Figure 2.4, fluorescence from the microstructured protein coating can be quantified or imaged using a spectrofluorometer or microscope. Nonetheless, a portable fluorescent biosensor application would require a simple and low-cost fluorescence reader such as a smartphone camera equipped with a light-emitting diode (LED) and filter. For this to work, the density of protein coatings on a device should be high enough to emit strong quantifiable fluorescence. To increase the protein density, we repeated the steps of coating assembly and deposition (Figure 2.1C). In addition to mCherry, we used the green fluorescent protein EGFP as a model to also demonstrate the modularity of our system. A droplet of Z_R-ELP solution was placed and dried on a glass surface at 42°C, followed by incubation with a solution of EGFP-Z_E.[178] This process was repeated for up to four cycles, followed by quantification of fluorescence from EGFP using a portable LED transilluminator and smartphone camera (Figure 2.9, Figure 2.10.A, and Figure 2.10.B). As a result, the intensity of green fluorescence after three cycles of protein deposition was increased by more than 100% than a single-deposition process.

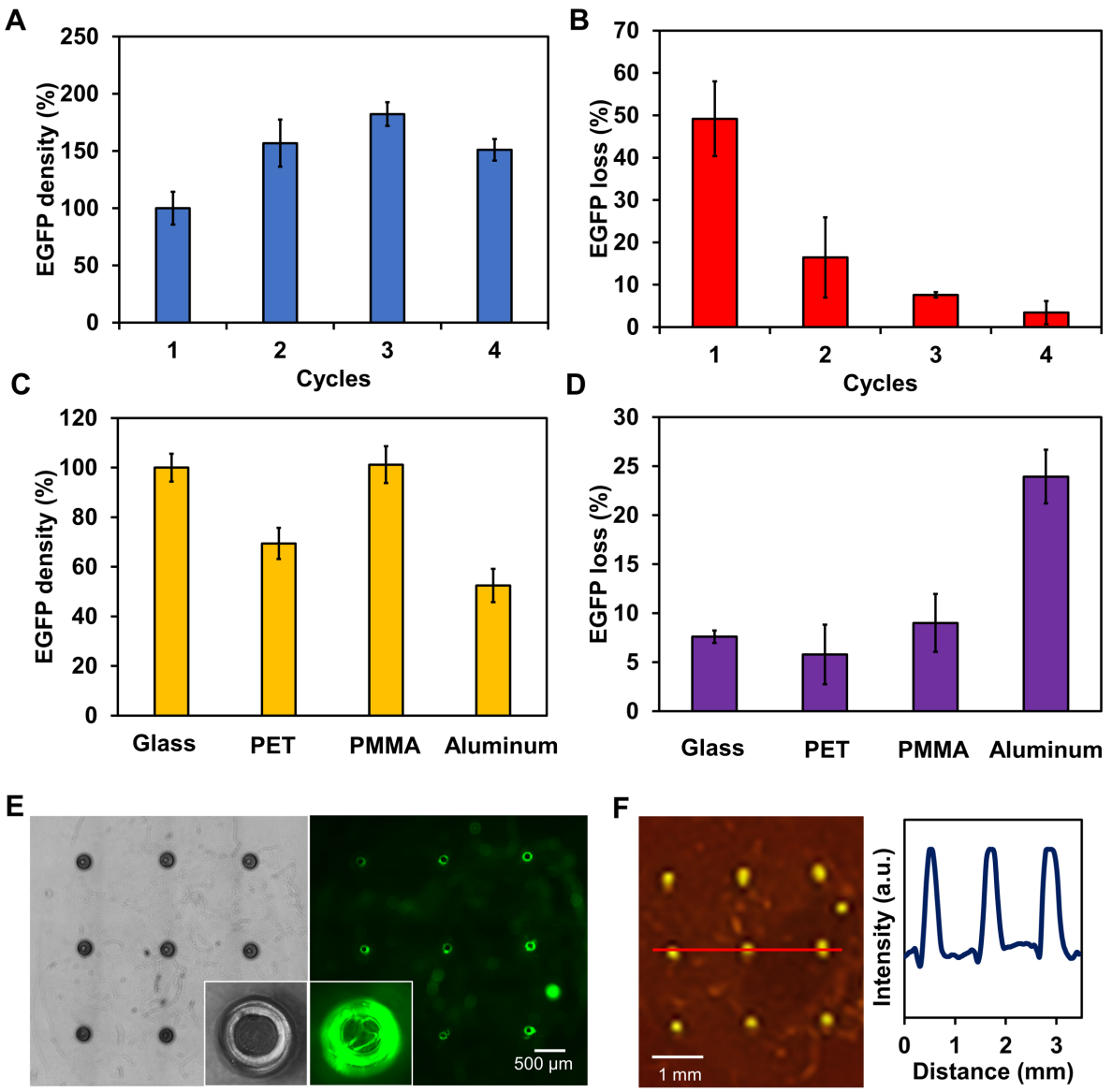

Figure 2.9 Protein density and stability of self-assembled EGFP-Z_E/Z_R-ELP coatings.

(A) Relative protein density of EGFP in the coatings from repeated assembly and deposition cycles. The EGFP densities are normalized to the value from a single cycle. (B) Loss of EGFP from the coatings after three-hour incubation. (C) Relative protein density of EGFP on four distinct substrates: glass, PET, PMMA, and aluminum. The EGFP densities are normalized to the value from glass. (D) Loss of EGFP from the protein coatings after a three-hour incubation. (E) Micrographs of a protein-coated micropillar array (left: bright field, right: green fluorescence) and the close-up images (insets). (F) An optical image of the protein-coated micropillar array under a transilluminator (left) and the fluorescent intensity profile of a cross-section (indicated by the red line in the left image, right).

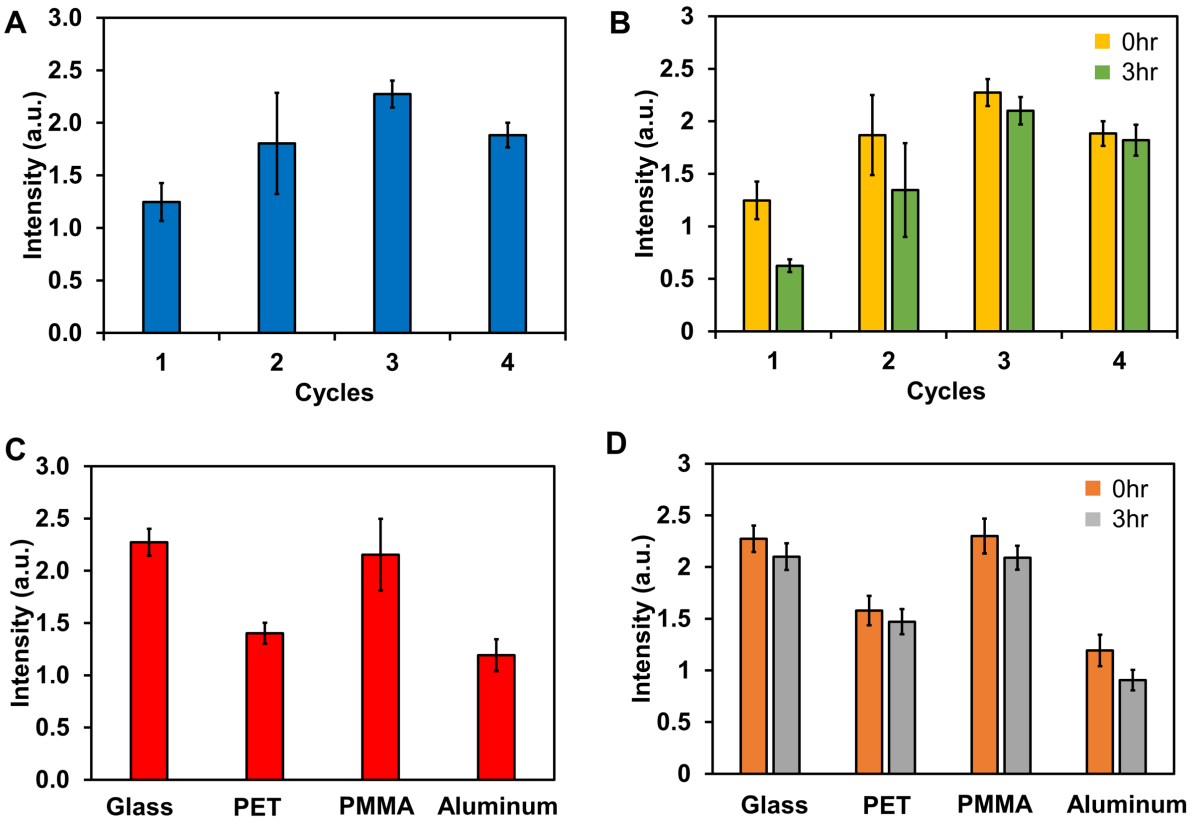

Figure 2.10 Relative fluorescence intensities from EGFP-Z_E/Z_R-ELP coatings before normalization.

(A) Coatings from repeated assembly and deposition cycles. (B) Fluorescence changes from the coatings in panel B after a three-hour incubation buffer. (C) Coatings on various substrates: glass, PET, PMMA, and aluminum. (D) Fluorescence changes from of the coatings in panel C after three-hour incubation buffer.

The fluorescence intensity difference between the 3-cycle and 4-cycle protein coatings was not statistically significant (Figure 2.11). This could be due to surface saturation, as the maximum loadable proteins may have been reached after three coating cycles, limiting further EGFP incorporation. Cross-sectional analysis of samples from a single coating cycle revealed uneven fluorescence distribution (Figure 2.12), which could decrease response intensity and reduce sensitivity in fluorescent biosensor applications. In contrast, the 3-cycle process improved fluorescence homogeneity, a critical factor for enhancing biosensor functionality. In addition, we

observed an increase in the stability of the protein coatings. The repeated deposition of proteins resulted in a reduction in protein loss after long-term incubation of a coating of Z_R-ELP/EGFP-Z_E in buffer (~ 3 hours) (Figure 2.9.B). The coating from a single deposition showed a nearly 50% decrease in the fluorescence from the coating, while it was significantly reduced to below 10% after three or four cycles of repeated protein depositions.

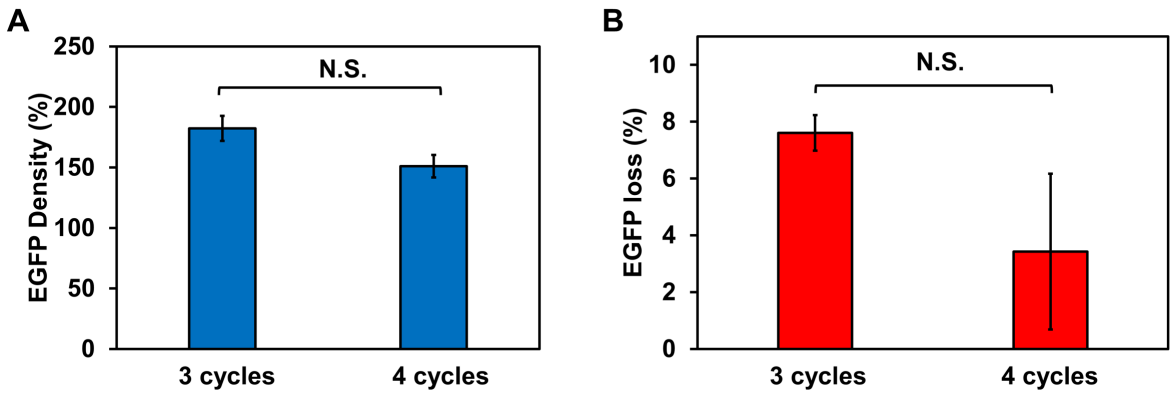

Figure 2.11 Comparison of EGFP-Z_E/Z_R-ELP coatings from 3 and 4 cycles.

(A)Relative protein density of EGFP in the coatings. (B) Loss of EGFP from the coatings after three-hour incubation. Not significant (N.S.); $p \geq 0.05$ ($n = 3$).

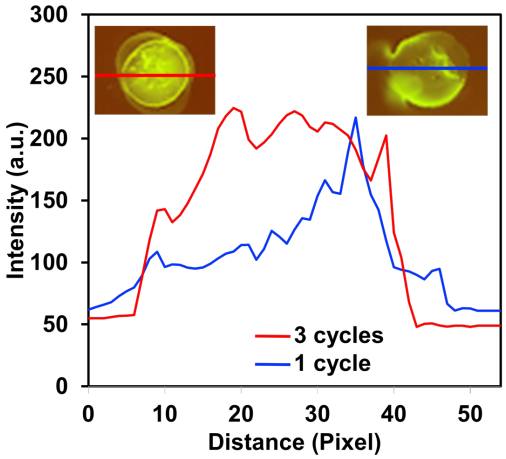

Figure 2.12 Cross-sectional fluorescent intensity profiles from one cycle (blue) and three cycles of protein deposition on glass substrates (red).

The insets show fluorescence images highlighting the corresponding cross-sections.

We also conducted a negative control experiment to investigate non-specific physical protein adsorption. Following the protocol for a single cycle without Z_R-ELP, a protein coating was created and the fluorescence from EGFP was quantified. The results showed that fluorescence intensity was reduced by about seven times (Figure 2.13), indicating that the EGFP coating is primarily driven by the specific dimerization of Z_E and Z_R, with minimal physical adsorption.

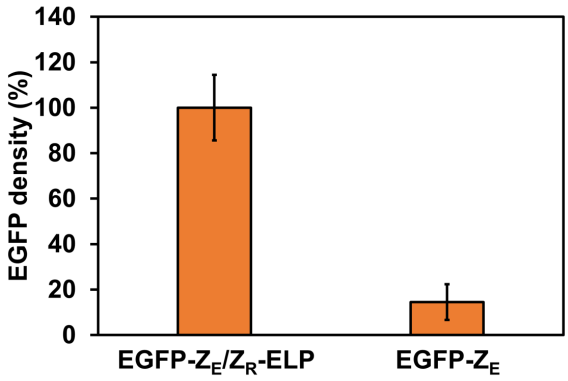

Figure 2.13 The effect of the Z_R-ELP on the protein coating assembly.
Relative protein density of EGFP in the coating prepared in the presence (left) and absence of Z_R-ELP (right). The EGFP densities are normalized to the value from a single cycle assembly of EGFP-Z_E/Z_R-ELP coating.

The fluorescence intensity quantified using a smartphone camera was linearly dependent on the concentration of EGFP-Z_E (Figure 2.14). We correlated the relative fluorescence unit (RFU) and the EGFP-Z_E concentrations using a microplate reader, which was further correlated with the fluorescence intensity quantified from the smartphone images. The result shows a linear relationship between the fluorescence intensity of the coating, the corresponding RFU, and the protein concentration. It verifies the improvement in the density of EGFP incorporated within the coating and the stability of coating attachment. Further in-depth analysis using techniques such as

QCM-D could provide precise measurements of the total mass of adsorbed proteins on the surface, which could be correlated with the amount of EGFP incorporated and its overall stability.

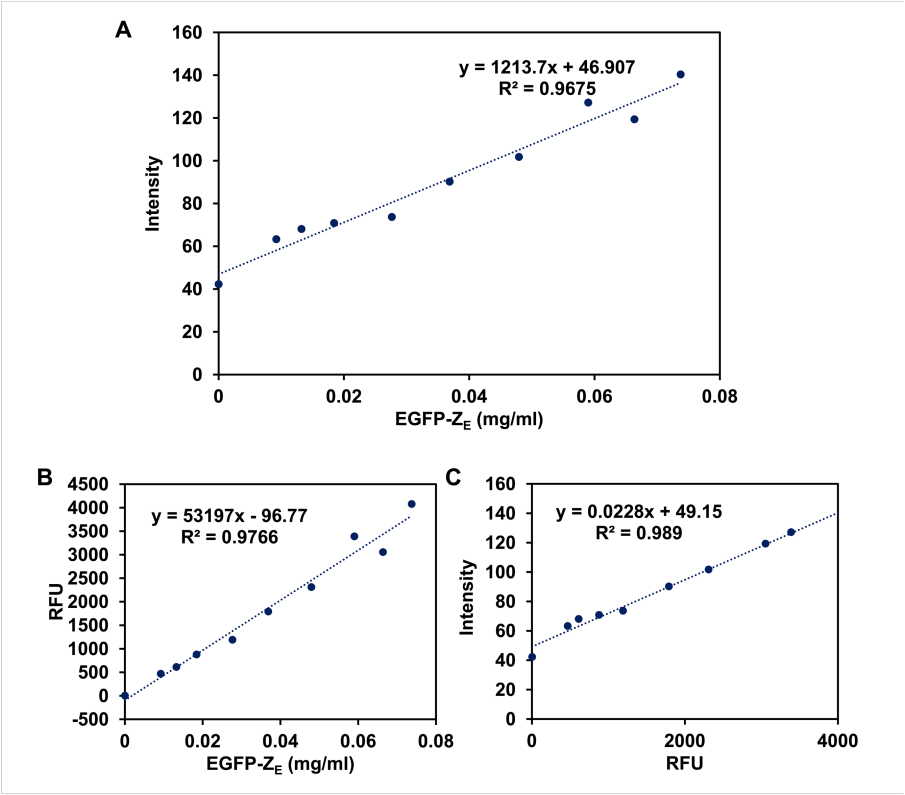

Figure 2.14 Quantification of protein coating using a calibration curve

(A) Calibration curve for the fluorescence intensity from smartphone images as a function of the concentration of EGFP-Z_E. (B) The relative fluorescence units (RFU) that correspond to the concentration of EGFP-Z_E. (C) The fluorescence intensity from smartphone camera images that correspond to RFU obtained from a microplate reader. The calibration curve in panel (A) was generated from the curves in panels (B) and (C).

2.3.3 Deposition of Protein Coatings on Four Distinct Substrates

Next, we conducted protein coating assembly on four distinct substrate materials to demonstrate the versatility of our method. The coating of Z_R-ELP/EGFP-Z_E from three repeated cycles of protein deposition on three different substrates other than glass, including polyethylene terephthalate (PET), polymethyl methacrylate (PMMA), and aluminum, showed higher levels of fluorescence intensity, as shown in Figure 4C. The protein coatings on the polymeric substrates (PET and PMMA) had an EGFP density of ~70% and ~100% relative to glass, respectively. Both were as stable as the coating on glass, according to the result from the 3-hour stability test (Figure 2.9.D). This finding suggests that similar levels of protein density and stability were achieved using these polymeric substrates, although the coating on aluminum was not as stable as the one on glass. The aromatic and non-aromatic polymers with hydrophobic properties, PET and PMMA, facilitate hydrophobic interactions with Z_R-ELP, while negatively charged glass surfaces enhance the adsorption of Z_R-ELP, which has a positive charge (PI = 11.59 at pH 7.4), through strong electrostatic interactions. In contrast, aluminum may exhibit increased hydrophilicity due to the formation of a thin oxide layer, which could reduce the stability of protein coatings. Overall, the results demonstrate the versatility of our protein coating platform across four distinct glass or polymer substrate materials without covalent conjugation or any pretreatment of substrates.

In biomedical applications, devices with microarchitectures are often combined with biological components like proteins. For example, microneedles are micron-scale medical devices used for transdermal delivery of drugs, vaccines, and other therapeutics.[188–190] To test the feasibility of our coating method on microfabricated surfaces, we conducted protein coating assembly (Z_R-ELP/EGFP-Z_E) on a micropillar array that is widely used for microneedles. After repeated protein coating deposition on the array of micropillars from photolithographic patterning,

we imaged them using a fluorescence microscope. The green fluorescence from the micropillars in the micrograph (Figure 2.9.E) indicates the formation of the protein coating on the surface of the micropillars. We were also able to confirm that the green fluorescence could be imaged and quantified using an LED transilluminator and smartphone camera, followed by imaging analysis (Figure 2.9.F). This indicates that, without functionalization, the formation of dense protein coating was achieved directly from the micropillar array. As demonstrated in Figure 2.9, our method can be extended to microneedles fabricated using a variety of substrates such as glass and polymers, as surface treatment or functionalization is not necessary. We anticipate our approach will be a good alternative to conventional spray coating methods.[191,192]

2.3.4 Calcium Sensing for the Detection of Hypercalcemia

Lastly, we demonstrated the application of our protein coating platform for a calcium biosensor using a genetically encoded calcium ion sensor protein GCaMP. The fluorescent biosensor protein is a highly effective Ca^{2+} probe, having a high signal-to-noise ratio with enhanced Ca^{2+} binding affinity (K_D for $Ca^{2+} \approx 235$ nM).[109] GCaMP6m, an improved version of GCaMP, was developed by modifying the GCaMP sequence through mutagenesis to enhance its sensitivity and speed.[193] The GCaMP6m protein consists of circularly- permuted GFP (cpGFP) and calmodulin (CaM), and the chicken myosin light chain kinase (M13) domains.[110] Upon binding of Ca^{2+} with CaM and M13, a conformational change occurs, which alters the binding orientation of CaM and M13. This causes a change in the chemical environment surrounding the chromophore in cpGFP, which consequently increases the fluorescence intensity. Because of the critical role of intracellular Ca^{2+} in neuronal signaling, GCaMPs have been used to monitor *in vivo* neuronal activities in the mouse cortex, zebrafish, and insects, after gene transfer and transgenic

expression in cells.[193] Extracellular Ca^{2+} also functions as an important messenger[194] and its increased level is associated with diseases like hypercalcemia.[172,195] By assembling a coating of purified GCaMP, we used it to measure the level of Ca^{2+} in biological fluids outside cells.

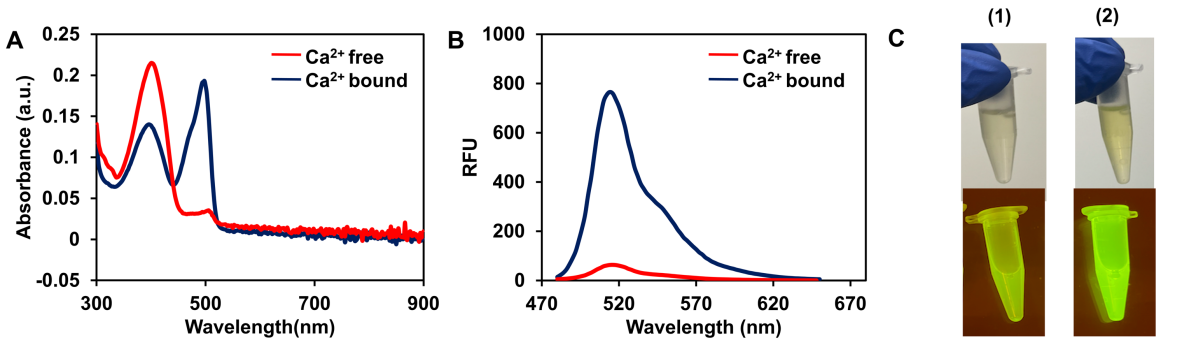

Figure 2.15 Absorbance and fluorescence changes of soluble GCaMP6m-Z_E upon calcium ion binding.

(A) UV-vis absorption spectra. (B) Fluorescence spectra (excitation at 470 nm). The spectra were measured in the presence of Ethylenediaminetetraacetic acid (Ca^{2+}-free, red) or $CaCl_2$ (Ca^{2+}-bound, navy blue). (C) Photographs of soluble GCaMP6m-Z_E at the Ca^{2+}-free (1) and Ca^{2+}-bound state (2) under visible light (top) and transilluminator (bottom).

We designed the recombinant fusion protein GCaMP6m-Z_E for the coating assembly along with Z_R-ELP (Figure 2.2B). After expression and purification from *Escherichia coli*, we confirmed the changes in absorbance and fluorescence intensities upon Ca^{2+} binding (Figure 2.15). The absorbance intensity of GCaMP6m-Z_E shows a significant reduction at 496 nm after the addition of a chelating agent, ethylenediaminetetraacetic acid (EDTA) at 100 μM (Figure 2.15.A). It was immediately recovered after the addition of 100 μM of calcium chloride. Moreover, the fluorescence intensity of GCaMP6m-Z_E changed in response to the binding of Ca^{2+}, as confirmed by the data in the presence of EDTA or $CaCl_2$ (Figures 2.15.B and 2.15.C). The results indicate that the sensing ability of GCaMP6m was not affected by the genetic fusion of the Z_E coiled-coil

domain. Following the coating assembly procedure described above for Z_R-ELP and EGFP-Z_E, we created a protein coating that included GCaMP6m-Z_E on glass substrates (Figures 2.16.A and 2.16.B). After three cycles of coating assembly and deposition, the samples were washed and dried. The coating of Z_R-ELP/GCaMP6m-Z_E on glass had a green-emitting fluorescent microstructure, as shown in the micrograph (Figure 2.16.A). To prepare a protein coating at a Ca^{2+}-free state, EDTA (100 μM) was added to a solution of GCaMP6m-Z_E and removed from the coating during the washing step. The protein coating was incubated with aqueous solutions at a range of Ca^{2+} concentrations, and the fluorescence from the coating was imaged using a smartphone camera, followed by image analysis to quantify the intensities.

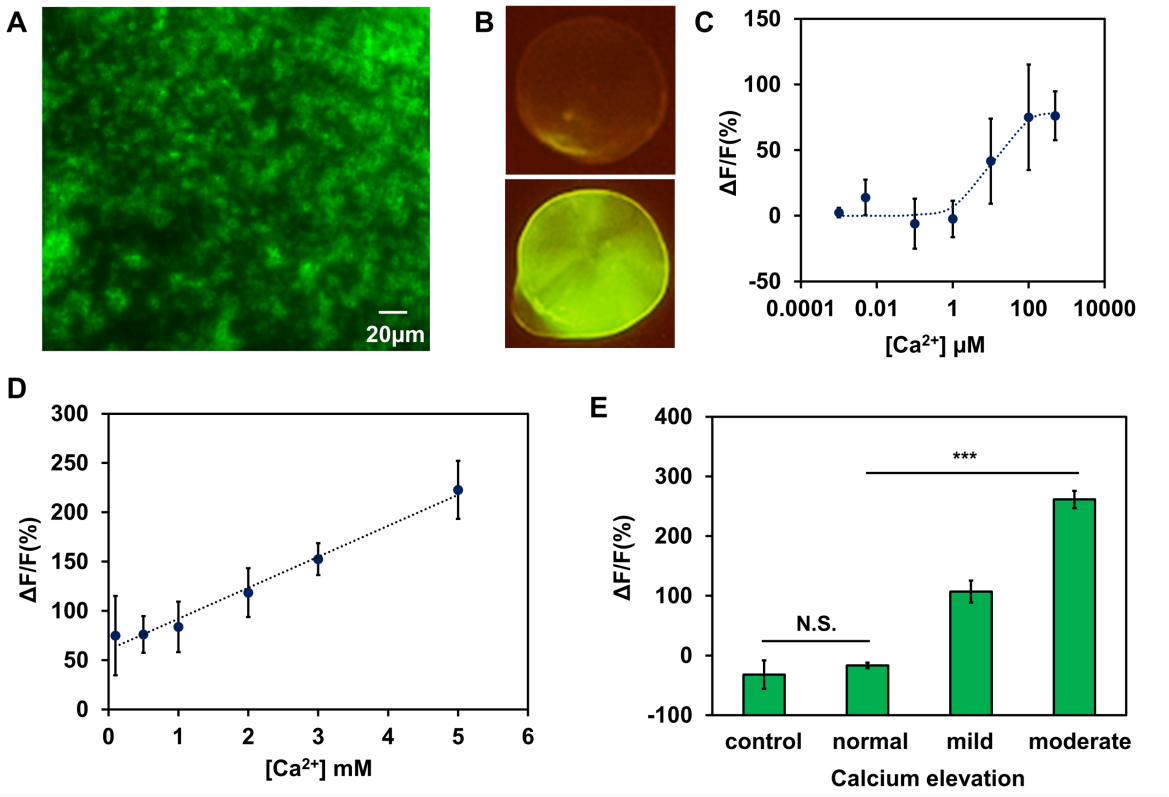

Figure 2.16 The self-assembled GCaMP6m-Z_E/Z_R-ELP coating.

(A) A fluorescent micrograph. (B) Optical images of the coatings under a transilluminator before (top) and after incubation with 5 mM Ca^{2+} (bottom). (C) The Ca^{2+}-dependent relative fluorescence intensity ($\Delta F/F_0$) in the range of 1 nM to 500 μM. Experimental data were fitted to a binding model (dotted line) to evaluate $K_{D,app.}$ (D) The $\Delta F/F_0$ curve in the range of 0.5 to 5.0 mM. Experimental data were fitted to a linear model (dotted line). (E) The $\Delta F/F_0$ response from Tyrode's solution under hypercalcemia-related physiological conditions: control (no calcium), normal (1.3 mM), and mild (1.5 mM) or moderate hypercalcemia (1.8 mM). ***$p \leq 0.005$, and not significant (N.S.). The error bars in panels C, D, and E represent the standard deviation (n = 3).

The fluorescence from the Ca^{2+}-free coating was quickly recovered after exposure to Ca^{2+} in water (Figure 2.16.C), and the relative fluorescence intensity ($\Delta F/F_0$) increased up to 76% when the concentrations of Ca^{2+} ranged from 1 nM to 500 μM. The apparent dissociation constant ($K_{D,app}$) was ~11 μM, which is shifted by two orders of magnitude from the values for soluble GCaMP6m.[110] The values of $K_{D,app}$ in general can be shifted due to the higher target concentration in the micro-environment.[196] In our study, the ELP-based protein coating mimics tissue proteins'

micro-environment where Ca^{2+} was far above the K_D of soluble GCaMP6m. Therefore, this shift is most likely due to a higher Ca^{2+} concentration in the micro-environment surrounding the GCaMP probe placed within a protein-rich phase.

The $\Delta F/F_0$ was also plotted against the concentrations of Ca^{2+} in the millimolar level that falls within the calcium levels in the extracellular matrix, from 0.5 to 3.0 mM (Figure 2.16.D).[102,172,197] At this Ca^{2+} concentration level, we observed a drastic change in the fluorescence that was linearly dependent on the concentration of Ca^{2+}. The measured $\Delta F/F_0$ was from 76% to 223% at the Ca^{2+} concentrations of 0.5 to 5.0 mM, respectively, and an equilibrium binding model did not provide a good fit to the data. This may be due to the complex binding mechanism between GCaMP and Ca^{2+} in this concentration range and more complex binding models such as cooperativity in the ELP domain and Ca^{2+} may need to be considered after additional biophysical characterizations.[198]

The coating of Z_R-ELP/GCaMP6m-Z_E was then used to detect hypercalcemia, which is characterized by elevated Ca^{2+} concentrations in the extracellular fluid. The normal Ca^{2+} concentration is around 1.3 mM, while mild hypercalcemia manifests with Ca^{2+} concentrations around 1.6 mM and moderate hypercalcemia exceeds 1.8 mM.[199] In order to evaluate the sensing ability of our coating platform in the extracellular fluid, we conducted experiments varying Ca^{2+} concentrations in Tyrode's solution that mimics the interstitial fluid. It is a solution with the composition of ions close to the tissue fluid and contains glucose and bovine serum albumin (BSA). The coating incubated with a solution of 1.3 mM Ca^{2+} exhibited $\Delta F/F_0$ of -17 ± 5 % (Figure 2.16.E). Conversely, the coating under the mild hypercalcemia condition of 1.5 mM Ca^{2+} showed $\Delta F/F_0$ of 107 ± 18 %, while the $\Delta F/F_0$ of the sample of moderate hypercalcemia condition (1.8 mM) was 261 ± 14 %. The $\Delta F/F_0$ values corresponding to mild and moderate hypercalcemia were

significantly higher than the normal condition, and the signal difference between mild and moderate hypercalcemia was also significant ($p \leq 0.005$). The reduction of fluorescence under normal or no-calcium conditions could be attributed to the interaction of Ca^{2+} with BSA.[200] In an additional experiment, the relative fluorescence change from tris-buffered saline (TBS) containing Ca^{2+} but no BSA was compared to the same buffer that includes Ca^{2+} and 1% BSA (Figure 2.17). Although a minor decrease in fluorescence was observed with the addition of BSA, statistical analysis indicates that the difference in the fluorescence intensities is not significant.

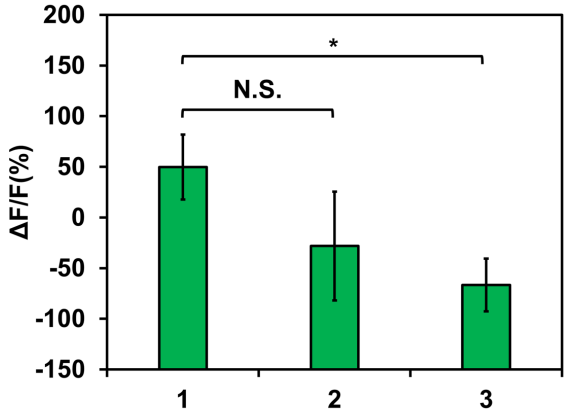

Figure 2.17 The $\Delta F/F_0$ response under hypercalcemia-related physiological conditions.
(1) 1.3 mM of $CaCl_2$ in tris buffered saline (TBS) without bovine serum albumin (BSA), (2) 1.3 mM of $CaCl_2$ in TBS with 1% BSA, (3) 1.3 mM of $CaCl_2$ in deionized water with 1% BSA. *$p \leq 0.05$ and not significant (N.S.)

We conducted additional experiments using a mammalian cell culture medium and fetal bovine serum (FBS), which mimics the protein-rich conditions in tissue fluid or blood. Dulbecco's Modified Eagle's Medium (DMEM) was supplemented with FBS to simulate normal calcemia and hypercalcemia conditions, and the fluorescence intensity changes from protein coatings incubated in the media were quantified. The results showed a 19.5% (±15.9) increase in fluorescent intensity in the normal calcemia region, while increases of 102.3% (±43.5) and 268.5% (±58.5) were observed in mild and moderate hypercalcemia, respectively (Figure 2.18). Both hypercalcemia

conditions showed fluorescence changes statistically different from the normal calcemia condition. Despite a minor loss in the sensitivity, these results validate that our calcium sensor coating could potentially work for blood or tissue fluid samples from patients.

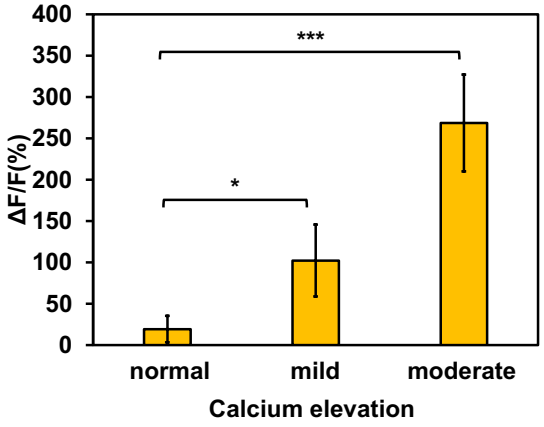

Figure 2.18 ΔF/F0 response from FBS with DMEM solution under hypercalcemia-related physiological conditions.

Normal (1.3 mM), mild (1.5 mM) and moderate hypercalcemia (1.8 mM). ***$p \leq 0.005$, *$p \leq 0.05$. The error bars indicate the standard deviation.

Hypercalcemia is frequently associated with several types of cancers.[195,199] The regulation of calcium homeostasis is interrupted, leading to the increase of the calcium level in the bloodstream above the normal level. During the asymptotic stage, the onset of mild hypercalcemia is associated with cancer development.[199] The fluorescence calcium sensor device demonstrated in this paper showed a sensing ability sufficient to detect mild or moderate hypercalcemia. The current Ca^{2+} sensors for the high concentration range (0.5–3.0 mM) are based on photonic polymers,[166,167] aggregation-induced emission luminogen,[201] functionalized gold nanoparticles,[168,169] and a chemical fluorescence indicator,[172] which require a spectrophotometer or microscope for signal measurement. Genetically modified Ca^{2+} sensors with weaker affinities than GCaMPs operate within this concentration range[113,202] but have only been used to monitor

Ca^{2+} dynamics with a fluorescence microscope. In contrast, our detection method operates in a low-resource setting by using a smartphone camera equipped with an LED and light filter, which suggests a potential use for a point-of-care (POC) platform in a clinical setting. The high surface area-to-volume ratio feature generated by the microstructured coating was critical for the high-density inclusion of fluorescent biosensor proteins like GCaMP, providing enhanced resolution for calcium quantification with these low-resource settings. This feature may also have broader bioengineering applications, particularly where reaction efficiency and mass transfer are critical. Also, our coating fabrication process based on protein solution casting can be extended to the manufacturing of low-cost disposable sensor platforms as demonstrated in portable electrochemical sensors.[203,204] We anticipate such a platform will facilitate a more accessible and early diagnosis of cancer in combination with the detection of other cancer-related metabolites.

2.4 Conclusion

We demonstrated a self-assembly method of protein coatings with microstructural features and programmable functionality by leveraging the modular design of recombinant proteins. The temperature-triggered coacervation through an inverse phase transition followed by non-covalent protein binding of coiled coils resulted in microstructured functional protein coatings. This method is applicable to additional types of substrate materials and modular to program a functionality by incorporating globular functional protein domains like EGFP or GCaMP. We created a calcium biosensor device that quantified the Ca^{2+} level relevant to the detection of hypercalcemia conditions. This modular and versatile protein coating platform is based on a simple, chemical-free, and water-based process under biocompatible conditions. Using the genetically encoded fluorescent biosensor proteins for a variety of targets,[205] we anticipate this platform will provide

methods to develop a POC application with rapid and continuous monitoring of disease-associated biomarkers in a low-resource setting.

Chapter 3 - Cooperative Assembly of Nanoparticle-Encapsulating Protein Cages

3.1 Background and Motivation

In recent years, protein-based materials have been extensively investigated as hybrid materials in combination with non-protein foreign components due to their ability to form diverse structures and control materials' properties.[3,206–208] These hybrid materials improve the physical and chemical properties of the protein materials, making them more promising. Specifically, protein-based hybrid materials have paved the way for advancements in biotechnology, including biocatalysts[209], biosensors[210], and targeted drug delivery systems.[211,212] Proteins can be engineered into various structures, which serve as templates to enhance aqueous solubility[213], stability[87], and biocompatibility. [213–215] One of the structures found in protein-based materials is the protein, which features a spherical structure with an inner cavity capable of capturing molecules while isolating them from the external environment.[216,217] This feature facilitates the incorporation of foreign materials into its interior, creating a confined space for these molecules.[217–219] Recent studies have demonstrated that nanoparticles can be loaded in the inner cavity, while exterior surfaces present enhanced biocompatibility and ability for targeting.[87,218,220,221] These characteristics have led to a growing focus on the application of protein cages for drug delivery, as their distinctive morphology provides an optimal environment for drug encapsulation as well as efficient delivery into cells.[91,217,222–226]

A protein cage consists of three interfaces: the exterior surface, inter-subunit region, and inner cavity. [219,220,224,227] The properties of protein cages can vary significantly based on the incorporated foreign elements, making them functionally versatile. For instance, surface

modification can equip the external surface with cell-targeting capabilities, optimizing it for a therapeutic application. The inner cavity can host various nanoparticles, such as quantum dot[228], gold[224], and iron oxide nanoparticles.[229] For instance, ferritin has been utilized as a template for synthesizing or encapsulating inorganic nanoparticles for cancer cell imaging.[224,230] Similarly, virus-like particles have been chemically modified to load and deliver therapeutic cargo materials.[90,223] These protein nano-cages often exhibit limited nanoparticle loading capacity. High concentrations of nanoparticles have only been successfully encapsulated in amphiphilic block-copolymer micelles.[231–233] This raises an intriguing question: can protein cages achieve highly packed nanoparticle encapsulation? Protein assembly using a dynamic structural motif might offer a solution to enhance nanoparticle encapsulation.

In this study, we demonstrate the cooperative assembly of protein cages that simultaneously encapsulate nanoparticles with high-density packing. We employed engineered amphiphilic protein building blocks based on an elastin-like polypeptide (ELP), a class of biomimetic polypeptides derived from tropoelastin,[227] ELPs exhibit unique properties, such as lower critical solution temperature (LCST) phase behavior, which mediates liquid-liquid phase separation of proteins into coacervates under a temperature control.[27,31,234] When combined with globular or rod-shaped hydrophilic proteins, ELPs can function as the hydrophobic segment in constructing amphiphilic protein building blocks.[178] These protein building blocks form vesicle-like cages consisting of a monolayer protein membrane with hydrophobic inner surfaces. This structural feature facilitates preferential encapsulation of nanoparticles within the cage, resulting in pomegranate-like structures with a high-density packing of nanoparticles (Figure 3.1). Despite the remarkable ability to encapsulate hydrophobic cargo,[29] the simultaneous nature of nanoparticle encapsulation during protein cage assembly remains unclear. To address this, we investigated the

cooperativity between the cage assembly and nanoparticle encapsulation to understand the underlying mechanism. Additionally, we employed this system to control the optical properties of fluorescent protein cages toward biosensor applications.

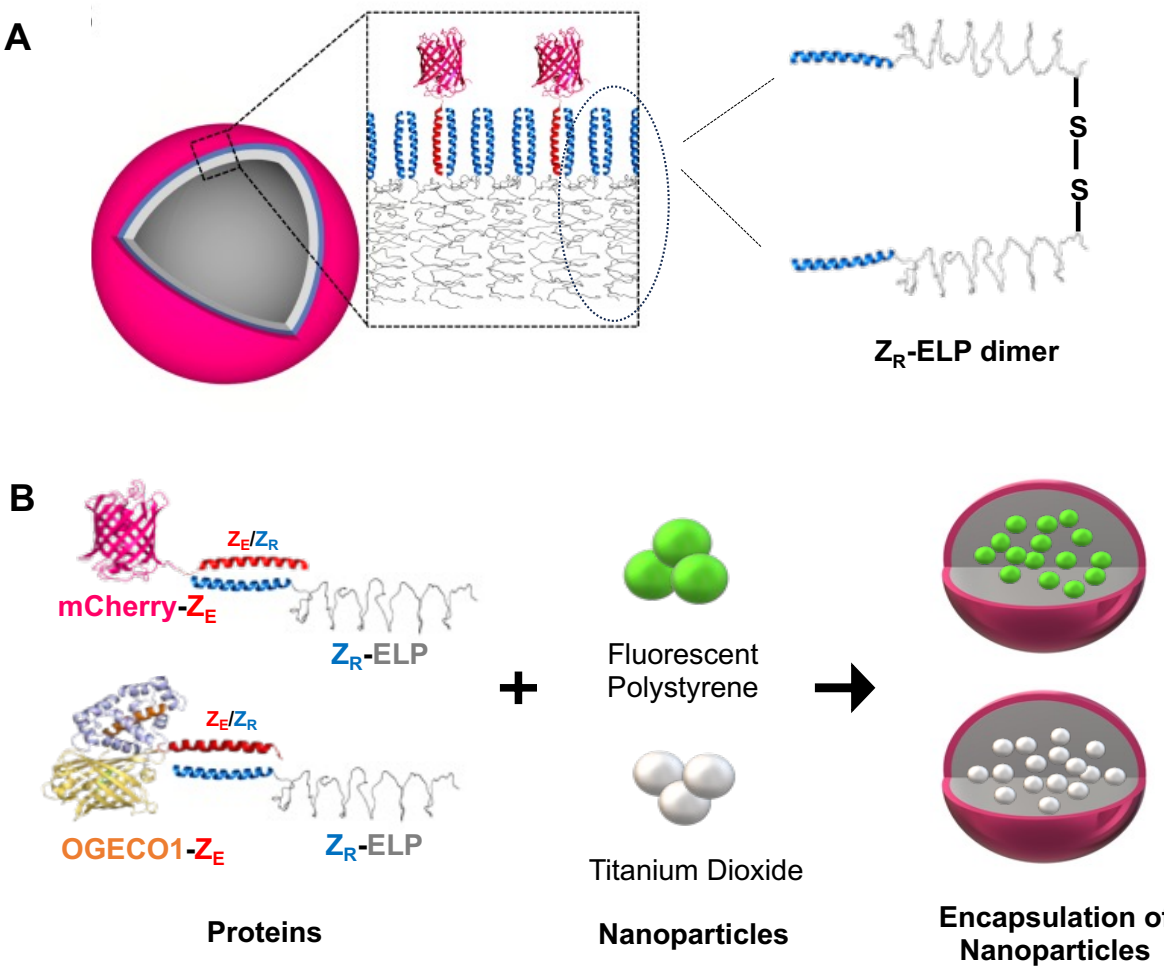

Figure 3.1 Cooperative self-assembly of hybrid protein cages encapsulating nanoparticles simultaneously.

(A) Protein cage structure without nanoparticles. The amphiphilic complexes of recombinant fusion proteins (mCherry-Z_E/Z_R-ELP and Z_R-ELP dimer). (B) Protein complexes (mCherry-Z_E/Z_R-ELP or OGECO1-Z_E/Z_R-ELP) have cooperative interactions with nanoparticles, forming a protein-nanoparticle hybrid coacervate that evolves into a self-assembled cage with high-density packing of nanoparticles.

3.2 Materials and Methods

3.2.1 Materials

The *E. coli* strain T7 Express BL 21 was purchased from New England Biolabs. The plasmids, pQE60- Z_E/Z_R-ELP and pQE60-mCherry−Z_E, were also kindly provided by Professor Julie Champion at the Georgia Institute of Technology. Nickel nitrilotriacetic acid (HisPur™ Ni-NTA) resin was purchased from Thermo Scientific. Fluorescent polystyrene nanoparticles (Fluoresbrite® YG Carboxylate Microspheres 0.50μm) were purchased from Polysciences. Titanium dioxide nanoparticles, the mixture of rutile and anatase (d<100nm), were purchased from Sigma Aldrich. Rhodamine B (RhB) was purchased from ACROS Organics.

3.2.2 Cloning, Protein Expression, and Purification

The DNA sequences encoding OGEO1[235] and the Z_E domain[176] were combined to generate a construct encoding OGECO1-Z_E. The gene fragment was synthesized and inserted into the *NcoI* and *BglII* restriction sites of the pQE60 vector (3.4kbp), followed by sequence verification by GenScript. The resulting plasmid pQE60_OGECO1-Z_E was inserted into T7 Express chemically competent cells. The fusion proteins Z_R-ELP, mCherry-−Z_E, and OGECO1-Z_E were expressed and purified following previously described protocols.[29] Briefly, both proteins contain the His_6 tag for metal affinity purification. Z_R-ELP was co-expressed with His6-Z_E and incubated with Ni-NTA after cell harvesting. 6 M guanidine hydrochloride was used to elute the washed protein, then dialyzed DI water several times and stored at 4°C. For mCherry-Z_E, buffers, including 8 M urea, 10 mM Tris-Cl, and 100 mM Na_2HPO_4 at pH 8.0, were used to lysis the harvested cells. Wash was done with buffer at pH 6.3, and washed proteins were eluted from the resin at pH 4.5. Then, proteins were dialyzed into phosphate-buffered saline (PBS, pH 7.4) and stored at 4°C.

3.2.3 Turbidity Measurement

To make the protein-polystyrene (PS) nanoparticle hybrid, fusion proteins were prepared by combining 30 μM of Z_R-ELP and 1.5 μM of mCherry-Z_E. The proteins were premixed in PBS and maintained at 0^0C in an icebox during the preparation process. Next, we added different volumes of the fluorescent PS solution (1 μl, 2 μl, 3 μl, and 5 μl) to the premixed protein solution. After thorough mixing, the protein-nanoparticle hybrid solutions were transferred to a cuvette. The absorbance was measured at 400 nm for 30 minutes using a Thermo Fisher BIOMATE 160 spectrophotometer while maintaining the temperature at 25°C with a Peltier controller. The data was collected every minute. For the protein-TiO_2 nanoparticle hybrid, 100 μl of a 2.5% (w/v) TiO_2 suspension was added to the same protein mixture used above. Data collection follows the same procedure, with measurements taken every minute.

3.2.4 Fluorescence Microscopy

Images of TiO_2 nanoparticles with recombinant protein cages taken by inverted fluorescent microscopy (Olympus IX73). A protein complex with nanoparticles was prepared at 0ºC and then gently centrifuged for one minute. A 5μl aliquot of aggregated proteins were placed on a slide glass (24 x 60 mm), then covered with square cover glass. (18 x 18 mm). All images are captured with 40x objectives with Texas Red for red fluorescence and bright field imaging.

3.2.5 Photocatalytic Activity Measurement

The photocatalytic activity was assessed under various radiation conditions and sample compositions. Control samples were prepared without UV radiation, using PBS and 20 μM Rhodamine B. One control sample included 100 μl of TiO_2 nanoparticles. Additionally, samples

were prepared with bare TiO_2 in PBS, a protein solution (30 μM ZR-ELP and 1.5 μM mCherry-ZE), and protein combined with 100 μl of TiO_2 nanoparticles, all mixed with 20 μM Rhodamine B. Each sample was placed in a 1 mL glass vial and incubated at room temperature for 30 minutes. After this incubation period, three of the samples were irradiated with UV light (BTLab SYSTEMS, 302 nm, 50-60 Hz). Images were captured every hour to monitor the photocatalytic activity.

3.2.6 UV-Transmittance Measurement

The UV blocking property was determined by measuring the UV transmittance. Samples containing TiO_2 nanoparticles and those without were prepared in the icebox and transferred to 1 mm quartz cuvettes. UV transmittance spectra were recorded from a BIOMATE 160 (Thermo Fisher) UV−vis spectrometer ranging from 200 nm to 300 nm.

3.2.7 Fluorescence Measurement

The fluorescence of the OGECO1-Z_E/Z_R-ELP was measured by Biotek 96-well microplate reader at 25°C. To achieve a Ca^{2+}-free state, OGECO1-Z_E was treated with 100 μM of EDTA. To validate the effect of TiO_2 nanoparticles, recombinant proteins (at a 0.05 ratio) were prepared with and without 50μl of TiO_2 nanoparticles. To each 90 μl of the protein mixture, 10 μl of the $CaCl_2$ solution with varying concertation was added. Fluorescence was measured at an excitation wavelength of 520nm with 570nm emission.

3.3 Results and Discussion

3.3.1 Encapsulation of Nanoparticles into the Vesicle-like Protein Cages

The vesicle-like protein cages were assembled from amphiphilic recombinant fusion protein complexes.[29] Two recombinant fusion proteins were used: of a globular protein, mCherry, fused with a glutamic acid-rich leucine zipper, Z_E, (mCherry-Z_E), and an arginine-rich leucine zipper, Z_R, fused with an ELP (Z_R-ELP). They can undergo either hetero- (Z_R:Z_E, colon denotes dimerization) or homo-dimerization (Z_R:Z_R), resulting in "globule-coil-rod" (mCherry-Z_E/Z_R-ELP) or "rod-coil" complexes (Z_R-ELP dimer) when mixed (Figure 3.1). The vesicle-like cages, featuring hydrophobic inner surfaces, were formed from these amphiphilic protein complexes, which allowed preferential encapsulation of nanoparticles.[29]

3.3.2 Correlation between Cage Size and Number of Nanoparticles

We prepared the recombinant fusion proteins Z_R-ELP and mCherry-Z_E in phosphate buffered saline (PBS) and mixed them with polystyrene (PS) nanospheres (diameter ~ 500 nm). The self-assembly of protein cages was induced by increasing temperature from 4°C to 25°C. This temperature elevation resulted in a rapid increase in turbidity, confirming the formation of vesicle-like protein cages. Fluorescent microscope images revealed pomegranate-like particles where PS nanospheres (green) were encapsulated by the protein membrane (red) (Figure 3.2.A). The protein membrane contained mCherry with red fluorescence, while the PS nanospheres exhibited green fluorescence. The internal space of the vesicle-like cages was densely packed with PS nanoparticles, which distinguished them from the morphologies observed in nanoparticle-encapsulating cages reported in other studies.[224,228,229] The number of encapsulated PS nanoparticles (n_{PS}) observed in the microscope images ranged from 1 to over 14 (Figure 3.2.B).

However, the high-density encapsulation gave rise to an overall pomegranate-like morphology. We estimated the volume density of PS nanoparticles per volume of a protein cage (as shown in Figure 3.3.A) and observed a significantly narrower distribution in packing density. This finding suggests a controlled density of nanoparticle packing, independent of the total number of nanoparticles encapsulated within each cage. We also observed that the diameters of protein cages were proportional to the number of encapsulated PS nanospheres (Figure 3.2.B). The average diameter of protein cages containing PS nanospheres ($d_C \sim 2.3 \pm 0.6$ μm) was larger than that of the hollow cages without PS nanoparticles (~1.5 μm),[29] indicating the cooperative interaction between the nanoparticles and the protein building blocks during cage formation. The image analysis demonstrated that the estimated number of PS nanoparticles encapsulated within each cage (n_{PS}) scales to the volume of protein cages ($n_{PS} \sim d_{HC}^3$, Figure 3.3.A. and B). Consistently, the number of PS nanoparticles counted from cross-sectional images was approximately proportional to the cross-section area of the cages ($n_{PS} \sim d_{HC}^2$). The dependency of protein cage size on the number of encapsulated nanoparticles supports the existence of interactions that facilitate the incorporation of nanoparticles during the coacervates formation, ultimately leading to a core-shell morphology. In the absence of nanoparticles, the intermediate coacervate phase transitioned into hollow cages, further supporting this mechanism.[180,236]

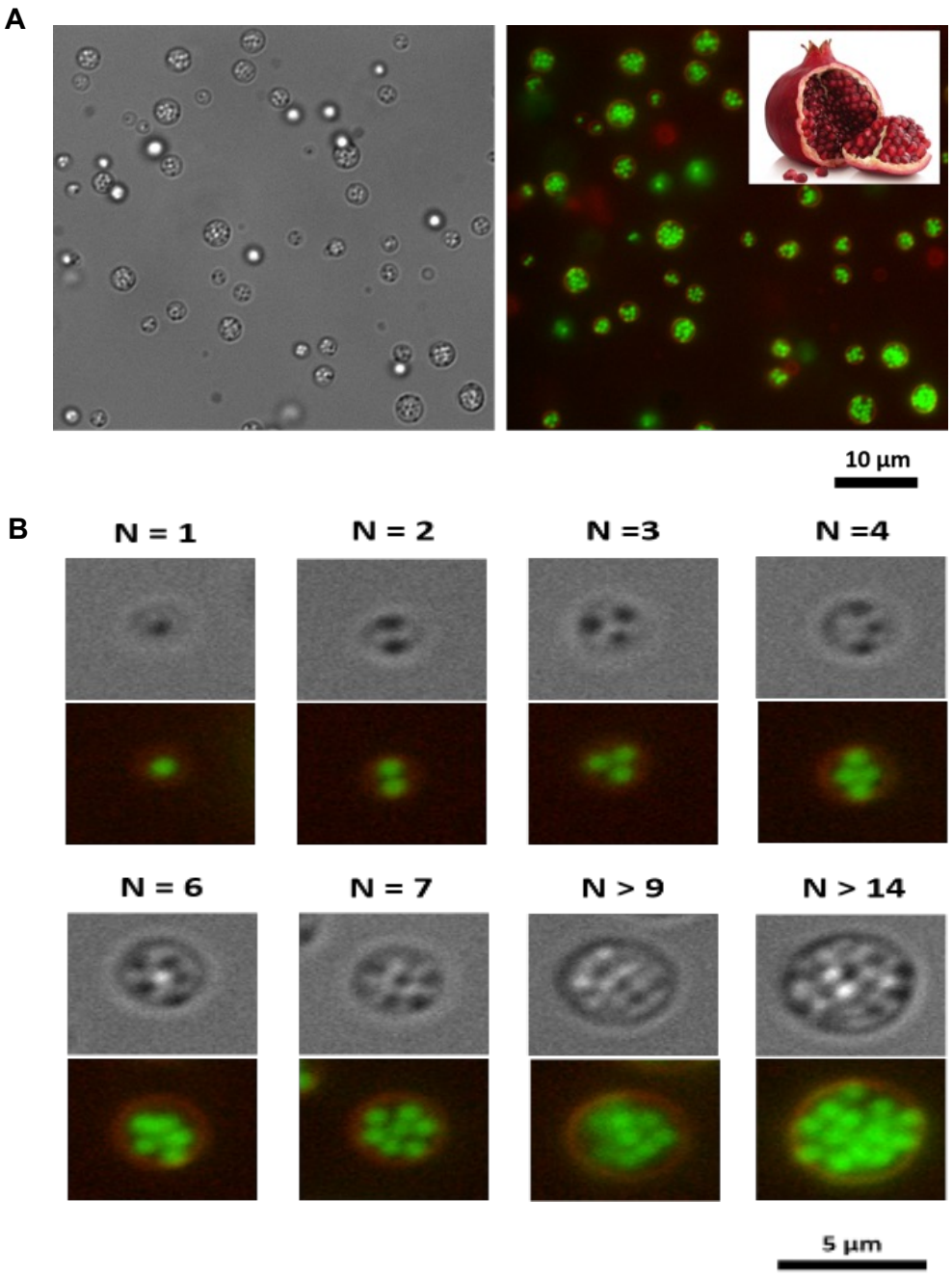

Figure 3.2 The morphology of protein cage encapsulating PS nanoparticles.

(A) Fluorescent microscope images of self-assembled protein cage with PS nanoparticles. The red fluorescence is attributed to mCherry-Z_E, while the green fluorescence is from the PS nanoparticles. (B) Individual protein cages and the number of PS nanoparticles encapsulated within each cage.

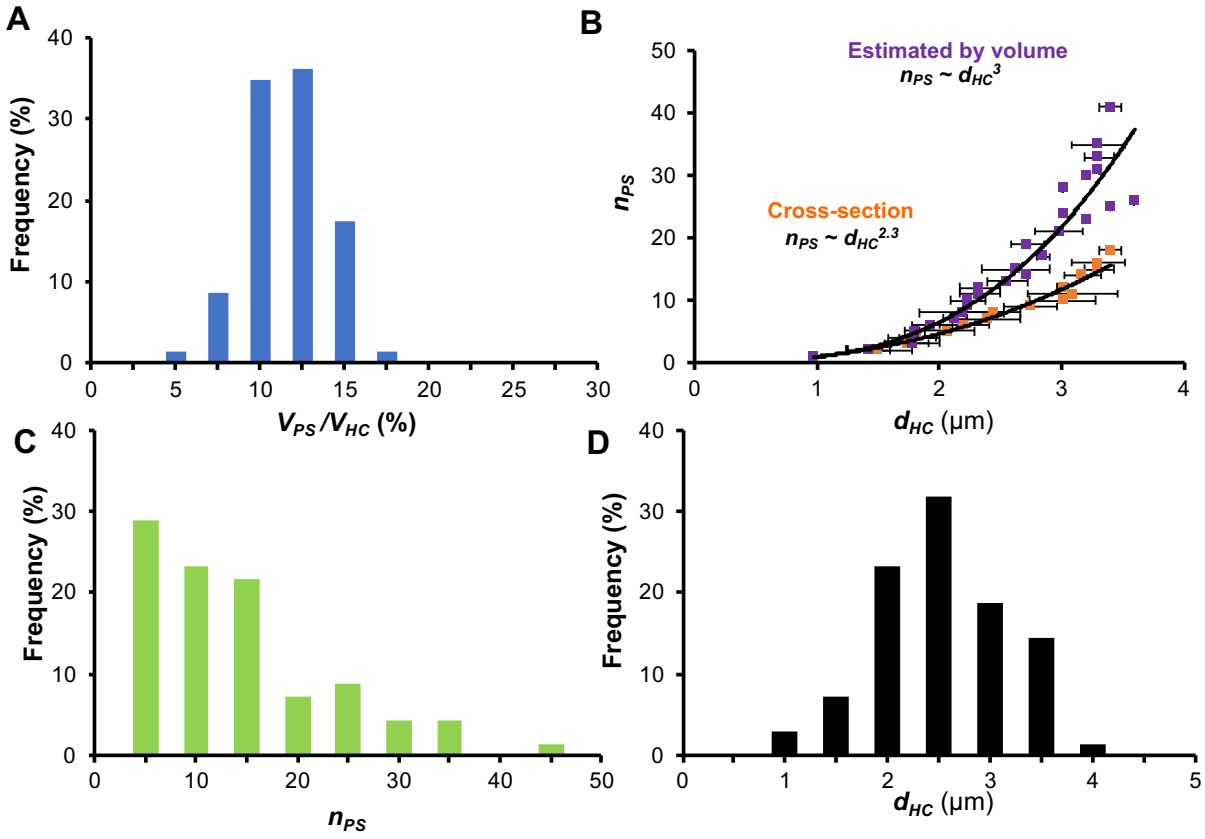

Figure 3.3 Relationship between protein cages and nanoparticles

(A) Distribution of cage sizes as a percentage of total frequency (B) Correlation diameter of cages and nanoparticles from the cross-sectional area and estimated volume. (C) Histogram of protein cages with different numbers of encapsulated nanoparticles. (D) Size distribution histograms of protein cages with different diameters of hollow spheres.

Additionally, we confirmed the distribution of encapsulated nanoparticles within the protein cages (Figure 3.3.C). This suggests a potential interaction between the protein and the nanoparticles, as most cages contain small encapsulated particles while maintaining a consistent nanoparticle volume fraction per cage. Furthermore, as shown in Figure 3.3.D, the size distribution of the protein cages exhibits a Poisson distribution, indicating that the encapsulation process is stochastic.

3.3.3 Kinetics of Nanoparticle Encapsulation

The turbidity profiles further support the cooperative interactions between the protein building blocks and PS nanoparticles during cage self-assembly. In the presence of PS nanoparticles (ranging from 3.64 to 18.2 particles/μL), turbidity changes during the initial inverse phase transition were measured as a function of time. Turbidity is associated with the presence of coacervates.[178] In the initial stage for coacervate formation, turbidity increases rapidly, followed by a gradual decrease during the maturation stage of self-assembly. A higher concentration of nanoparticles led to a slower rise in turbidity profile between 4 and 7 minutes (Figure. 3.4.A). To be consistent, a steeper decline in the slope of turbidity change was observed during that period at higher nanoparticle concentrations (Figure. 3.4.B). The results indicate the presence of interactions between the protein building blocks and PS nanoparticles during the initial stage for coacervate formation. According to the self-assembly mechanism of vesicles formed by Z_R-ELP and mCherry-Z_E,[180] a the process involves a transition from coacervate to vesicle. Similarly, the nanoparticle-bound protein coacervates are likely to undergo a transition to vesicles, during which the PS nanoparticles are positioned in the core and the amphiphilic protein complexes organize into a membrane structure that enclose the nanoparticles.

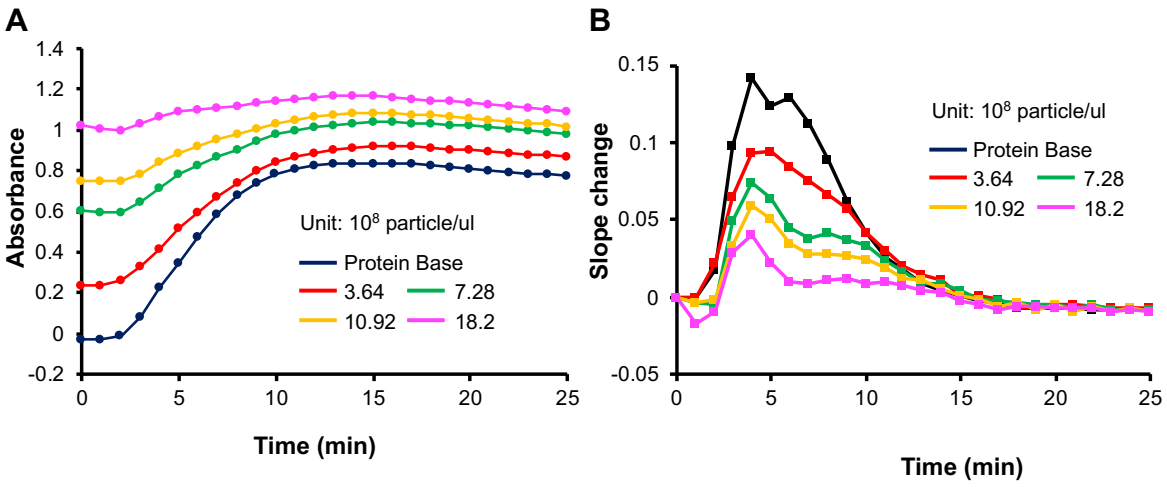

Figure 3.4 Absorbance changes during protein cage formation

(A) Turbidity profile observed during the inverse phase transition, with measurements taken at a fixed wavelength of 400 nm. Protein solutions were initially cooled in an icebox and then heated to 25℃ after the addition of PS nanoparticles. (blue: protein only, red: 3.64 particles/μl, green: 7.28 particles/μl, yellow: 10.92 particles/μl, magenta: 18.2 particles/μl) (B) Time-dependent changes in turbidity, the slope change of the turbidity profiles plotted in panel (A).

3.3.4 Encapsulation of Titanium Dioxide (TiO_2)

To evaluate whether different types of nanoparticles can be encapsulated, we used this platform for the encapsulation of titanium dioxide (TiO_2) nanoparticles. TiO_2 nanoparticles is well known as sunscreen agent[237] and photocatalyst[238] due to their effective UV absorption and radical generation under UV radiation. However, TiO_2 can release reactive oxygen species (ROS), which may promote skin photodamage through photocatalytic degradation.[239] Surface inhibition of TiO_2 particles, if encapsulation is successful, could reduce photocatalytic activity. To test this, we investigated the photocatalytic activity of TiO_2 encapsulated by the protein cage under UV radiation.

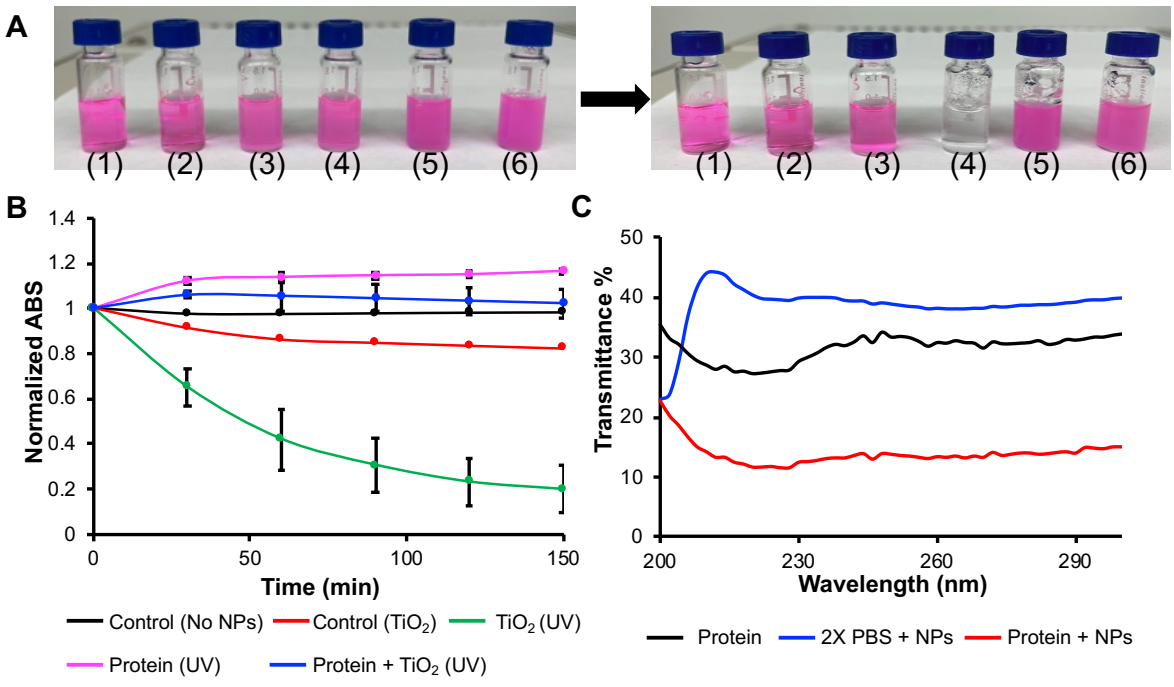

Figure 3.5 Photocatalytic activity of protein-titanium dioxide (TiO_2) nanoparticle hybrid

(A) Optical images of different samples with rhodamine B in the (1) water (2) 2X PBS under natural light, (3) 2X PBS and TiO2 nanoparticles under natural light, (4) 2X PBS and TiO_2 under UV radiation, (5) protein without nanoparticles under UV radiation, (6) protein with TiO_2 nanoparticles under UV radiation (B) Normalized absorption spectra at wavelength 554 nm (C) UV-transmittance spectra of 2X PBS with TiO_2 NPs (blue), TiO_2 in the protein solution (red), and protein only (black). Data was collected after 30 min vesicle formation.

The photodegradation experiment with TiO_2 was conducted under various sample conditions, using Rhodamine B (RhB) as a model dye to assess the reaction (Figure 3.5). RhB is a dye that initially appears pink color but loses its color upon reacting with radicals produced from TiO_2 under UV radiation. The control samples with TiO_2 but UV radiation or under UV ratio in the absence of TiO_2 did not show any photodegradation of RhB. Under UV radiation, TiO_2 without proteins exhibits the fastest photocatalytic degradation, while samples containing TiO_2-encapsulated protein cages showed only slightly increased turbidity (Figure 3.5.B). These findings suggest that TiO_2 nanoparticles were encapsulated by the protein layer, preventing the release radicals even under UV radiation. We further investigated the UV-screening property of the TiO_2-encapsulated protein cages by measuring the transmittance in the UV range from 200 nm to 300 nm (Figure 3.5.C). The hybrid sample showed the lowest UV-transmittance compared to bare TiO_2 and pure proteins, indicating superior UV-blocking capabilities. Additionally, fluorescent microscope images revealed that the presence of mCherry from the hybrid materials (Figure 3.6).

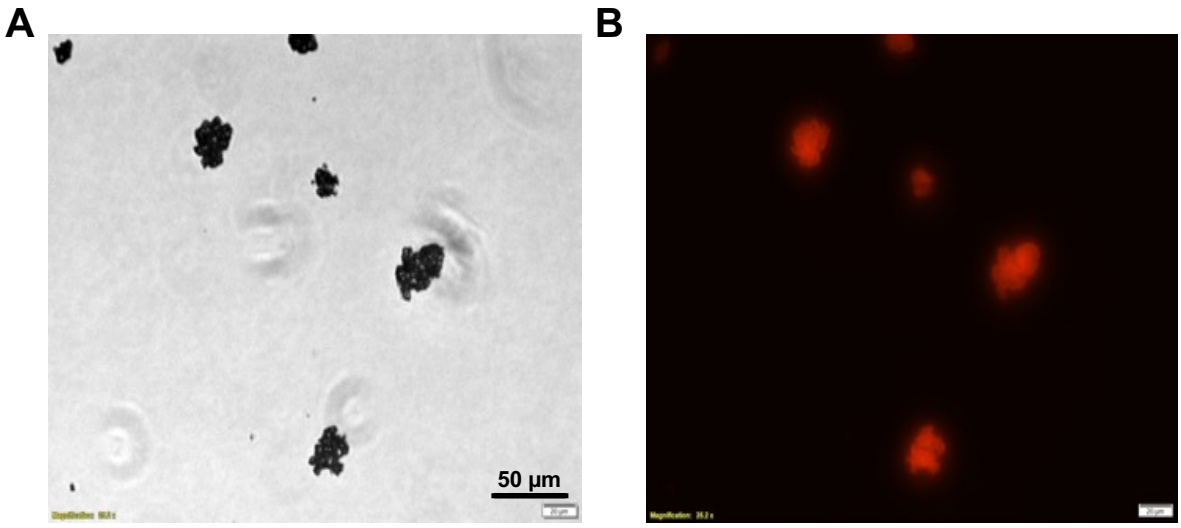

Figure 3.6 Optical microscope images of TiO_2 nanoparticles coated by mCherry-Z_E/Z_R-ELP cage, Microscope images of TiO_2 nanoparticles surrounded by engineered protein cages.

(A) Bright-field images of TiO_2 nanoparticles surrounded by engineered protein cages. (B) Image with fluorescent filter (TEXAS-RED)

3.3.5 Enhancement of Biosensing Signals through Nanoparticle Encapsulation

Lastly, we demonstrated enhanced calcium sensing using the TiO_2-encapsulated hybrid particles. TiO_2 is known for its strong light-scattering properties, due to its high refractive index, making it a valuable white pigment in various applications. This property allows TiO_2 to effectively reflect and scatter light, thereby enhancing fluorescence in biological contexts.[240,241] Previous research by the Yao group highlighted the fluorescence enhancement effect of TiO_2 in cancer detection surgeries, particularly for bladder cancer cells.[242] We hypothesize that the integration of fluorescent biosensor proteins with TiO_2-encapsulating hybrid protein cages could further amplify fluorescent intensity.

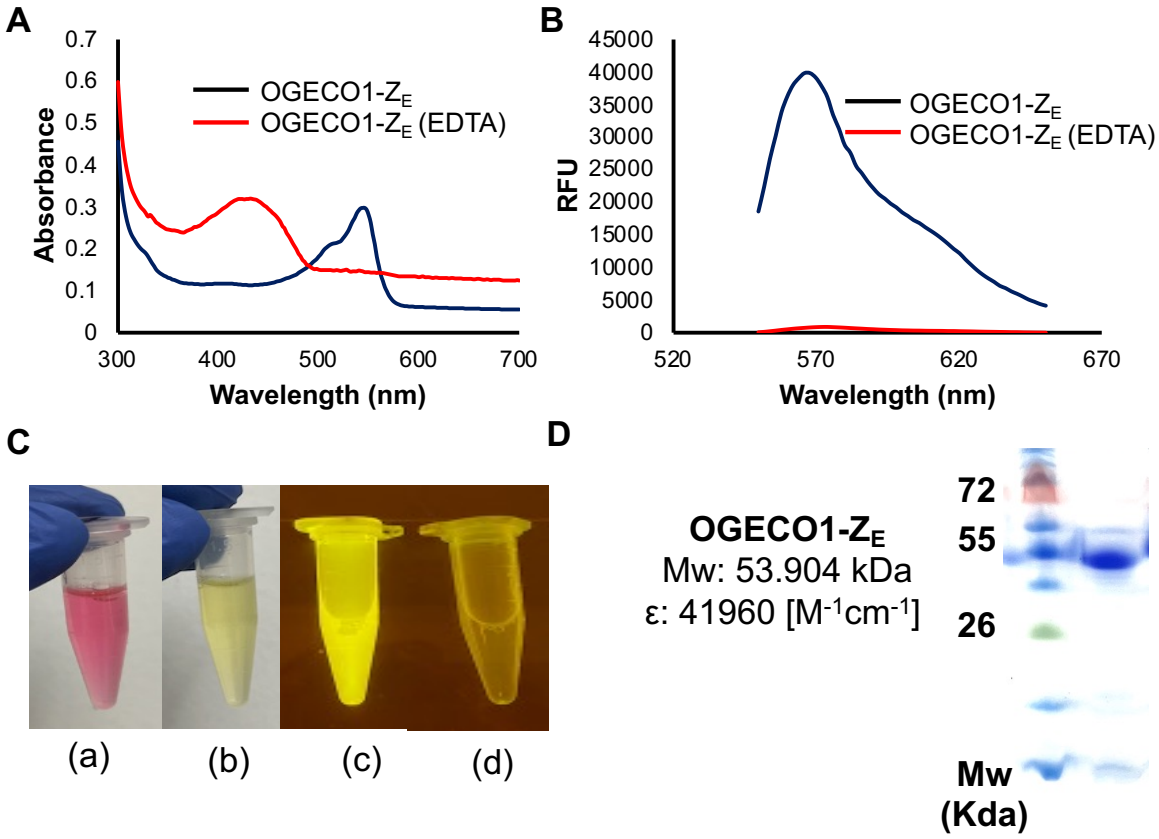

Figure 3.7 Analysis of OGEO1-Z_E

(A) Absorbance and fluorescence changes of soluble OGEO1-Z_E upon calcium ion binding. (B) Fluorescence spectra with excitation at 520 nm. The spectra were measured in the presence of Ethylenediaminetetraacetic acid (Ca^{2+}-free, red) or $CaCl_2$ (Ca^{2+}-bound, navy blue). (C) Optical images of purified OGEO1-Z_E under visible light the Ca^{2+}-free (a) and Ca^{2+}-bound state (b) and under transilluminator with Ca^{2+}-free (c) and Ca^{2+}-bound state (d). (D) SDS-PAGE analysis of purified OGEO1-Z_E The theoretical molecular weights (Mw) and extinction coefficients (ε) are provided on top of gel image.

For this, we designed the recombinant fluorescent fusion protein OGECO1-Z_E for modular assembly along with Z_R-ELP. We have confirmed absorbance and fluorescence change upon binding to Ca^{2+} (Figure 3.7.A, B and C) and verified the purity of proteins. (Figure 3.7.D) Self-assembled protein cages with a 0.05 ratio of Z_R-ELP and a fluorescent protein calcium indicator (OGECO1-Z_E) were prepared in the presence or absence of TiO_2 nanoparticles. The chelating

agent EDTA (100 μM) was added to control the concentration of free Ca^{2+}, which was calculated using the Maxchelator tool.[243] Higher concentrations of free Ca^{2+} led to enhanced fluorescence amplification (ΔF/F%) in the presence of TiO_2. (Figure 3.8.A) Specifically, at a free Ca^{2+} concentration of 0.783 nM, the protein complex without TiO_2 exhibited a ΔF/F% of 262.85 (±26.69), while the addition of TiO_2 increased this value to 850.70 (±144.38), representing more than a threefold enhancement (Figure 3.8.B). This significant increase in fluorescence intensity and sensitivity, facilitated by TiO_2 encapsulation, could serve as a foundation for developing a biosensor in future applications.

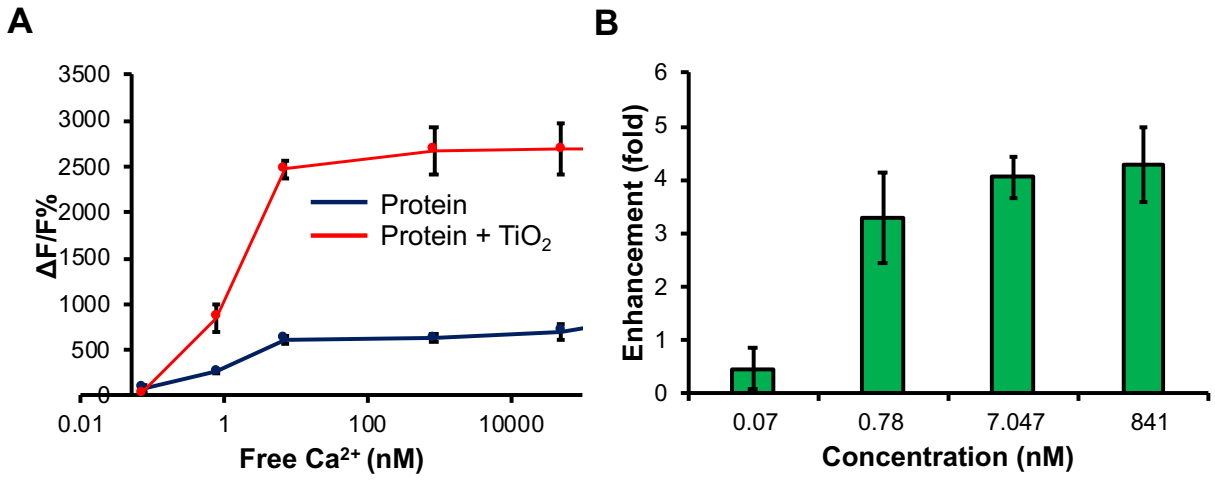

Figure 3.8 Fluorescent intensity of Z_R-ELP and OGECO1-Z_E complex with/without TiO_2
(A) Fluorescent intensity of Z_R-ELP and OGECO1-Z_E complexes with a ratio of 0.05. All samples were treated with EDTA to capture residual calcium ion. (B) Ratio of fluorescent intensity of protein with nanoparticles compared to protein alone, across different concentrations of free Ca^{2+}: 0.07 nM, 0.78 nM, 7.049 nM , 841 nM.

3.4 Conclusion

We demonstrated the cooperative self-assembly of protein cages that simultaneously encapsulate nanoparticles with high-density packing. Our analysis using fluorescent PS

nanoparticles revealed a cooperative mechanism that nanoparticles-coacervate intermediates form and subsequently convert into core-shell hybrid particles. This was further confirmed through a kinetics study. This versatile platform can be applied to various types of nanoparticles, especially TiO_2. Encapsulation of TiO_2 nanoparticles via protein self-assembly showed great promise for controlling photocatalytic activity while enhancing UV-blocking properties and significantly improving fluorescence signals when integrated with fluorescent protein calcium sensor probes. Future work will be focus on expanding the potential applications of this platform, including nanomedicine, biosensors, and bioimaging.

Chapter 4 - Development of a Nitrite Sensor Based on Fluorescent Proteins

4.1 Background and Motivation

Nitrite (NO_2^-) and nitrate (NO_3^-) play critical roles in greenhouse gas (GHG) emissions, primarily through their involvement in nitrification and denitrification processes across various ecosystems.[244] These compounds function as intermediates in the nitrogen cycle, where their inherent instability makes them highly susceptible to transformation. NO_2^- can convert into NO_3^- or ammonia, depending on the environmental conditions.[245] Nitrification is a complex process orchestrated by ammonia-oxidizing bacteria (AOB) and nitrite-oxidizing bacteria (NOB), which sequentially oxidize ammonium (NH_4^+) to NO_2^- and subsequently to NO_3^-.[246] A significant product of nitrification is nitrous oxide (N_2O), a potent greenhouse gas. Elevated nitrite levels during nitrification can trigger an escalation in N_2O production, leading to an increase in greenhouse gas emissions and contributing to global warming.[247] Notably, *Nitrosomonas europaea* stands out as an obligated chemolithoautotrophic, thriving solely on NH_3, CO, and mineral salts.[248] The enzymes ammonia monooxygenase (AMO) and hydroxylamine oxidoreductase (HAO) of *N. europaea* direct two-step oxidation of NH_3.[249] AMO converts NH_3 to hydroxyl amine (NH_2OH), and HAO then oxidizes NH_2OH to NO_2^-, which results in the production of N_2O (Figure 4.1).[250] Given the complexity of the reaction processes, detecting and quantifying NO_2^- and NO_3^- from *N. europaea* in soil is essential.

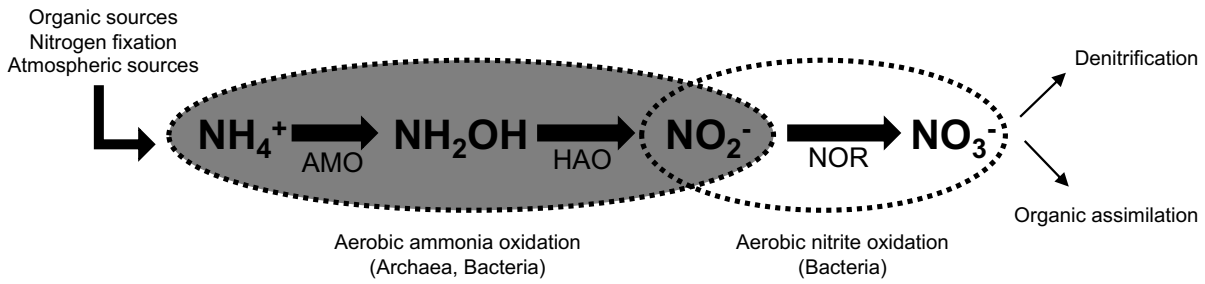

Figure 4.1 Schematic representation of aerobic ammonia oxidation during nitrification under an oxygen limiting condition. AMO, ammonia monooxygenase; HAO, hydroxylamine oxidoreductase.

In addition to their roles in the soil nitrification process, NO_2^- and NO_3^- are vital macronutrients within natural aquatic systems, where they can contribute to anthropogenic nutrient pollution that triggers harmful algal blooms and eutrophication.[251] Increased levels of NO_2^- in groundwater, rivers, and lakes pose significant risks to public health and environmental integrity.[252] A representative example is the irreversible reaction between NO_2^- and hemoglobin, which yields methemoglobin— a compound that hampers the blood's capacity to transport oxygen effectively.[253,254] This alteration in hemoglobin's functionality results in tissue hypoxia, particularly within the central nervous system. It is known for heightened susceptibility to oxygen deficiency, ultimately leading to methemoglobinemia.[252] Furthermore, excessive NO_2^- levels, often used in food preservation, can be linked to carcinogenic effects by acting as a precursor to N-nitrosamine formation.[255] This underscores the pressing need to monitor NO_2^- concentrations in water to mitigate potential adverse effects on human health.[128]

Although numerous methods for sensing NO_2^- have been reported in the literature[255–258], their direct applicable to soil environments remains limited. In our study, we employed genetically engineered fluorescent biosensors integrated into cellular systems to enable precise detection of NO_2^- through fluorescence signal transduction. We focused on monitoring intracellular NO_3^-/ NO_2^-

dynamics, using a recently developed fluorescence resonance energy transfer (FRET)-based biosensor named sNOOOPy (sensor for NO_3^-/ NO_2^- in physiology).[130] The sNOOOpy biosensor employs a regulatory protein complex called NasS-NasT, where NasS acts as the NO_3^-/NO_2^- sensor domain and NasT is a transcription antiterminator.[259] This NasS-NasT protein complex remains stable until interaction with NO_3^-/ NO_2^- triggers its dissociation, Effectively separating NasT from NasS upon analyte binding. The proteins NasT and NasS are fused with the FRET pairs cyan fluorescence protein (CFP) and yellow fluorescent protein (mVenus), respectively, creating fusion proteins CFP-NasT and NasS-mVenus. Upon binding of NO_3^-/NO_2^- to the complex of CFP-NasT/NasS-mVenus, the FRET signal changes, allowing for quantification of NO_3^-/NO_2^-. (Figure 4.2.A)

We cloned the genes for CFP-NasT and NasS-mVenus constructs in a single bacterial vector, aiming to measure the NO_2^- level in bacterial cells by quantifying FRET efficiency. (Figure 4.3.B) Alternatively, we also explored using cell extracts to develop a cost-effective and straightforward protein coating for NO_2^- sensing. This approach eliminates the need for living cells, making it suitable for low-resource settings (Figure 4.2C). Furthermore, we conducted molecular docking simulations using atomic structure models to enhance sensor performance. By examining the interactions between NO_2^- and the binding site within NasS, we gained insights that could improve binding affinity or adjust specificity for other relevant targets such as hydroxyl amine (NH_2OH).

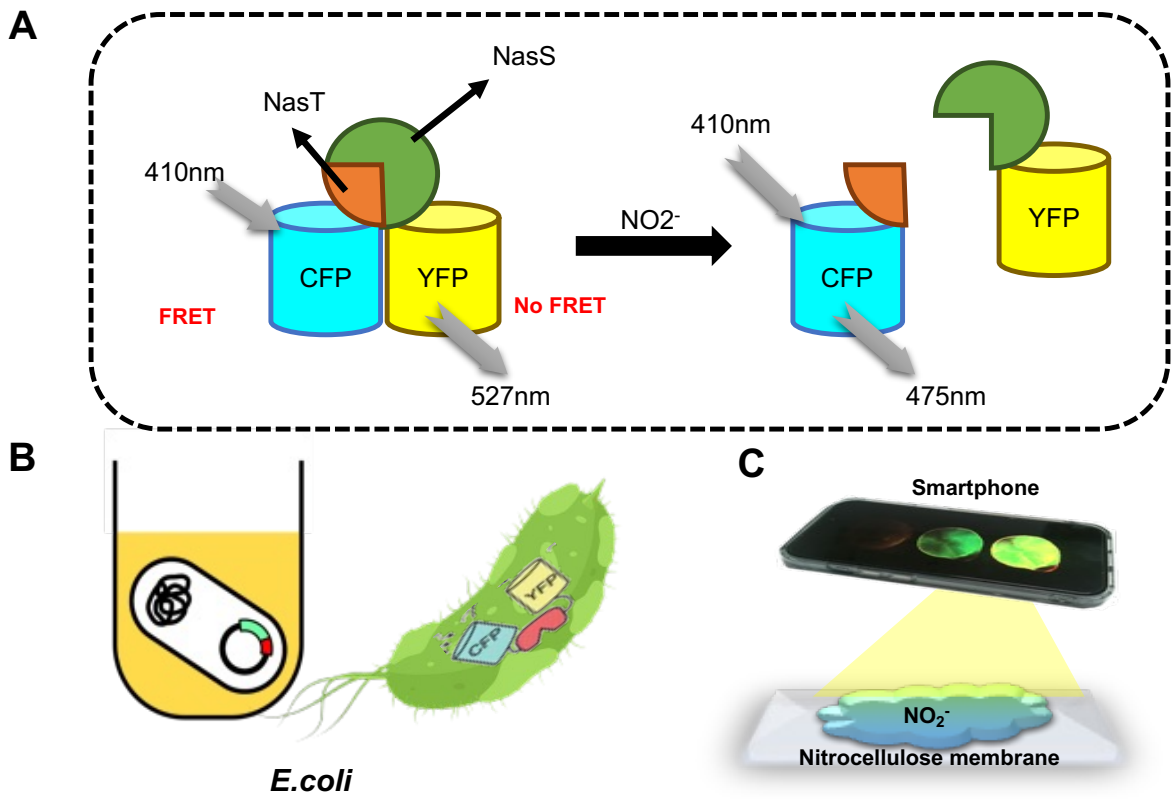

Figure 4.2 Scheme of the FRET-based nitrite sensor development

(A) Two component system with fluorescent proteins. In the proposed model, a two-component regulatory system is suggested, comprising NasS-NasT. Within this system, NasS functions as a negative regulator, exerting its influence through interaction with NasT. (B) schematic illustration showing nitrite sensor working in living cell (C) Coating fabrication process, whole cell extracts containing the protein are deposited onto nitrocellulose substrates. Protein coatings are then irradiated with a transilluminator, and the fluorescence intensity is quantified using a smartphone camera.

4.2 Materials and Methods

4.2.1 Materials

The *E. coli* strain T7 Express BL 21 was purchased from New England Biolabs. Gene synthesis and cloning were ordered from GenScript. Lysis buffer containing NaH_2PO_4 (100mM), 10 mM Tris·Cl, 6 M GuHCl were prepared in the lab. Nitrocellulose Membranes with 0.45µm pore size were purchased from Thermo Scientific.

4.2.2 Cloning and Protein Expression

The genes for CFP-NasT and NasS-mVenus[130] were synthesized and cloned into a pQE60 vector to construct the plasmid pQE60-CFP-NasT/NasS-mVenus. Gene synthesis and cloning were ordered from GenScript. The gene sequences encoding CFP-NasT and NasS-mVenus were connected by the sequence that includes ribosome binding sites (RBS) for co-expression.[29] The mVenus was circularly permuted, and a His_6-tag was added to the NasS-mVenus C-terminal only. The plasmid pQE60-CFP-NasT/NasS-mVenus was transformed into E. coli strain T7 Express cells and incubated overnight at 37°C. The transformants were grown aerobically in 8 ml of LB medium at 37°C. The overnight cultures were transferred in 250 ml 2XYT medium with 100 µg/mL at 37°C under dark conditions. Cells were harvested after -7h by centrifuging at 4000rpm for 30min. Cell pellets are resuspended in native lysis buffer and stored at -80°C.

4.2.3 Fluorescence Measurement

Fluorescence measurements were conducted using a Biotek 96-well microplate reader at 25°C. Samples were collected 3 and 7 hours after transfer to 2XYT medium, then centrifuged to remove the media and lysed with a native buffer. Following vortexing, 100 µl of each sample was loaded in triplicate to obtain average and standard deviation. The cell extract was excited at 410 nm, and fluorescence spectra were recorded from 440 to 600 nm with a 2 nm step size. To assess the sensing capability, proteins in both the absence (control) and presence of anions were analyzed. For this, 10 µl of NO_3^-/NO_2^- solutions at varying concentrations were added to 90 µl of the protein cell lysate, adjusting for the final concentration.

4.2.4 Coating Fabrication

2 mm x 2 mm pieces of nitrocellulose paper were prepared at room temperature. The cell lysates were frozen, thawed, and sonicated before application. A 20 µl drop of protein cell lysates was deposited onto the nitrocellulose paper, which was then placed on substrates and allowed to dry overnight.

4.2.5 Image Analysis

The nitrocellulose-coated proteins were placed under an LED transilluminator (BT Lab Systems) and excited at 470 nm. Fluorescence images were captured using an iPhone 13 (Apple, Inc.) with a rear camera (4000x3000 pixels). Image analysis and fluorescence quantification were performed using ImageJ software. Mean intensity values were measured in the green channel, corresponding to the transilluminator's wavelength. Quantified intensities were normalized to background intensity and averaged across the selected area. For consistency, an equally sized area was chosen from each image for analysis.

4.2.6 *In silico* Molecular Modeling of Nitrite Sensor

The structures of NasS were modelled using MODELLER v10.4 which is a tool for homology structure modelling.[260,261] The template for homology modelling was selected from NrtA (PDB ID: 2G29). A set of 10 models were generated through 5 to 15 optimization iterations and the model with the lowest z-DOPE (Discrete Optimized Protein Energy) score—an assessment method using statistical potentials—was chosen for further analysis. For molecular docking simulations, we employed Autodock Vina[262] while AutoDockTools (ADT) was used for the

preparation of both the protein and ligand. The docking grid was carefully positioned to surround the binding pocket of NasS. PyMOL supports the visualization of docking results.

4.3 Results and Discussion

4.3.1 FRET-based Measurement of Nitrite Quantification from Live Bacteria

We confirmed the expression of CFP-NasT and NasS-mVenus in *E.coli* through fluorescence measurement (Figure 4.3 A and B). Using an excitation wavelength of 410 nm, we set the CFP emission at 475 nm and the YFP emission at 527 nm. Upon excitation at 410nm, we observed a peak at 478nm and confirmed the presence of CFP. Excitation at 490 nm with an emission peak at 530 nm confirmed mVenus expression. After verifying the presence of each fluorescent protein, we examined the measurement of NO_2^-/NO_3^- concentrations within live cells by quantifying the FRET efficiency.

Our investigations have successfully confirmed that protein sensor selectively detects NO_2^- over NO_3^- in live *E. coli* cells. We expressed the proteins for 3hr and 7hr, and by measuring with an excitation wavelength of 410 nm, the YFP to CFP emission ratio (YFP/CFP) was obtained and normalized during emission scanning. (Figure 4.3C) After 3 hours of expression, the FRET ratio (YFP/CFP) decreased to 0.92 in response to 10 mM NO_2^-, while exposed to 10 mM NO_3^- resulted in almost no change in the YFP/CFP ratio. Extending the expression period to 7 hours, the YFP/CFP ratio further decreased to 0.91 with 10 mM NO_2^-, whereas no significant change was observed with 10 mM NO_3^-. Additionally, fluorescence intensity scans at 410 nm excitation indicate that higher concentrations lead to a decreased fluorescence intensity (Figure 4.3.D). We tested the NO_2^- concentration up to 100 mM, and the sensor proteins exhibited a concentration-dependent response, with increasing NO_2^- concentrations inducing dissociation of the NasS-NasT

complex. These findings further confirm the applicability of NO_2^- sensing in live bacteria using the genetically encoded FRET sensor proteins.

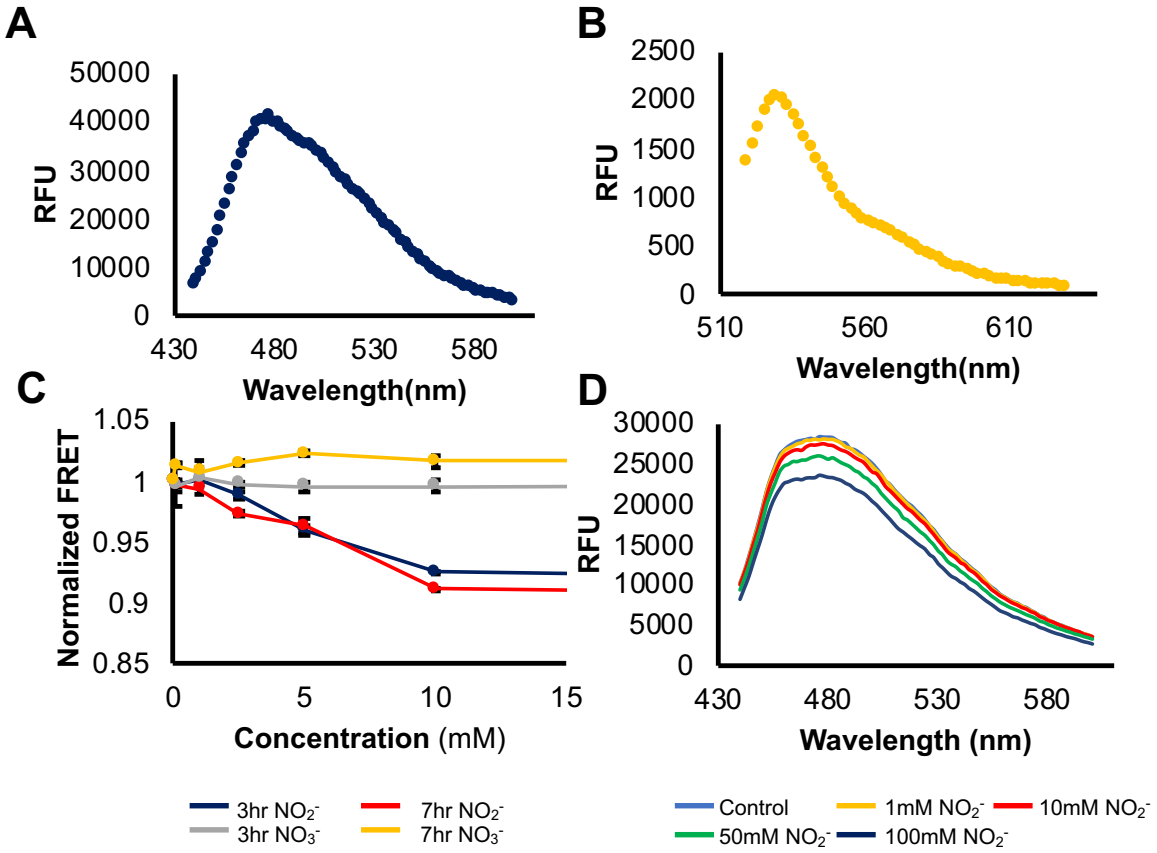

Figure 4.3 Fluorescent intensity analysis of nitrite sensor

(A) Confirmation of CFP fluorophore with 410 nm excitation. (B) Confirmation of YFP fluorophore with 490 nm excitation. (C) Monitoring of YFP/CFP ratios in live cells, showing different incubation times: 3 hours (blue for NO_2^-, gray for NO_3^-) and 7 hours (red for NO_2^-, yellow for NO_3^-) with varying anion concentrations. (D) Emission spectrum of the protein sensor with varying nitrite concentrations in living cells. The control sample contains only CFP-NasT/NasS-YFP protein.

Additionally, we attempted to engineer a single-chain fluorescent nitrite sensor protein using only the NasS protein. In this approach, the sensor domain was fused to cyan fluorescent protein (CFP) at the N-terminal and mVenus at the C-terminal, aiming to enhance FRET efficiency. Consequently, we designed the fusion protein CFP-NasS-YFP (CNasSY). However,

the results indicated no change in fluorescent intensity upon the addition of NO_2^- and NO_3^- within bacteria (Figure 4.4A). The purified CNasSY also did not react with NO_2^- and NO_3^- (Figure 4.4B).

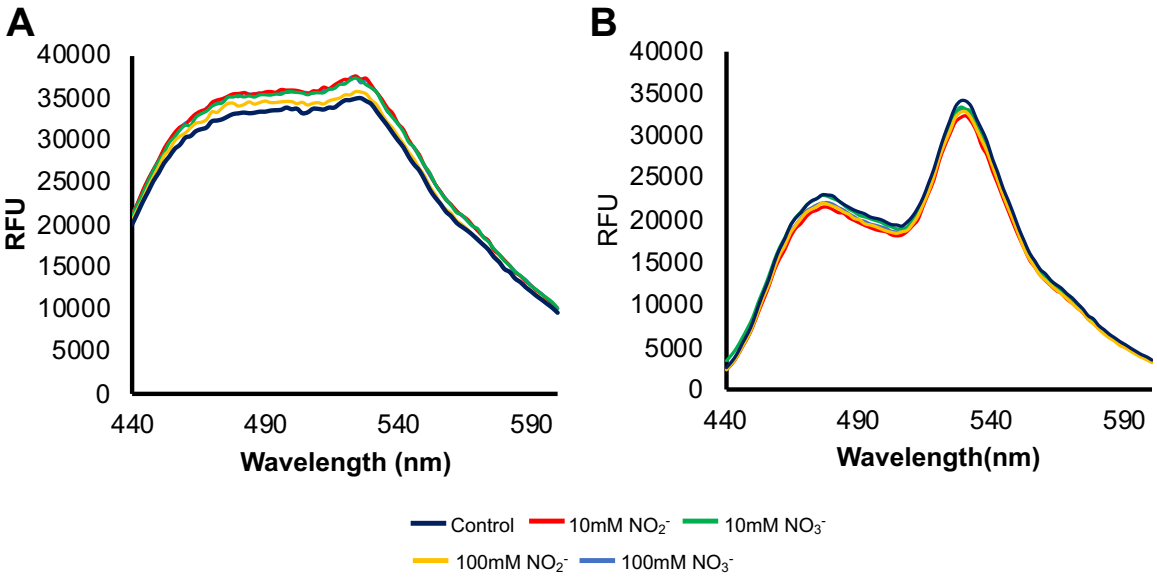

Figure 4.4 Fluorescent intensity analysis of CNasSY at excitation 410 nm

(A) Emission spectrum of CNasSY in the living cell after 7hr expression with varying concentration of NO_2^- and NO_3^- (B) Purified CNasSY with varying anion concentrations

4.3.2 Self-Assembly of Nitrite Sensor Coating

Next, we demonstrated the application of the FRET sensor proteins for creating coatings as a cost-effective biosensor device. Since the proteins function effectively in cells and purified protein is not required, we chose to use whole-cell extracts from cell pellets instead of performing protein purification. We deposited the protein extract onto the nitrocellulose membrane to create a coating, which was then placed under a transilluminator. We applied solutions of NO_2^- at varying concentrations (0, 10 mM, 20 mM, and 100 mM) and captured images using a smartphone camera. We observed a decrease in overall fluorescent intensity before and after NO_2^- binding (Figure 4.5.A). Upon adding water, there was a 59.84% (± 2.01) increase in fluorescent intensity, whereas only a 4.39% (± 8.56%) change was observed with 10 mM NO_2^- (Figure 4.5.B). This indicates that our sensor can effectively distinguish NO_2^- at millimolar levels. The fluorescence intensity profiles of the cross-sectional areas in these optical images were quantified using image analysis (Figure 4.5.C), showing clear differences between the fluorescence intensities from the wet protein coating in the presence or absence of NO_2^-. Notably, the coating with 100 mM NO_2^- exhibited the lowest intensity, consistent with the live cell fluorescence results.

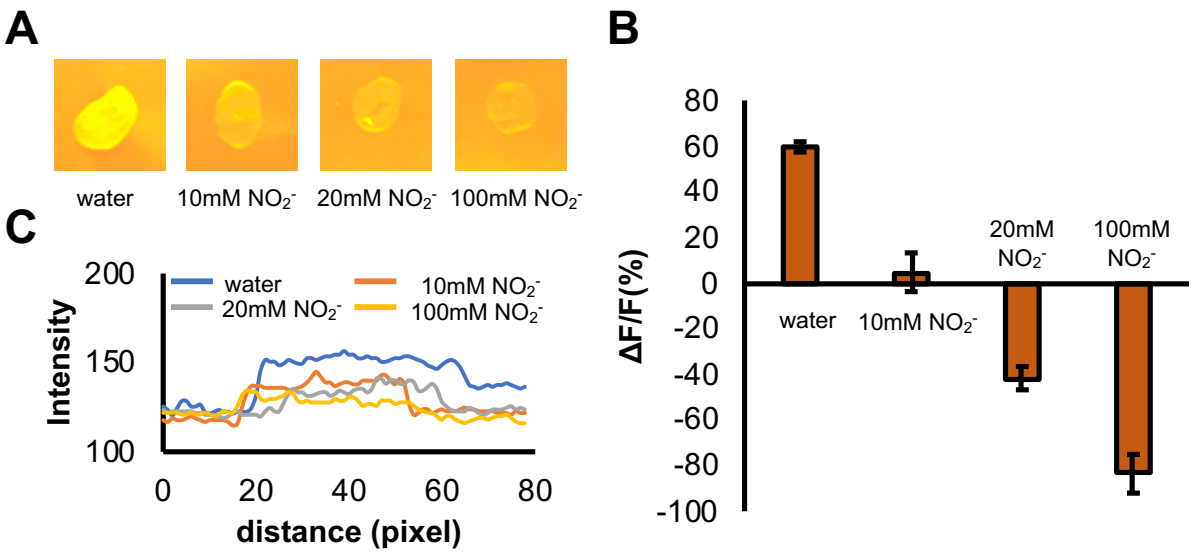

Figure 4.5 Analysis of nitrite protein sensor images

(A) A fluorescence image of the protein-coated nitrocellulose membrane under a transilluminator (B) The NO_2^- dependent fluorescent intensity changes in the range for 0 to 100mM NO_2^- (C) fluorescent intensity profile of a cross-section shown in panel (A)

4.3.3 Molecular Docking of Nitrate and Sensor Proteins

In pursuit of developing a sensor with improved specificity for NO_2^- binding, we conducted *in silico* molecular modeling to understand the interactions between NasS and NO_2^-. We verified that several significant interactions were observed between NO_3^- and NrtA, corresponding to those between NasS and NO_2^- through molecular docking simulation. NrtA[101,133], a protein that binds to NO_3^- is homologous to NasS, with the ability to bind to NO_3^-/ NO_2^- (Figure 4.6.A).[130] Using the crystal structure of NrtA (PDB ID: 2G29)[101,133] we conducted homology modeling of the NasS structure using Modeller software.[260] Subsequently, we conduct molecular docking of both NO_3^- and NO_2^- using Autodock Vina[263] and aligned with NrtA. (Figure 4.6.B).

Literature indicates that the interaction between the oxygen within NO_3^- and H196 of NrtA, corresponding to H145 of NasS, is important for the protein-ligand interaction (Figure

4.6.C).[101,130,133] Further contributions to binding affinity were attributed to residues W102, K269 and V239 of NrtA, which correspond to W42, K218 and V188 of NasS. Residues Q155 and G240 in NrtA are absent in NasS. Despite the sequence difference between NrtA and NasS, modeling identified the residues involved in NO_2^- binding: W42, N89, H145, V188, E177, and K218 in NasS (Figure 4.6.D and E). Notably, W42, N89, H145, and K218 form hydrogen bonds with NO_2^-. Specifically, H145 forms hydrogen bonds with two oxygen atoms of NO_2^-, while H145 and K269 help to neutralize the negative charge on oxygen of the NO_3^-, thereby assisting in the polarization of the NO_3^- anion.

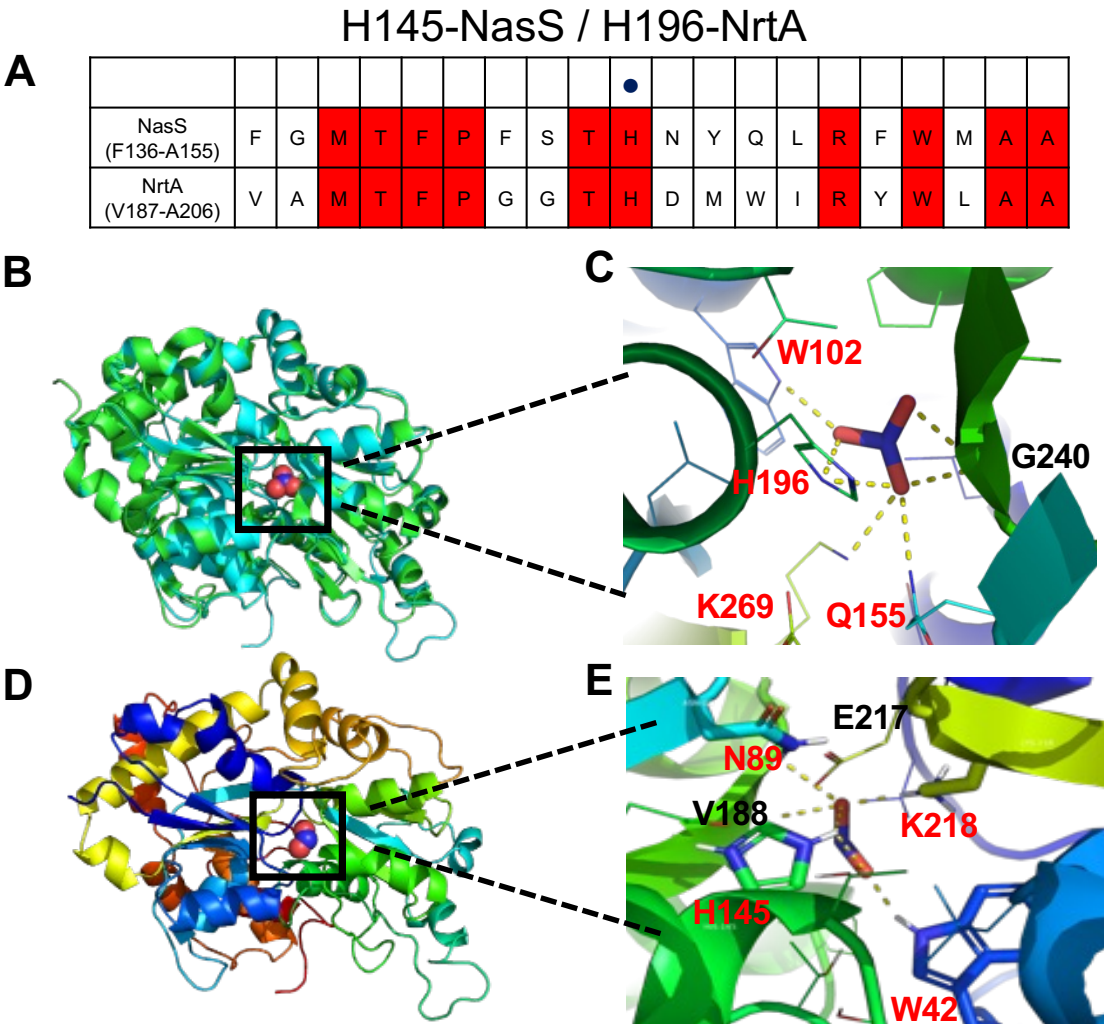

Figure 4.6 Structural analysis of NO_2^-/NO_3^- binding proteins

(A) Amino acid sequence alignment between NasS and NrtA (B) Homologous structures of NasS and NrtA, visualized using PyMOL. Alignment of NrtA (PDB ID: 2g29) with the modeled NasS domain. NrtA is shown in green, while NasS is depicted in cyan. (C) Schematic representation of the NO_3^- -binding site, illustrating protein-ligand interactions between NrtA and nitrate. Dashed lines indicate potential hydrogen-bonding and electrostatic interactions. (D) Schematic representation of the modeled NasS protein and molecular docking results. (E) The predicted binding site of NasS with NO_2^-, with oxygen atoms shown in red and nitrogen atoms in blue.

To assess the role of the H145 residue in our modeled NasS domain, we prepared a NasS-H145A mutant, which is predicted to interfere with a NO_2^- binding site. We then conducted molecular docking simulations to explore this interaction (Figure 4.7). The binding pocket location in the mutant shifted from that in the wild-type NasS protein, affecting residues such as W42, N89, and K218, which are crucial for NasS and NO_2^- binding. Additionally, the mutant protein exhibited direct interactions with residues N146 and Q324. These findings underscore the critical role of H145 in NO_2^- binding within the NasS structure.

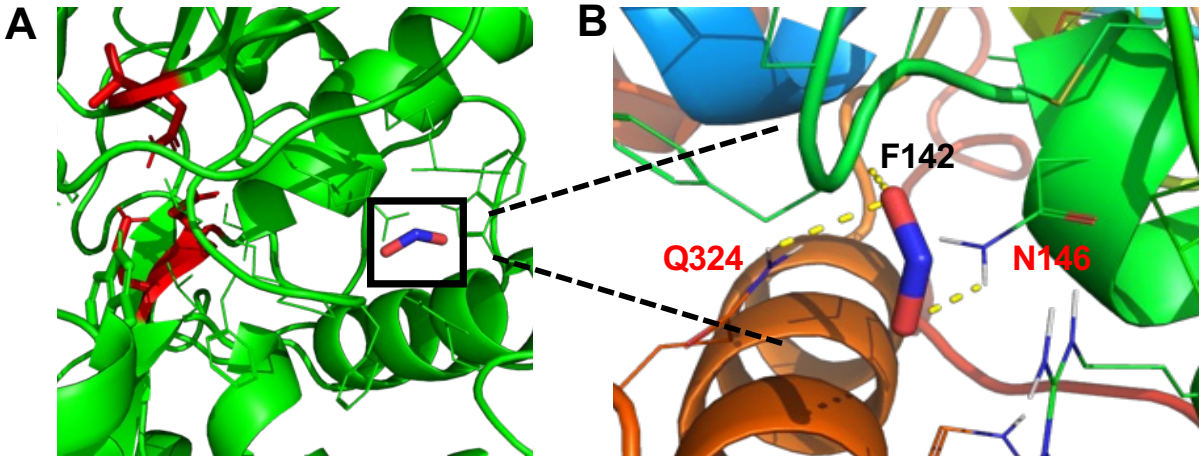

Figure 4.7 Modeling and molecular docking studies of the NasS-H145A mutant

(A) 3D schematic diagram of the NasS-H145A mutant structure bound with nitrite (NO_2^-), highlighting a different binding location compared to previous studies. Red residues indicate the original NasS binding pocket, including W42, N89, and K218. (B) Detailed view of the NasS-H145A binding site with nitrite, illustrating direct hydrogen/electrostatic bonds. Oxygen atoms are shown in red and nitrogen atoms in blue.

4.3.4 Molecular Insights for the Design of a Hydroxylamine Sensor

In the previous chapter, we predicted the specific molecular interactions between NO_2^- and NasS through molecular docking simulations. Building on these findings, our goal is to achieve specific binding of NasS to hydroxylamine (NH_2OH) for new sensor development as

hydroxylamine is produced from ammonia through the action of AMO in ammonia-oxidizing bacteria in the soil environments. While many research groups have developed hydroxylamine sensing methods using chemical probes[264,265], electrochemical techniques[266], and gas chromatography[267], these approaches do not enable real-time monitoring of hydroxylamine within cells. Therefore, our research focuses on developing a protein-based fluorescent hydroxylamine sensor that allows for real-time monitoring inside bacteria, utilizing computational molecular docking to identify protein domains with unique NH_2OH-binding properties.

Our docking results revealed that only the E217 residue of NasS directly interacts with the hydrogen of NH_2OH, while other residues in the vicinity—T144, H145, Q148, and L212—are involved in indirect interactions. (Figure 4.8) To enhance binding affinity to the NH_2OH molecule, we propose point mutations of the indirectly interacting residues. Given that the hydrogen bond between NH_2OH and E217, which has a negatively charged side chain, is particularly strong, we suggest mutating T144 and Q148, which have polar uncharged residues, to T144E, Q148E, or T144D, Q148E. Additionally, changing H145, a positively charged residue, to H145D or H145A may improve binding to the hydrogen molecule. We also propose mutating L212 to L212D or L212E to potentially increase binding affinity.

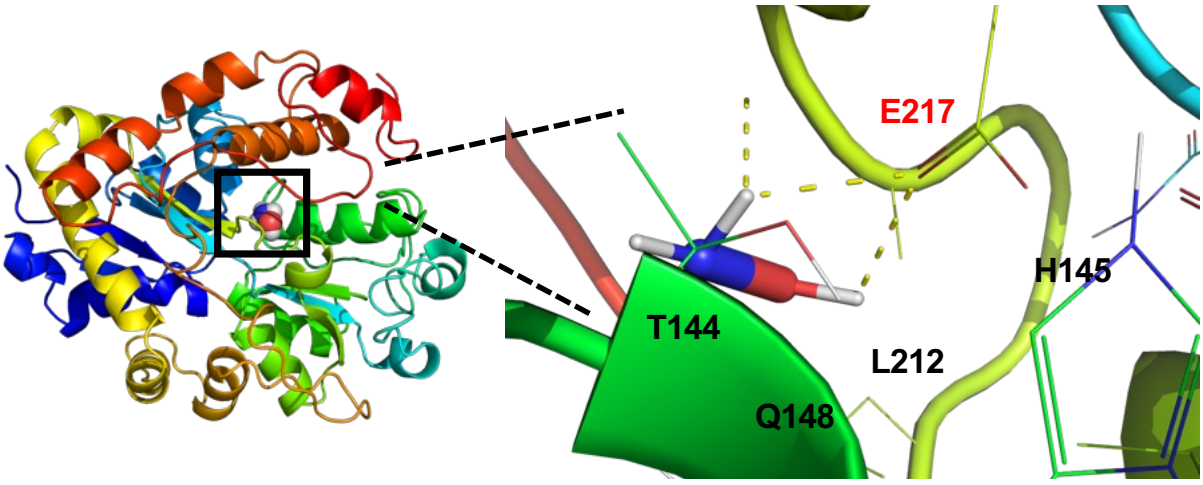

Figure 4.8 Molecular docking simulation of NasS with NH_2OH

(A) 3D illustration of the predicted binding site between the nitrite-sensing domain of NasS and hydroxylamine (B) Detailed view of the binding interaction, highlighting key residues involved in the binding, specifically E217.

Single amino acid changes can often disrupt the intricate network of intramolecular interactions, potentially affecting protein folding, stability, dynamics, and function. Therefore, we also aimed to predict the impact of the proposed mutations on protein stability. To achieve this, we utilized Dynamut2, a web server that employs machine learning to calculate changes in Gibbs free energy and assess the effects of missense mutations on protein stability.[268] We mutated residues T144, H145, Q148, and L212 to alanine, aspartic acid, and glutamic acid. The results indicated that mutations T144E, H145E, and Q148E exhibited significantly lower destabilizing effects (Table 4.2), prompting us to perform molecular docking with these variants.

Mutation	$\Delta\Delta G^{stability}$ (kcal/mol)	Mutation	$\Delta\Delta G^{stability}$ (kcal/mol)
H145A	-2.2	Q148A	-0.37
H145D	-2.5	Q148D	-1.98
H145E	-2.58	Q148E	-0.15
T144A	-1.5	L212A	-2.85
T144D	-0.67	L212D	-2.75
T144E	-0.67	L212E	-2.7

Table 4.1 Mutation details with predicted stability change from DynaMut2.
The predicted effect of a mutation in stability and dynamics is given as the variation in Gibbs Free Energy (in kcal/mol).

While Q148E did not show any direct interaction between the protein and NH_2OH (Figure 4.9A), the T144D mutant displayed one direct interaction with D14 and the hydrogen of NH_2OH, along with indirect interactions involving oxygen with V13 or G88 (Figure 4.9B). In the T144E mutant, we observed increased interactions between NH_2OH and the protein: the hydrogen connected to nitrogen interacted with D14 and N89, while the oxygen engaged with W314 (Figure 4.9C and D). Overall, these results suggest that mutating the NasS domain to subtly alter protein dynamic stability can enhance interactions between NH_2OH and the protein. Additionally, the binding affinity energy between NasS and NH_2OH supports this conclusion (Table 4.2). The affinity of the wild-type NasS protein for NH_2OH is -2.1 kcal/mol, while the mutated protein demonstrates a lower energy state, particularly the T144E mutation, which shows the most promising tight binding with the lowest energy of -2.9 kcal/mol. Therefore, our approach using

molecular docking simulations indicates a promising strategy to design NasS for the development of an NH_2OH sensor.

Mutation	Affinity (kcal/mol)
Wild type	-2.1
Q148E	-2.8
T144D	-2.8
T144E	-2.9

Table 4.2 Affinity binding value between NasS and NH_2OH from Autodock Vina.

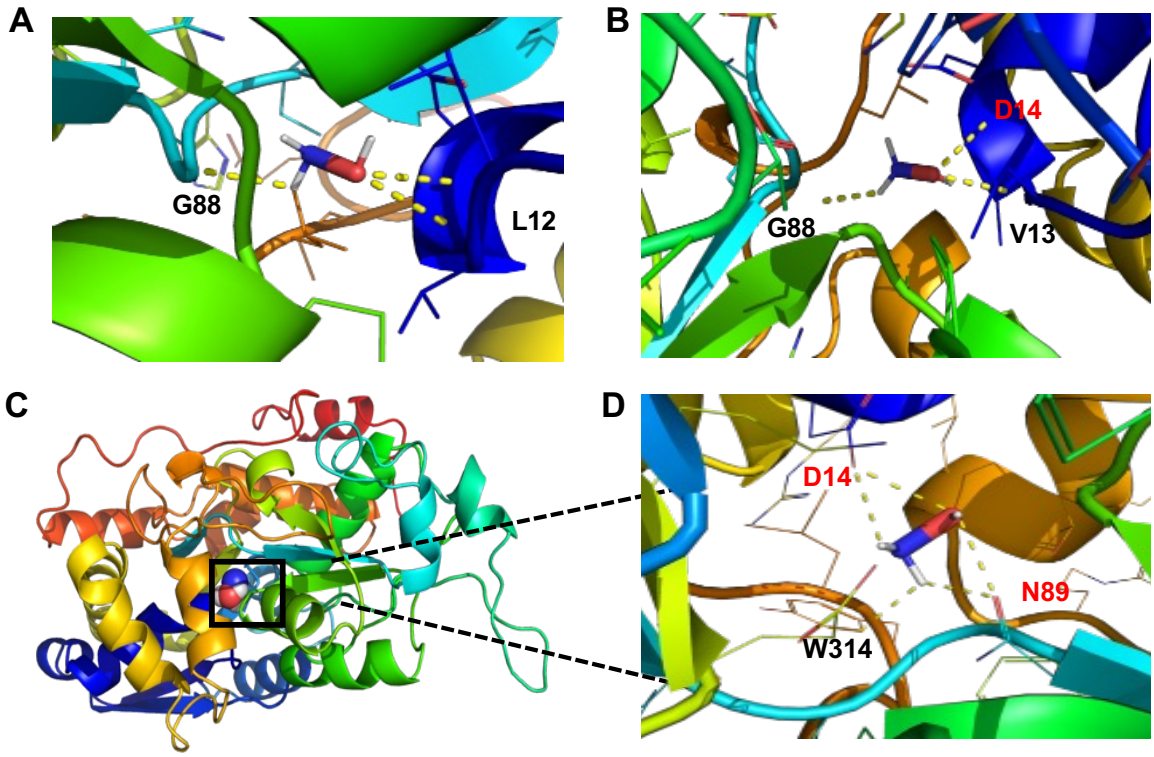

Figure 4.9 Molecular docking simulation of NasS mutants with hydroxylamine (NH_2OH)

(A) Predicted binding interaction between NasS-Q148E and NH_2OH, with oxygen shown in red, nitrogen in blue, and hydrogen in gray. (B) Predicted binding interaction between NasS-T144D and NH_2OH. (C) 3D illustration of the modeled structure NasS-T144E and its molecular docking results with NH_2OH. (D) Close-up view of the T144E mutant and its interactions with NH_2OH, which includes D14 and N89 residue for hydrogen of NH_2OH.

4.4 Conclusion

In summary, employing genetically engineered fluorescent biosensors, we demonstrated a FRET system to measure intracellular NO_2^- concentrations. Notably, the findings have highlighted the sensitivity of the sensor within living cells, particularly at the 10 mM NO_2^- concentration during both 3-hour and 7-hour expression periods. We also developed a NO_2^-sensor device based on protein coating on nitrocellulose paper using a straightforward drop-casting method. The nitrite sensor coatings detected changes in fluorescent intensity within the millimolar concentration

range. Additionally, molecular docking studies provided valuable insights into molecular interactions, guiding future advancements in sensor technology and environmental monitoring. Future work will explore other targets, such as NH_2OH, leveraging novel designs and computational structural analysis. Overall, this study established a foundation for the development of fluorescent protein sensors for NO_2^- specific binding, which could potentially enhance our understanding of nitrification processes and contribute to mitigating GHG emissions.

Chapter 5 - Conclusions and Future Outlook

5.1 Conclusions

This dissertation describes the processes of protein self-assembly with a focus on engineering biosensors through strategies that incorporate of functional proteins. Recombinant protein building blocks, inspired by biomimetic motifs, were engineered to create microstructured functional coating materials. Additionally, various sensor protein domains with fluorescence functionality were generated and assembled into protein-based biomaterials that exhibit enhanced performance. The notable feature of this approach is its modular design, which facilitates the integration of functional domains, including fluorescent proteins combined with various sensing domains. Moreover, the ability to control protein material morphologies, such as coatings or cages provides a foundation for cost-effective and straightforward fabrication for biosensing platforms.

We demonstrated a robust platform for high-density, stable, and versatile protein coating self-assembly using modularly designed recombinant proteins. By incorporating fluorescent calcium sensor domains, this protein coating was developed for biosensor applications, particularly for calcium-sensing relevant to hypercalcemia. Next, we explored the fundamentals of self-assembly in nanoparticle-encapsulating hybrid protein cages, demonstrating how incorporating nanoparticles can amplify sensor capabilities. Lastly, we studied a nitrite sensor within living cells based on the FRET. Our experiments confirmed the concentration-dependent behavior and sensing ability of the protein sensors and also elucidated the interactions with the analytes by molecular docking simulations. These findings will enhance the sensing capabilities for monitoring of nitrification-related greenhouse gas emissions.

5.2 Future Outlook

5.2.1 Clinical Test using a Protein-Based Calcium Sensing Coating

A simple and cost-effective way of protein-coated biosensor was achieved through protein self-assembly. The extended application of the biosensor is hypercalcemia-related cancer detection. Future studies may focus on validating the sensor performance with experiments using clinical samples. Additionally, by leveraging microneedle substrates, the calcium sensing coating can also be applied to develop a highly sensitive and minimally invasive diagnostic tool. The integration of microneedle sensors has the potential enhance the diagnostic capabilities for hypercalcemia related cancer, ultimately improving patient outcomes through more accessible and affordable testing methods. Moreover, the use of calcium sensor proteins with distinct color variations, which distinguish calcium ion binding state under visible light or allow deep tissue penetration, simplifies its use in point-of-care settings and practical applications.

5.2.2 Encapsulation of Various Types of Nanoparticles

We investigated the morphology control and encapsulation mechanism of nanoparticles within protein hybrid. Future research may explore the integration of various cargo, such as iron oxide nanoparticles and quantum dots. Extending this nanoparticle encapsulation platform to living organisms, including bacteria, is also recommended for the future work. One potential approach involves introducing fluorescent bacteria with metal ions and His_6-Z_E/Z_R-ELP into the existing protein self-assembly system. The outer membrane of bacteria, primarily composed of lipopolysaccharides (LPS) with negatively charged functional groups, has a natural affinity for metal ions that interact with histidine residues. This interaction may facilitate the formation of bacterial particles, which could then be encapsulated within a protein cage.

5.2.3 Developing NH_2OH Sensor for Environmental Monitoring

In chapter 4, we developed a straightforward fabrication method for nitrite ion sensor which is functioning in moisture-rich conditions. As a step forward, it is recommended to assess its sensing capability in agricultural water, using changes in FRET efficiency to quantify NO_2^- level in the water samples. In addition, we proposed mutations for a potential design of NH_2OH sensor based on the molecular docking simulation. Future work may involve designing new sensors and evaluating NH_2OH sensing ability by quantifying FRET efficiency. Our approach is expected to advance the development of strategies for managing nitrification and improving environmental sustainability.

References or Bibliography

(1) King, N. P.; Sheffler, W.; Sawaya, M. R.; Vollmar, B. S.; Sumida, J. P.; André, I.; Gonen, T.; Yeates, T. O.; Baker, D. Computational Design of Self-Assembling Protein Nanomaterials with Atomic Level Accuracy. *Science.* **2012**, *336* (6085), 1171–1174. https://doi.org/10.1126/science.1219364.

(2) Pieters, B. J. G. E.; Van Eldijk, M. B.; Nolte, R. J. M.; Mecinović, J. Natural Supramolecular Protein Assemblies. *Chem. Soc. Rev.* **2016**, *45* (1), 24–39. https://doi.org/10.1039/c5cs00157a.

(3) Beloqui, A.; Cortajarena, A. L. Protein-Based Functional Hybrid Bionanomaterials by Bottom-up Approaches. *Curr. Opin. Struct. Biol.* **2020**, *63*, 74–81. https://doi.org/10.1016/j.sbi.2020.04.005.

(4) Abbas, M.; Zou, Q.; Li, S.; Yan, X. Self-Assembled Peptide- and Protein-Based Nanomaterials for Antitumor Photodynamic and Photothermal Therapy. *Adv. Mater.* **2017**, *29* (12). https://doi.org/10.1002/adma.201605021.

(5) Luo, Q.; Hou, C.; Bai, Y.; Wang, R.; Liu, J. Protein Assembly: Versatile Approaches to Construct Highly Ordered Nanostructures. *Chem. Rev.* **2016**, *116* (22), 13571–13632. https://doi.org/10.1021/acs.chemrev.6b00228.

(6) Javid, N.; Roy, S.; Zelzer, M.; Yang, Z.; Sefcik, J.; Ulijn, R. V. Cooperative Self-Assembly of Peptide Gelators and Proteins. *Biomacromolecules* **2013**, *14* (12), 4368–4376. https://doi.org/10.1021/bm401319c.

(7) Urry, D. W.; Luan, C.; Parker, T. M.; Gowda, D. C.; Prasad, K. U.; Reid, M. C. Temperature of Polypeptide Inverse Temperatrue Transition Depends on Mean Residue Hydrophobicity. *J. Am. Chem. Soc.* **1991**, *113* (9), 4346–4348.

(8) Webber, M. J.; Appel, E. A.; Meijer, E. W.; Langer, R. Supramolecular Biomaterials. *Nat. Mater.* **2015**, *15* (1), 13–26. https://doi.org/10.1038/nmat4474.

(9) Zhang, S. Fabrication of Novel Biomaterials through Molecular Self-Assembly. *Nat. Biotechnol.* **2003**, *21* (10), 1171–1178. https://doi.org/10.1038/nbt874.

(10) Yadav, S.; Sharma, A. K.; Kumar, P. Nanoscale Self-Assembly for Therapeutic Delivery. *Front. Bioeng. Biotechnol.* **2020**, *8* (February), 1–24. https://doi.org/10.3389/fbioe.2020.00127.

(11) Fu, X.; Cai, J.; Zhang, X.; Li, W. Di; Ge, H.; Hu, Y. Top-down Fabrication of Shape-Controlled, Monodisperse Nanoparticles for Biomedical Applications. *Adv. Drug Deliv. Rev.* **2018**, *132*, 169–187. https://doi.org/10.1016/j.addr.2018.07.006.

(12) Ianiro, A.; Wu, H.; van Rijt, M. M. J.; Vena, M. P.; Keizer, A. D. A.; Esteves, A. C. C.; Tuinier, R.; Friedrich, H.; Sommerdijk, N. A. J. M.; Patterson, J. P. Liquid–Liquid Phase Separation during Amphiphilic Self-Assembly. *Nat. Chem.* **2019**, *11* (4), 320–328.

https://doi.org/10.1038/s41557-019-0210-4.

(13) Peng, Z.; Peralta, M. D. R.; Cox, D. L.; Toney, M. D. Bottom-up Synthesis of Protein-Based Nanomaterials from Engineered β-Solenoid Proteins. *PLoS One* **2020**, *15* (2), 1–17. https://doi.org/10.1371/journal.pone.0229319.

(14) Cosert, K. M.; Castro-Forero, A.; Steidl, R. J.; Worden, R. M.; Reguera, G. Bottom-up Fabrication of Protein Nanowires via Controlled Self-Assembly of Recombinant Geobacter Pilins. *MBio* **2019**, *10* (6). https://doi.org/10.1128/mBio.02721-19.

(15) Sasso, L.; Suei, S.; Domigan, L.; Healy, J.; Nock, V.; Williams, M. A. K.; Gerrard, J. A. Versatile Multi-Functionalization of Protein Nanofibrils for Biosensor Applications. *Nanoscale* **2014**, *6* (3), 1629–1634. https://doi.org/10.1039/c3nr05752f.

(16) Leng, Y.; Wei, H. P.; Zhang, Z. P.; Zhou, Y. F.; Deng, J. Y.; Cui, Z. Q.; Men, D.; You, X. Y.; Yu, Z. N.; Luo, M.; Zhang, X. E. Integration of a Fluorescent Molecular Biosensor into Self-Assembled Protein Nanowires: A Large Sensitivity Enhancement. *Angew. Chemie - Int. Ed.* **2010**, *49* (40), 7243–7246. https://doi.org/10.1002/anie.201002452.

(17) Jordan, P. C.; Patterson, D. P.; Saboda, K. N.; Edwards, E. J.; Miettinen, H. M.; Basu, G.; Thielges, M. C.; Douglas, T. Self-Assembling Biomolecular Catalysts for Hydrogen Production. *Nat. Chem.* **2016**, *8* (2), 179–185. https://doi.org/10.1038/nchem.2416.

(18) Mitchison, T. J.; Biol, J. C.; Kelleher, J. F.; Atkinson, S. J.; Pollard, T. D.; Biol, J. C.; Hartgerink, J. D.; Beniash, E.; Stupp, S. I. Self-Assembly and Mineralization of Peptide-Amphiphile Nanofibers. **2001**, *294* (November), 1684–1688.

(19) Yu, Y.; Jiang, X.; Gong, S.; Feng, L.; Zhong, Y.; Pang, Z. The Proton Permeability of Self-Assembled Polymersomes and Their Neuroprotection by Enhancing a Neuroprotective Peptide across the Blood-Brain Barrier after Modification with Lactoferrin. *Nanoscale* **2014**, *6* (6), 3250–3258. https://doi.org/10.1039/c3nr05196j.

(20) Sinha, N. J.; Langenstein, M. G.; Pochan, D. J.; Kloxin, C. J.; Saven, J. G. Peptide Design and Self-Assembly into Targeted Nanostructure and Functional Materials. *Chem. Rev.* **2021**, *121* (22), 13915–13935. https://doi.org/10.1021/acs.chemrev.1c00712.

(21) Lai, Y. T.; King, N. P.; Yeates, T. O. Principles for Designing Ordered Protein Assemblies. *Trends Cell Biol.* **2012**, *22* (12), 653–661. https://doi.org/10.1016/j.tcb.2012.08.004.

(22) Jang, Y.; Choi, W. T.; Heller, W. T.; Ke, Z.; Wright, E. R.; Champion, J. A. Engineering Globular Protein Vesicles through Tunable Self-Assembly of Recombinant Fusion Proteins. *Small* **2017**, *13* (36), 1–9. https://doi.org/10.1002/smll.201700399.

(23) Le, D. H. T.; Sugawara-Narutaki, A. Elastin-like Polypeptides as Building Motifs toward Designing Functional Nanobiomaterials. *Mol. Syst. Des. Eng.* **2019**, *4* (3), 545–565. https://doi.org/10.1039/c9me00002j.

(24) Cao, M.; Shen, Y.; Wang, Y.; Wang, X.; Li, D. Self-Assembly of Short Elastin-like Amphiphilic Peptides: Effects of Temperature, Molecular Hydrophobicity and Charge Distribution. *Molecules* **2019**, *24* (1). https://doi.org/10.3390/molecules24010202.

(25) Sallach, R. E.; Cui, W.; Wen, J.; Martinez, A.; Conticello, V. P.; Chaikof, E. L. Elastin-Mimetic Protein Polymers Capable of Physical and Chemical Crosslinking. *Biomaterials* **2009**, *30* (3), 409–422. https://doi.org/10.1016/j.biomaterials.2008.09.040.

(26) Kowalczyk, T.; Hnatuszko-Konka, K.; Gerszberg, A.; Kononowicz, A. K. Elastin-like Polypeptides as a Promising Family of Genetically-Engineered Protein Based Polymers. *World J. Microbiol. Biotechnol.* **2014**, *30* (8), 2141–2152. https://doi.org/10.1007/s11274-014-1649-5.

(27) Christensen, T.; Hassouneh, W.; Trabbic-Carlson, K.; Chilkoti, A. Predicting Transition Temperatures of Elastin-like Polypeptide Fusion Proteins. *Biomacromolecules* **2013**, *14* (5), 1514–1519. https://doi.org/10.1021/bm400167h.

(28) Sing, M. K.; Burghardt, W. R.; Olsen, B. D. Influence of End-Block Dynamics on Deformation Behavior of Thermoresponsive Elastin-like Polypeptide Hydrogels. *Macromolecules* **2018**, *51* (8), 2951–2960.https://doi.org/10.1021/acs.macromol.8b00002.

(29) Park, W. M.; Champion, J. A. Thermally Triggered Self-Assembly of Folded Proteins into Vesicles. *J. Am. Chem. Soc.* **2014**, *136* (52), 17906–17909. https://doi.org/10.1021/ja5090157.

(30) Bellingham, C. M.; Lillie, M. A.; Gosline, J. M.; Wright, G. M.; Starcher, B. C.; Bailey, A. J.; Woodhouse, K. A.; Keeley, F. W. Recombinant Human Elastin Polypeptides Self-Assemble into Biomaterials with Elastin-Like Properties. *Biopolymers* **2003**, *70* (4), 445–455. https://doi.org/10.1002/bip.10512.

(31) Costa, S. A.; Simon, J. R.; Amiram, M.; Tang, L.; Zauscher, S.; Brustad, E. M.; Isaacs, F. J.; Chilkoti, A. Photo-Crosslinkable Unnatural Amino Acids Enable Facile Synthesis of Thermoresponsive Nano- to Microgels of Intrinsically Disordered Polypeptides. *Adv. Mater.* **2018**, *30* (5), 1–9. https://doi.org/10.1002/adma.201704878.

(32) Macewan, S. R.; Chilkoti, A. Applications of Elastin-like Polypeptides in Drug Delivery. *J. Control. Release* **2014**, *190*, 314–330. https://doi.org/10.1016/j.jconrel.2014.06.028.

(33) Nettles, D. L.; Chilkoti, A.; Setton, L. A. Applications of Elastin-like Polypeptides in Tissue Engineering. *Adv. Drug Deliv. Rev.* **2010**, *62* (15), 1479–1485. https://doi.org/10.1016/j.addr.2010.04.002.

(34) Dash, B. C.; Thomas, D.; Monaghan, M.; Carroll, O.; Chen, X.; Woodhouse, K.; O'Brien, T.; Pandit, A. An Injectable Elastin-Based Gene Delivery Platform for Dose-Dependent Modulation of Angiogenesis and Inflammation for Critical Limb Ischemia. *Biomaterials* **2015**, *65*, 126–139. https://doi.org/10.1016/j.biomaterials.2015.06.037.

(35) Lampe, K. J.; Antaris, A. L.; Heilshorn, S. C. Design of Three-Dimensional Engineered

Protein Hydrogels for Tailored Control of Neurite Growth. *Acta Biomater.* **2013**, *9* (3), 5590–5599. https://doi.org/10.1016/j.actbio.2012.10.033.

(36) Koria, P.; Yagi, H.; Kitagawa, Y.; Megeed, Z.; Nahmias, Y.; Sheridan, R.; Yarmush, M. L. Self-Assembling Elastin-like Peptides Growth Factor Chimeric Nanoparticles for the Treatment of Chronic Wounds. *Proc. Natl. Acad. Sci. U. S. A.* **2011**, *108* (3), 1034–1039. https://doi.org/10.1073/pnas.1009881108.

(37) Riziotis, I. G.; Lamprou, P.; Papachristou, E.; Mantsou, A.; Karolidis, G.; Papi, R.; Choli-Papadopoulou, T. De Novo Synthesis of Elastin-like Polypeptides (ELPs): An Applied Overview on the Current Experimental Techniques. *ACS Biomater. Sci. Eng.* **2021**, *7* (11), 5064–5077. https://doi.org/10.1021/acsbiomaterials.1c00329.

(38) Wang, H.; Cai, L.; Paul, A.; Enejder, A.; Heilshorn, S. C. Hybrid Elastin-like Polypeptide-Polyethylene Glycol (ELP-PEG) Hydrogels with Improved Transparency and Independent Control of Matrix Mechanics and Cell Ligand Density. *Biomacromolecules* **2014**, *15* (9), 3421–3428. https://doi.org/10.1021/bm500969d.

(39) Newman, K.; Clark, K.; Gurumurthy, B.; Pal, P.; Janorkar, A. V. Elastin-Collagen Based Hydrogels as Model Scaffolds to Induce Three-Dimensional Adipocyte Culture from Adipose Derived Stem Cells. *Bioengineering* **2020**, *7* (3), 1–12. https://doi.org/10.3390/bioengineering7030110.

(40) Diáz-Caballero, M.; Navarro, S.; Ventura, S. Functionalized Prion-Inspired Amyloids for Biosensor Applications. *Biomacromolecules* **2021**, *22* (7), 2822–2833. https://doi.org/10.1021/acs.biomac.1c00222.

(41) Li, Y.; Li, K.; Wang, X.; Cui, M.; Ge, P.; Zhang, J.; Qiu, F.; Zhong, C.; Zhong, C. Conformable Self-Assembling Amyloid Protein Coatings with Genetically Programmable Functionality. *Sci. Adv.* **2020**, *6* (21), 1–12. https://doi.org/10.1126/sciadv.aba1425.

(42) Gras, S. L.; Tickler, A. K.; Squires, A. M.; Devlin, G. L.; Horton, M. A.; Dobson, C. M.; MacPhee, C. E. Functionalised Amyloid Fibrils for Roles in Cell Adhesion. *Biomaterials* **2008**, *29* (11), 1553–1562. https://doi.org/10.1016/j.biomaterials.2007.11.028.

(43) Mostaert, A. S.; Higgins, M. J.; Fukuma, T.; Rindi, F.; Jarvis, S. P. Nanoscale Mechanical Characterisation of Amyloid Fibrils Discovered in a Natural Adhesive. *J. Biol. Phys.* **2006**, *32* (5), 393–401. https://doi.org/10.1007/s10867-006-9023-y.

(44) Reches, M.; Gazit, E. Casting Metal Nanowires within Discrete Self-Assembled Peptide Nanotubes. *Science.* **2003**, *300* (5619), 625–627. https://doi.org/10.1126/science.1082387.

(45) Rammensee, S.; Slotta, U.; Scheibel, T.; Bausch, A. R. Assembly Mechanism of Recombinant Spider Silk Proteins. *Proc. Natl. Acad. Sci. U. S. A.* **2008**, *105* (18), 6590–6595. https://doi.org/10.1073/pnas.0709246105.

(46) Papapostolou, D.; Smith, A. M.; Atkins, E. D. T.; Oliver, S. J.; Ryadnov, M. G.; Serpell, L. C.; Woolfson, D. N. Engineering Nanoscale Order into a Designed Protein Fiber. *Proc.*

Natl. Acad. Sci. U. S. A. **2007**, *104* (26), 10853–10858. https://doi.org/10.1073/pnas.0700801104.

(47) Kluge, J. A.; Rabotyagova, O.; Leisk, G. G.; Kaplan, D. L. Spider Silks and Their Applications. *Trends Biotechnol.* **2008**, *26* (5), 244–251. https://doi.org/10.1016/j.tibtech.2008.02.006.

(48) Kiseleva, A. P.; Krivoshapkin, P. V.; Krivoshapkina, E. F. Recent Advances in Development of Functional Spider Silk-Based Hybrid Materials. *Front. Chem.* **2020**, *8* (June), 1–20. https://doi.org/10.3389/fchem.2020.00554.

(49) Malay, A. D.; Suzuki, T.; Katashima, T.; Kono, N.; Arakawa, K.; Numata, K. Spider Silk Self-Assembly via Modular Liquid-Liquid Phase Separation and Nanofibrillation. *Sci. Adv.* **2020**, *6* (45), 1–13. https://doi.org/10.1126/SCIADV.ABB6030.

(50) Nilebäck, L.; Hedin, J.; Widhe, M.; Floderus, L. S.; Krona, A.; Bysell, H.; Hedhammar, M. Self-Assembly of Recombinant Silk as a Strategy for Chemical-Free Formation of Bioactive Coatings: A Real-Time Study. *Biomacromolecules* **2017**, *18* (3), 846–854. https://doi.org/10.1021/acs.biomac.6b01721.

(51) Kiseleva, A. P.; Kiselev, G. O.; Nikolaeva, V. O.; Seisenbaeva, G.; Kessler, V.; Krivoshapkin, P. V.; Krivoshapkina, E. F. Hybrid Spider Silk with Inorganic Nanomaterials. *Nanomaterials* **2020**, *10* (9), 1–16. https://doi.org/10.3390/nano10091853.

(52) Reinke, A. W.; Grant, R. A.; Keating, A. E. A Synthetic Coiled-Coil Interactome Provides Heterospecific Modules for Molecular Engineering. *J. Am. Chem. Soc.* **2010**, *132* (17), 6025–6031. https://doi.org/10.1021/ja907617a.

(53) Thompson, K. E.; Bashor, C. J.; Lim, W. A.; Keating, A. E. Synzip Protein Interaction Toolbox: In Vitro and in Vivo Specifications of Heterospecific Coiled-Coil Interaction Domains. *ACS Synth. Biol.* **2012**, *1* (4), 118–129. https://doi.org/10.1021/sb200015u.

(54) Fletcher, J. M.; Boyle, A. L.; Bruning, M.; Bartlett, Sg. J.; Vincent, T. L.; Zaccai, N. R.; Armstrong, C. T.; Bromley, E. H. C.; Booth, P. J.; Brady, R. L.; Thomson, A. R.; Woolfson, D. N. A Basis Set of de Novo Coiled-Coil Peptide Oligomers for Rational Protein Design and Synthetic Biology. *ACS Synth. Biol.* **2012**, *1* (6), 240–250. https://doi.org/10.1021/sb300028q.

(55) Lupas, A. N.; Bassler, J.; Dunin-Horkawicz, S. *The Structure and Topology of α-Helical Coiled Coils*; 2017; Vol. 82. https://doi.org/10.1007/978-3-319-49674-0_4.

(56) Woolfson, D. N. The Design of Coiled-Coil Structures and Assemblies. *Adv. Protein Chem.* **2005**, *70* (04), 79–112. https://doi.org/10.1016/S0065-3233(05)70004-8.

(57) Utterström, J.; Naeimipour, S.; Selegård, R.; Aili, D. Coiled Coil-Based Therapeutics and Drug Delivery Systems. *Adv. Drug Deliv. Rev.* **2021**, *170*, 26–43. https://doi.org/10.1016/j.addr.2020.12.012.

(58) Burkhard, P.; Ivaninskii, S.; Lustig, A. Improving Coiled-Coil Stability by Optimizing Ionic Interactions. *J. Mol. Biol.* **2002**, *318* (3), 901–910. https://doi.org/10.1016/S0022-2836(02)00114-6.

(59) Gribbon, C.; Channon, K. J.; Zhang, W.; Banwell, E. F.; Bromley, E. H. C.; Chaudhuri, J. B.; Oreffo, R. O. C.; Woolfson, D. N. MagicWand: A Single, Designed Peptide That Assembles to Stable, Ordered α-Helical Fibers. *Biochemistry* **2008**, *47* (39), 10365–10371. https://doi.org/10.1021/bi801072s.

(60) Akey, D. L.; Malashkevich, V. N.; Kim, P. S. Buried Polar Residues in Coiled-Coil Interfaces. *Biochemistry* **2001**, *40* (21), 6352–6360. https://doi.org/10.1021/bi002829w.

(61) Crick, F. H. . The Packing of α-Helices: Simple Coiled-Coils. *Acta Crystallogr.* **1953**, *6* (8), 689–697. https://doi.org/10.1107/s0365110x53001964.

(62) Walshaw, J.; Woolfson, D. N. SOCKET: A Program for Identifying and Analysing Coiled-Coil Motifs within Protein Structures. *J. Mol. Biol.* **2001**, *307* (5), 1427–1450. https://doi.org/10.1006/jmbi.2001.4545.

(63) Lapenta, F.; Aupič, J.; Strmšek, Ž.; Jerala, R. Coiled Coil Protein Origami: From Modular Design Principles towards Biotechnological Applications. *Chem. Soc. Rev.* **2018**, *47* (10), 3530–3542. https://doi.org/10.1039/c7cs00822h.

(64) Mandal, R.; Bedewy, M.; Park, W. M. Coiled-Coil Protein Origami Nanostructure Modeling for Improved Characterization and Prediction. *Mol. Syst. Des. Eng.* **2022**, *7* (7), 725–732. https://doi.org/10.1039/d2me00037g.

(65) Park, W. M. Coiled-Coils: The Molecular Zippers That Self-Assemble Protein Nanostructures. *Int. J. Mol. Sci.* **2020**, *21* (10). https://doi.org/10.3390/ijms21103584.

(66) Fletcher, J. M.; Harniman, R. L.; Barnes, F. R. H.; Boyle, A. L.; Collins, A.; Mantell, J.; Sharp, T. H.; Antognozzi, M.; Booth, P. J.; Linden, N.; Miles, M. J.; Sessions, R. B.; Verkade, P.; Woolfson, D. N. Self-Assembling Cages from Coiled-Coil Peptide Modules Europe PMC Funders Group. *Science.* **2013**, *340* (6132), 595–599. https://doi.org/10.1126/science.1233936.Self-Assembling.

(67) Ross, J. F.; Bridges, A.; Fletcher, J. M.; Shoemark, D.; Alibhai, D.; Bray, H. E. V.; Beesley, J. L.; Dawson, W. M.; Hodgson, L. R.; Mantell, J.; Verkade, P.; Edge, C. M.; Sessions, R. B.; Tew, D.; Woolfson, D. N. Decorating Self-Assembled Peptide Cages with Proteins. *ACS Nano* **2017**, *11* (8), 7901–7914. https://doi.org/10.1021/acsnano.7b02368.

(68) Beesley, J. L.; Baum, H. E.; Hodgson, L. R.; Verkade, P.; Banting, G. S.; Woolfson, D. N. Modifying Self-Assembled Peptide Cages to Control Internalization into Mammalian Cells. *Nano Lett.* **2018**, *18* (9), 5933–5937. https://doi.org/10.1021/acs.nanolett.8b02633.

(69) Yang, J.; Yao, M. H.; Wen, L.; Song, J. T.; Zhang, M. Z.; Zhao, Y. Di; Liu, B. Multifunctional Quantum Dot-Polypeptide Hybrid Nanogel for Targeted Imaging and Drug Delivery. *Nanoscale* **2014**, *6* (19), 11282–11292.

https://doi.org/10.1039/c4nr03058c.

(70) Ernenwein, D.; Ghosh, P.; Rotello, V.; Chmielewski, J. Gold Nanoparticle Self-Assembly Promoted by a Non-Covalent, Charge-Complemented Coiled-Coil Peptide. *J. Mater. Chem.* **2010**, *20* (27), 5608–5611. https://doi.org/10.1039/c0jm01108h.

(71) Quijano-Rubio, A.; Yeh, H. W.; Park, J.; Lee, H.; Langan, R. A.; Boyken, S. E.; Lajoie, M. J.; Cao, L.; Chow, C. M.; Miranda, M. C.; Wi, J.; Hong, H. J.; Stewart, L.; Oh, B. H.; Baker, D. De Novo Design of Modular and Tunable Protein Biosensors. *Nature* **2021**, *591* (7850), 482–487. https://doi.org/10.1038/s41586-021-03258-z.

(72) Lian, M.; Chen, X.; Lu, Y.; Yang, W. Self-Assembled Peptide Hydrogel as a Smart Biointerface for Enzyme-Based Electrochemical Biosensing and Cell Monitoring. *ACS Appl. Mater. Interfaces* **2016**, *8* (38), 25036–25042. https://doi.org/10.1021/acsami.6b05409.

(73) Jeong, W. jin; Choi, S. H.; Lee, H. soo; Lim, Y. beom. A Fluorescent Supramolecular Biosensor for Bacterial Detection via Binding-Induced Changes in Coiled-Coil Molecular Assembly. *Sensors Actuators, B Chem.* **2019**, *290* (March), 93–99. https://doi.org/10.1016/j.snb.2019.03.112.

(74) Muhammad-Tahir, Z.; Alocilja, E. C. A Conductometric Biosensor for Biosecurity. *Biosens. Bioelectron.* **2003**, *18* (5–6), 813–819. https://doi.org/10.1016/S0956-5663(03)00020-4.

(75) Turner, A. P. F. Biosensors: Sense and Sensibility. *Chem. Soc. Rev.* **2013**, *42* (8), 3184–3196. https://doi.org/10.1039/c3cs35528d.

(76) Nangare, S. N.; Patil, P. O. Affinity-Based Nanoarchitectured Biotransducer for Sensitivity Enhancement of Surface Plasmon Resonance Sensors for in Vitro Diagnosis: A Review. *ACS Biomater. Sci. Eng.* **2021**, *7* (1), 2–30. https://doi.org/10.1021/acsbiomaterials.0c01203.

(77) Schwarz, B.; Douglas, T. Development of Virus-like Particles for Diagnostic and Prophylactic Biomedical Applications. *Wiley Interdiscip. Rev. Nanomedicine Nanobiotechnology* **2015**, *7* (5), 722–735. https://doi.org/10.1002/wnan.1336.

(78) Gong, C.; Sun, S.; Zhang, Y.; Sun, L.; Su, Z.; Wu, A.; Wei, G. Hierarchical Nanomaterials: Via Biomolecular Self-Assembly and Bioinspiration for Energy and Environmental Applications. *Nanoscale* **2019**, *11* (10), 4147–4182. https://doi.org/10.1039/c9nr00218a.

(79) Tomadoni, B.; Capello, C.; Valencia, G. A.; Gutiérrez, T. J. Self-Assembled Proteins for Food Applications: A Review. *Trends Food Sci. Technol.* **2020**, *101* (December 2019), 1–16. https://doi.org/10.1016/j.tifs.2020.04.015.

(80) Zeng, R.; Lv, C.; Wang, C.; Zhao, G. Bionanomaterials Based on Protein Self-Assembly: Design and Applications in Biotechnology. *Biotechnol. Adv.* **2021**, *52* (September),

107835. https://doi.org/10.1016/j.biotechadv.2021.107835.

(81) Laitinen, O. H.; Hytönen, V. P.; Nordlund, H. R.; Kulomaa, M. S. Genetically Engineered Avidins and Streptavidins. *Cell. Mol. Life Sci.* **2006**, *63* (24), 2992–3017. https://doi.org/10.1007/s00018-006-6288-z.

(82) Shekhawat, S. S.; Porter, J. R.; Sriprasad, A.; Ghosh, I. An Autoinhibited Coiled-Coil Design Strategy for Split-Protein Protease Sensors. *J. Am. Chem. Soc.* **2009**, *131* (42), 15284–15290. https://doi.org/10.1021/ja9050857.

(83) Song, W. J.; Tezcan, F. A. A Designed Supramolecular Protein Assembly with in Vivo Enzymatic Activity. *Science (80-.).* **2014**, *346* (6216), 1525–1528. https://doi.org/10.1126/science.1259680.

(84) Brodin, J. D.; Carr, J. R.; Sontz, P. A.; Tezcan, F. A. Exceptionally Stable, Redox-Active Supramolecular Protein Assemblies with Emergent Properties. *Proc. Natl. Acad. Sci. U. S. A.* **2014**, *111* (8), 2897–2902. https://doi.org/10.1073/pnas.1319866111.

(85) Salgado, E. N.; Faraone-Mennella, J.; Tezcan, F. A. Controlling Protein-Protein Interactions through Metal Coordination: Assembly of a 16-Helix Bundle Protein. *J. Am. Chem. Soc.* **2007**, *129* (44), 13374–13375. https://doi.org/10.1021/ja075261o.

(86) Sun, H.; Luo, Q.; Hou, C.; Liu, J. Nanostructures Based on Protein Self-Assembly: From Hierarchical Construction to Bioinspired Materials. *Nano Today* **2017**, *14*, 16–41. https://doi.org/10.1016/j.nantod.2017.04.006.

(87) Ren, H.; Zhu, S.; Zheng, G. Nanoreactor Design Based on Self-Assembling Protein Nanocages. *Int. J. Mol. Sci.* **2019**, *20* (3), 25–27. https://doi.org/10.3390/ijms20030592.

(88) Li, H.; Zheng, G.; Zhu, S. Construction of an Organelle-like Nanodevice via Supramolecular Self-Assembly for Robust Biocatalysts. *Microb. Cell Fact.* **2018**, *17* (1), 1–11. https://doi.org/10.1186/s12934-018-0873-3.

(89) Zhang, Y.; Ardejani, M. S. *Protein Cages*; Orner, B. P., Ed.; Humana Press: London, UK, 2015.

(90) Heddle, J. G.; Chakraborti, S.; Iwasaki, K. Natural and Artificial Protein Cages: Design, Structure and Therapeutic Applications. *Curr. Opin. Struct. Biol.* **2017**, *43*, 148–155. https://doi.org/10.1016/j.sbi.2017.03.007.

(91) Herrera Estrada, L. P.; Champion, J. A. Protein Nanoparticles for Therapeutic Protein Delivery. *Biomater. Sci.* **2015**, *3* (6), 787–799. https://doi.org/10.1039/c5bm00052a.

(92) McDaniel, J. R.; Callahan, D. J.; Chilkoti, A. Drug Delivery to Solid Tumors by Elastin-like Polypeptides. *Adv. Drug Deliv. Rev.* **2010**, *62* (15), 1456–1467. https://doi.org/10.1016/j.addr.2010.05.004.

(93) Andrew MacKay, J.; Chen, M.; McDaniel, J. R.; Liu, W.; Simnick, A. J.; Chilkoti, A.

Self-Assembling Chimeric Polypeptide-Doxorubicin Conjugate Nanoparticles That Abolish Tumours after a Single Injection. *Nat. Mater.* **2009**, *8* (12), 993–999. https://doi.org/10.1038/nmat2569.

(94) Rodríguez-Cabello, J. C.; Arias, F. J.; Rodrigo, M. A.; Girotti, A. Elastin-like Polypeptides in Drug Delivery. *Adv. Drug Deliv. Rev.* **2016**, *97*, 85–100. https://doi.org/10.1016/j.addr.2015.12.007.

(95) Kim, H.; Ju, J.; Lee, H. N.; Chun, H.; Seong, J. Genetically Encoded Biosensors Based on Fluorescent Proteins. *Sensors (Switzerland)* **2021**, *21* (3), 1–18. https://doi.org/10.3390/s21030795.

(96) Lyons, A. C.; Mehta, S.; Zhang, J. Fluorescent Biosensors Illuminate the Spatial Regulation of Cell Signaling across Scales. *Biochem. J.* **2023**, *480* (20), 1693–1717. https://doi.org/10.1042/BCJ20220223.

(97) Valenzuela-García, L. I.; Alarcón-Herrera, M. T.; Ayala-García, V. M.; Barraza-Salas, M.; Salas-Pacheco, J. M.; Díaz-Valles, J. F.; Pedraza-Reyes, M. Design of a Whole-Cell Biosensor Based on Bacillus Subtilis Spores and the Green Fluorescent Protein To Monitor Arsenic. *Microbiol. Spectr.* **2023**, *11* (4), 1–11. https://doi.org/10.1128/spectrum.00432-23.

(98) Park, S.; Cho, E.; Chueng, S. T. D.; Yoon, J. S.; Lee, T.; Lee, J. H. Aptameric Fluorescent Biosensors for Liver Cancer Diagnosis. *Biosensors* **2023**, *13* (6), 1–17. https://doi.org/10.3390/bios13060617.

(99) Pavoor, T. V.; Yong, K. C.; Shusta, E. V. Development of GFP-Based Biosensors Possessing the Binding Properties of Antibodies. *Proc. Natl. Acad. Sci. U. S. A.* **2009**, *106* (29), 11895–11900. https://doi.org/10.1073/pnas.0902828106.

(100) VanEngelenburg, S. B.; Palmer, A. E. Fluorescent Biosensors of Protein Function. *Curr. Opin. Chem. Biol.* **2008**, *12* (1), 60–65. https://doi.org/10.1016/j.cbpa.2008.01.020.

(101) Fatima, U.; Ameen, F.; Soleja, N.; Khan, P.; Almansob, A.; Ahmad, A. A Fluorescence Resonance Energy Transfer-Based Analytical Tool for Nitrate Quantification in Living Cells. *ACS Omega* **2020**, *5* (46), 30306–30314. https://doi.org/10.1021/acsomega.0c04868.

(102) Huang, W.; Wu, T.; Xie, C.; Rayner, C. K.; Priest, C.; Ebendorff-Heidepriem, H.; Zhao, J. Sensing Intra- and Extra-Cellular Ca^{2+} in the Islet of Langerhans. *Adv. Funct. Mater.* **2022**, *32* (3), 1–24. https://doi.org/10.1002/adfm.202106020.

(103) Yamada, Y.; Namba, K.; Fujii, T. Cardiac Muscle Thin Filament Structures Reveal Calcium Regulatory Mechanism. *Nat. Commun.* **2020**, *11* (1), 1–3. https://doi.org/10.1038/s41467-019-14008-1.

(104) Xu, H. T.; Yuan, X. B.; Guan, C. B.; Duan, S.; Wu, C. P.; Feng, L. Calcium Signaling in Chemorepellant Slit2-Dependent Regulation of Neuronal Migration. *Proc. Natl. Acad. Sci.*

U. S. A. **2004**, *101* (12), 4296–4301. https://doi.org/10.1073/pnas.0303893101.

(105) Ozbakir, H. F.; Miller, A. D. C.; Fishman, K. B.; Martins, A. F.; Kippin, T. E.; Mukherjee, A. A Protein-Based Biosensor for Detecting Calcium by Magnetic Resonance Imaging. *ACS Sensors* **2021**, *6* (9), 3163–3169. https://doi.org/10.1021/acssensors.1c01085.

(106) Kalko, E. K. V; Dukas, R.; Ratcliffe, J. M.; Teeling, E. C.; Haven, N.; Fattu, J. M.; Bates, M. E.; Simmons, J. a; Riquimaroux, H.; Surlykke, A.; Bouffard, F. H.; Lee, D. N.; Dear, S. P.; Horiuchi, T. K.; Krishnaprasad, P. S.; Moss, C. F.; Schuller, G.; Brudzynski, S. M.; Syme, D. a; Hollingworth, S.; Lindstedt, S. L.; Baylor, S. M.; Mead, a F.; Rome, L. C.; Goller, F.; Spierts, I. L. Y.; Leeuwen, J. L. Van; Schachat, F.; Rossmanith, G. H.; Hoh, J. F. Y.; Kelley, D. B.; Vater, M. a; Zhao, Y.; Kalko, E. K. V; Dukas, R.; Ratcliffe, J. M.; Teeling, E. C.; Haven, N.; Fattu, J. M.; Bates, M. E.; Simmons, J. a; Riquimaroux, H.; Surlykke, A.; Bouffard, F. H.; Lee, D. N.; Dear, S. P.; Horiuchi, T. K.; Krishnaprasad, P. S.; Moss, C. F.; Schuller, G.; Brudzynski, S. M.; Syme, D. a; Hollingworth, S.; Lindstedt, S. L.; Baylor, S. M.; Mead, a F.; Rome, L. C.; Goller, F.; Spierts, I. L. Y.; Leeuwen, J. L. Van; Schachat, F.; Rossmanith, G. H.; Hoh, J. F. Y.; Kelley, D. B.; Vater, M. a. An Expanded Palette of Genetically Encoded Ca^{2+} Indicators. *Science.* **2011**, *333* (September), 1888–1891.

(107) Zhao, Y.; Araki, S.; Wu, J.; Teramoto, T.; Chang, Y.-F.; Nakano, M.; Abdelfattah, A. S.; Fujiwara, M.; Ishihara, T.; Nagai, T.; Campbell, R. E. An Expanded Palette of Genetically Encoded Ca^{2+} Indicators. *Science.* **2011**, *333* (September), 1888–1891.

(108) Zhang, Y.; Rózsa, M.; Liang, Y.; Bushey, D.; Wei, Z.; Zheng, J.; Reep, D.; Broussard, G. J.; Tsang, A.; Tsegaye, G.; Narayan, S.; Obara, C. J.; Lim, J.-X.; Patel, R.; Zhang, R.; Ahrens, M. B.; Turner, G. C.; Wang, S. S. H.; Korff, W. L.; Schreiter, E. R.; Svoboda, K.; Hasseman, J. P.; Kolb, I.; Looger, L. L. Fast and Sensitive GCaMP Calcium Indicators for Imaging Neural Populations. *Nature* **2023**, *615* (7954), 884–891. https://doi.org/10.1038/s41586-023-05828-9.

(109) Junichi Nakai; Masamichi Ohkura; Keiji Imoto. A High Signal-to-Noise Ca^{2+} Probe Composed of a Single Green Fluorescent Protein. *Nat. Biotechnol.* **2001**, *19*, 137–141.

(110) Barnett, L. M.; Hughes, T. E.; Drobizhev, M. Deciphering the Molecular Mechanism Responsible for GCaMP6m's Ca^{2+}-Dependent Change in Fluorescence. *PLoS One* **2017**, *12* (2), 1–24. https://doi.org/10.1371/journal.pone.0170934.

(111) Molina, R. S.; Qian, Y.; Wu, J.; Shen, Y.; Campbell, R. E.; Drobizhev, M.; Hughes, T. E. Understanding the Fluorescence Change in Red Genetically Encoded Calcium Ion Indicators. *Biophys. J.* **2019**, *116* (10), 1873–1886. https://doi.org/10.1016/j.bpj.2019.04.007.

(112) Wu, J.; Liu, L.; Matsuda, T.; Zhao, Y.; Rebane, A.; Drobizhev, M.; Chang, Y. F.; Araki, S.; Arai, Y.; March, K.; Hughes, T. E.; Sagou, K.; Miyata, T.; Nagai, T.; Li, W. H.; Campbell, R. E. Improved Orange and Red Ca^{2+} Indicators and Photophysical Considerations for Optogenetic Applications. *ACS Chem. Neurosci.* **2013**, *4* (6), 963–972. https://doi.org/10.1021/cn400012b.

(113) Suzuki, J.; Kanemaru, K.; Ishii, K.; Ohkura, M.; Okubo, Y.; Iino, M. Imaging Intraorganellar Ca^{2+} at Subcellular Resolution Using CEPIA. *Nat. Commun.* **2014**, *5* (May), 1–13. https://doi.org/10.1038/ncomms5153.

(114) Gasterstädt, I.; Jack, A.; Stahlhut, T.; Rennau, L. M.; Gonda, S.; Wahle, P. Genetically Encoded Calcium Indicators Can Impair Dendrite Growth of Cortical Neurons. *Front. Cell. Neurosci.* **2020**, *14* (October), 1–18. https://doi.org/10.3389/fncel.2020.570596.

(115) Tian, L.; Andrew Hires, S.; Looger, L. L. Imaging Neuronal Activity with Genetically Encoded Calcium Indicators. *Cold Spring Harb. Protoc.* **2012**, *7* (6), 647–656. https://doi.org/10.1101/pdb.top069609.

(116) Shimomura, O.; Johnson, F. H. Peroxidized Coelenterazine, the Active Group in the Photoprotein Aequorin. *Proc. Natl. Acad. Sci. U. S. A.* **1978**, *75* (6), 2611–2615. https://doi.org/10.1073/pnas.75.6.2611.

(117) Shimomura, O.; Johnson, F. H.; Saiga, Y. Extraction, Purification and Properties of Aequorin, a Bioluminescent. *J. Cell. Comp. Physiol.* **1962**, *59* (165), 223–239. https://doi.org/10.1002/jcp.1030590302.

(118) Ebrahimi, M.; Mohseni, A.; Khalifeh, K.; Ranjbar, B.; Sajedi, R. H. Evolutionary Conservation of EF-Hand II Loop in Aequorin: Priority of Intensity to Decay Rate in Bioluminescence Emission. *Arch. Biochem. Biophys.* **2017**, *634*, 29–37. https://doi.org/10.1016/j.abb.2017.09.018.

(119) Shimomura, O.; Johnson, F. H. Calcium Binding, Quantum Yield, and Emitting Molecule in Aequorin Bioluminescence. *Nature* **1970**, *227*, 1356–1357.

(120) Rodriguez-Garcia, A.; Rojo-Ruiz, J.; Navas-Navarro, P.; Aulestia, F. J.; Gallego-Sandin, S.; Garcia-Sancho, J.; Alonso, M. T. GAP, an Aequorin-Based Fluorescent Indicator for Imaging Ca^{2+} in Organelles. *Proc. Natl. Acad. Sci. U. S. A.* **2014**, *111* (7), 2584–2589. https://doi.org/10.1073/pnas.1316539111.

(121) Baubet, V.; Le Mouellic, H.; Campbell, A. K.; Lucas-Meunier, E.; Fossier, P.; Brûlet, P. Chimeric Green Fluorescent Protein-Aequorin as Bioluminescent Ca^{2+} Reporters at the Single-Cell Level. *Proc. Natl. Acad. Sci. U. S. A.* **2000**, *97* (13), 7260–7265. https://doi.org/10.1073/pnas.97.13.7260.

(122) López-Arredondo, D. L.; Leyva-González, M. A.; Alatorre-Cobos, F.; Herrera-Estrella, L. Biotechnology of Nutrient Uptake and Assimilation in Plants. *Int. J. Dev. Biol.* **2013**, *57* (6–8), 595–610. https://doi.org/10.1387/ijdb.130268lh.

(123) Dong, H. P.; Huang, K. X.; Wang, H. L.; Lu, S. H.; Cen, J. Y.; Dong, Y. L. Understanding Strategy of Nitrate and Urea Assimilation in a Chinese Strain of Aureococcus Anophagefferens through RNA-Seq Analysis. *PLoS One* **2014**, *9* (10). https://doi.org/10.1371/journal.pone.0111069.

(124) Van Kessel, M. A. H. J.; Speth, D. R.; Albertsen, M.; Nielsen, P. H.; Op Den Camp, H. J.

M.; Kartal, B.; Jetten, M. S. M.; Lücker, S. Complete Nitrification by a Single Microorganism. *Nature* **2015**, *528* (7583), 555–559. https://doi.org/10.1038/nature16459.

(125) Wang, Y. Y.; Cheng, Y. H.; Chen, K. E.; Tsay, Y. F. Nitrate Transport, Signaling, and Use Efficiency. *Annu. Rev. Plant Biol.* **2018**, *69*, 85–122. https://doi.org/10.1146/annurev-arplant-042817-040056.

(126) Sparacino-Watkins, C.; Stolz, J. F.; Basu, P. Nitrate and Periplasmic Nitrate Reductases. *Chem. Soc. Rev.* **2014**, *43* (2), 676–706. https://doi.org/10.1039/c3cs60249d.Nitrate.

(127) Ignarro, L. J.; Fukuto, J. M.; Griscavage, J. M.; Rogers, N. E.; Byrns, R. E. Oxidation of Nitric Oxide in Aqueous Solution to Nitrite but Not Nitrate: Comparison with Enzymatically Formed Nitric Oxide from L-Arginine. *Proc. Natl. Acad. Sci. U. S. A.* **1993**, *90* (17), 8103–8107. https://doi.org/10.1073/pnas.90.17.8103.

(128) Ma, L.; Hu, L.; Feng, X.; Wang, S. Nitrate and Nitrite in Health and Disease. *Aging Dis.* **2018**, *9* (5), 938–945. https://doi.org/10.14336/AD.2017.1207.

(129) Chen, Y. N.; Cartwright, H. N.; Ho, C. H. In Vivo Visualization of Nitrate Dynamics Using a Genetically Encoded Fluorescent Biosensor. *Sci. Adv.* **2022**, *8* (42), 1–10. https://doi.org/10.1126/sciadv.abq4915.

(130) Hidaka, M.; Gotoh, A.; Shimizu, T.; Minamisawa, K.; Imamura, H.; Uchida, T. Visualization of NO_3^-/NO_2^- Dynamics in Living Cells by Fluorescence Resonance Energy Transfer (FRET) Imaging Employing a Rhizobial Two-Component Regulatory System. *J. Biol. Chem.* **2016**, *291* (5), 2260–2269. https://doi.org/10.1074/jbc.M115.687632.

(131) Clegg, R. M. *Förster Resonance Energy Transfer-FRET What Is It, Why Do It, and How It's Done*, 1st ed.; Elesvier B.V., 2009; Vol. 33. https://doi.org/10.1016/S0075-7535(08)00001-6.

(132) Bajar, B. T.; Wang, E. S.; Zhang, S.; Lin, M. Z.; Chu, J. A Guide to Fluorescent Protein FRET Pairs. *Sensors (Switzerland)* **2016**, *16* (9), 1–24. https://doi.org/10.3390/s16091488.

(133) Koropatkin, N. M.; Pakrasi, H. B.; Smith, T. J. Atomic Structure of a Nitrate-Binding Protein Crucial for Photosynthetic Productivity. *Proc. Natl. Acad. Sci. U. S. A.* **2006**, *103* (26), 9820–9825. https://doi.org/10.1073/pnas.0602517103.

(134) Purewal, S. S.; Kaur, A.; Bangar, S. P.; Singh, P.; Singh, H. Protein-Based Films and Coatings: An Innovative Approach. *Coatings* **2024**, *14* (1), 1–24. https://doi.org/10.3390/coatings14010032.

(135) Mihalca, V.; Kerezsi, A. D.; Weber, A.; Gruber-traub, C.; Schmucker, J.; Vodnar, D. C.; Dulf, F. V.; Socaci, S. A.; Fărcaș, A.; Mureșan, C. I.; Suharoschi, R.; Pop, O. L. Protein-based Films and Coatings for Food Industry Applications. *Polymers (Basel).* **2021**, *13* (5), 1–24. https://doi.org/10.3390/polym13050769.

(136) Aigner, T. B.; DeSimone, E.; Scheibel, T. Biomedical Applications of Recombinant Silk-

Based Materials. *Adv. Mater.* **2018**, *30* (19), 1–28. https://doi.org/10.1002/adma.201704636.

(137) Valo, H. K.; Laaksonen, H.; Peltonen, L. J.; Linder, M. B.; Hirvonen, J. T. Multifunctional Hydrophobin : Toward Nanoparticles. *ACS Nano* **2010**, *4* (Xx), 1750–1758.

(138) Li, L.; Yang, Y.; Wang, L.; Xu, F.; Li, Y.; He, X. The Effects of Serum Albumin Pre-Adsorption of Nanoparticles on Protein Corona and Membrane Interaction: A Molecular Simulation Study. *J. Mol. Biol.* **2023**, *435* (1), 167771. https://doi.org/10.1016/j.jmb.2022.167771.

(139) He, X.; Li, L.; Yang, Y.; Dong, Z.; Wang, L.; Qu, Z.; Xu, F. Tailoring Patchy Nanoparticle Design to Modulate Serum Albumin Adsorption and Membrane Interaction. *Soft Matter* **2021**, *17* (8), 2071–2080. https://doi.org/10.1039/d0sm01889a.

(140) Liu, Y.; Wu, G.; De Groot, K. Biomimetic Coatings for Bone Tissue Engineering of Critical-Sized Defects. *J. R. Soc. Interface* **2010**, *7*. https://doi.org/10.1098/rsif.2010.0115.focus.

(141) Jo, Y. K.; Kim, H. J.; Jeong, Y.; Joo, K. Il; Cha, H. J. Biomimetic Surface Engineering of Biomaterials by Using Recombinant Mussel Adhesive Proteins. *Adv. Mater. Interfaces* **2018**, *5* (9), 1–13. https://doi.org/10.1002/admi.201800068.

(142) Xuan, H.; Tang, X.; Zhu, Y.; Ling, J.; Yang, Y. Freestanding Hyaluronic Acid/Silk-Based Self-Healing Coating toward Tissue Repair with Antibacterial Surface. *ACS Appl. Bio Mater.* **2020**, *3* (3), 1628–1635. https://doi.org/10.1021/acsabm.9b01196.

(143) Sahoo, J.; Sharma, R.; Pachauri, V.; Gandhi, S. Biomimetic/Bioderived Nanoengineered Interfaces for Biosensor Applications: A Review. *ACS Appl. Nano Mater.* **2024**, *7* (17), 19854–19875. https://doi.org/10.1021/acsanm.4c04554.

(144) Paloni, J. M.; Olsen, B. D. Polymer Domains Control Diffusion in Protein-Polymer Conjugate Biosensors. *ACS Appl. Polym. Mater.* **2020**, *2* (11), 4481–4492. https://doi.org/10.1021/acsapm.0c00534.

(145) Grel, H.; Ratajczak, K.; Jakiela, S.; Stobiecka, M. Gated Resonance Energy Transfer (Gret) Controlled by Programmed Death Protein Ligand 1. *Nanomaterials* **2020**, *10* (8), 1–12. https://doi.org/10.3390/nano10081592.

(146) Lefevre, M.; Flammang, P.; Aranko, A. S.; Linder, M. B.; Scheibel, T.; Humenik, M.; Leclercq, M.; Surin, M.; Tafforeau, L.; Wattiez, R.; Leclère, P.; Hennebert, E. Sea Star-Inspired Recombinant Adhesive Proteins Self-Assemble and Adsorb on Surfaces in Aqueous Environments to Form Cytocompatible Coatings. *Acta Biomater.* **2020**, *112*, 62–74. https://doi.org/10.1016/j.actbio.2020.05.036.

(147) Tian, J.; Liu, Y.; Miao, S.; Yang, Q.; Hu, X.; Han, Q.; Xue, L.; Yang, P. Amyloid-like Protein Aggregates Combining Antifouling with Antibacterial Activity. *Biomater. Sci.* **2020**, *8* (24), 6903–6911. https://doi.org/10.1039/d0bm00760a.

(148) Sabaté del Río, J.; Henry, O. Y. F.; Jolly, P.; Ingber, D. E. An Antifouling Coating That Enables Affinity-Based Electrochemical Biosensing in Complex Biological Fluids. *Nat. Nanotechnol.* **2019**, *14* (12), 1143–1149. https://doi.org/10.1038/s41565-019-0566-z.

(149) Novick, S. J.; Dordick, J. S. Protein-Containing Hydrophobic Coatings and Films. *Biomaterials* **2002**, *23* (2), 441–448. https://doi.org/10.1016/S0142-9612(01)00123-5.

(150) Xu, X.; Xu, Z. K.; Yang, X. F.; He, Y. H.; Lin, R. Construction and Characterization of a Pure Protein Hydrogel for Drug Delivery Application. *Int. J. Biol. Macromol.* **2017**, *95*, 294–298. https://doi.org/10.1016/j.ijbiomac.2016.11.028.

(151) Kimura, Y.; Tabata, Y. Controlled Release of Stromal-Cell-Derived Factor-1 from Gelatin Hydrogels Enhances Angiogenesis. *J. Biomater. Sci. Polym. Ed.* **2010**, *21* (1), 37–51. https://doi.org/10.1163/156856209X410193.

(152) Nguyen, P. Q.; Botyanszki, Z.; Tay, P. K. R.; Joshi, N. S. Programmable Biofilm-Based Materials from Engineered Curli Nanofibres. *Nat. Commun.* **2014**, *5*, 1–10. https://doi.org/10.1038/ncomms5945.

(153) Song, R.; Wu, X.; Xue, B.; Yang, Y.; Huang, W.; Zeng, G.; Wang, J.; Li, W.; Cao, Y.; Wang, W.; Lu, J.; Dong, H. Principles Governing Catalytic Activity of Self-Assembled Short Peptides. *J. Am. Chem. Soc.* **2019**, *141* (1), 223–231. https://doi.org/10.1021/jacs.8b08893.

(154) Botyanszki, Z.; Tay, P. K. R.; Nguyen, P. Q.; Nussbaumer, M. G.; Joshi, N. S. Engineered Catalytic Biofilms: Site-Specific Enzyme Immobilization onto E. Coli Curli Nanofibers. *Biotechnol. Bioeng.* **2015**, *112* (10), 2016–2024. https://doi.org/10.1002/bit.25638.

(155) Nussbaumer, M. G.; Nguyen, P. Q.; Tay, P. K. R.; Naydich, A.; Hysi, E.; Botyanszki, Z.; Joshi, N. S. Bootstrapped Biocatalysis: Biofilm-Derived Materials as Reversibly Functionalizable Multienzyme Surfaces. *ChemCatChem* **2017**, *9* (23), 4328–4333. https://doi.org/10.1002/cctc.201701221.

(156) Gastaldi, E.; Chalier, P.; Guillemin, A.; Gontard, N. Microstructure of Protein-Coated Paper as Affected by Physico-Chemical Properties of Coating Solutions. *Colloids Surfaces A Physicochem. Eng. Asp.* **2007**, *301* (1–3), 301–310. https://doi.org/10.1016/j.colsurfa.2006.12.079.

(157) Ye, A.; Zhu, Z.; Ji, Z.; He, X.; He, Y.; Fu, X.; Yang, W.; Wang, Y. Electrochemical Active Micro-Protein Coating by Self-Assembling 2D-Microfluidics for Stabilizing Lithium Metal Anode. *Adv. Funct. Mater.* **2024**, *34* (6), 1–13. https://doi.org/10.1002/adfm.202310593.

(158) Gao, A.; Wu, Q.; Wang, D.; Ha, Y.; Chen, Z.; Yang, P. A Superhydrophobic Surface Templated by Protein Self-Assembly and Emerging Application toward Protein Crystallization. *Adv. Mater.* **2016**, *28* (3), 579–587. https://doi.org/10.1002/adma.201504769.

(159) Huang, A.; Qin, G.; Olsen, B. D. Highly Active Biocatalytic Coatings from Protein-Polymer Diblock Copolymers. *ACS Appl. Mater. Interfaces* **2015**, *7* (27), 14660–14669. https://doi.org/10.1021/acsami.5b01884.

(160) Masigol, M.; Fattahi, N.; Barua, N.; Lokitz, B. S.; Retterer, S. T.; Platt, T. G.; Hansen, R. R. Identification of Critical Surface Parameters Driving Lectin-Mediated Capture of Bacteria from Solution. *Biomacromolecules* **2019**, *20* (7), 2852–2863. https://doi.org/10.1021/acs.biomac.9b00609.

(161) Berckman, E. A.; Hartzell, E. J.; Mitkas, A. A.; Sun, Q.; Chen, W. Biological Assembly of Modular Protein Building Blocks as Sensing, Delivery, and Therapeutic Agents. *Annu. Rev. Chem. Biomol. Eng.* **2020**, *11*, 35–62. https://doi.org/10.1146/annurev-chembioeng-101519-121526.

(162) Dash, B. C.; Mahor, S.; Carroll, O.; Mathew, A.; Wang, W.; Woodhouse, K. A.; Pandit, A. Tunable Elastin-like Polypeptide Hollow Sphere as a High Payload and Controlled Delivery Gene Depot. *J. Control. Release* **2011**, *152* (3), 382–392. https://doi.org/10.1016/j.jconrel.2011.03.006.

(163) Srokowski, E. M.; Woodhouse, K. A. Surface and Adsorption Characteristics of Three Elastin-like Polypeptide Coatings with Varying Sequence Lengths. *J. Mater. Sci. Mater. Med.* **2013**, *24* (1), 71–84. https://doi.org/10.1007/s10856-012-4772-6.

(164) Atefyekta, S.; Pihl, M.; Lindsay, C.; Heilshorn, S. C.; Andersson, M. Antibiofilm Elastin-like Polypeptide Coatings: Functionality, Stability, and Selectivity. *Acta Biomater.* **2019**, *83*, 245–256. https://doi.org/10.1016/j.actbio.2018.10.039.

(165) Roberts, S.; Dzuricky, M.; Chilkoti, A. Elastin-like Polypeptides as Models of Intrinsically Disordered Proteins. *FEBS Lett.* **2015**, *589* (19), 2477–2486. https://doi.org/10.1016/j.febslet.2015.08.029.

(166) Moirangthem, M.; Arts, R.; Merkx, M.; Schenning, A. P. H. J. An Optical Sensor Based on a Photonic Polymer Film to Detect Calcium in Serum. *Adv. Funct. Mater.* **2016**, *26* (8), 1154–1160. https://doi.org/10.1002/adfm.201504534.

(167) Ding, Y.; Ling, J.; Qiao, Y.; Li, Z.; Sun, Z.; Cai, J.; Guo, Y.; Wang, H. A High-Throughput Fluorimetric Microarray with Enhanced Fluorescence and Suppressed "Coffee-Ring" Effects for the Detection of Calcium Ions in Blood. *Sci. Rep.* **2016**, *6* (December), 1–9. https://doi.org/10.1038/srep38602.

(168) Kim, S.; Park, J. W.; Kim, D.; Kim, D.; Lee, I.; Jon, S. Bioinspired Colorimetric Detection of Calcium(II) Ions in Serum Using Calsequestrin-Functionalized Gold Nanoparticles. *Angew. Chemie* **2009**, *121* (23), 4202–4205. https://doi.org/10.1002/ange.200900071.

(169) Kim, S.; Kim, J.; Lee, N. H.; Jang, H. H.; Han, M. S. A Colorimetric Selective Sensing Probe for Calcium Ions with Tunable Dynamic Ranges Using Cytidine Triphosphate Stabilized Gold Nanoparticles. *Chem. Commun.* **2011**, *47* (37), 10299–10301. https://doi.org/10.1039/c1cc13489b.

(170) Golynskiy, M. V.; Gunderson, W. A.; Hendrich, M. P.; Cohen, S. M. Metal Binding Studies and EPR Spectroscopy of the Manganese Transport Regulator MntR. *Biochemistry* **2006**, *45* (51), 15359–15372. https://doi.org/10.1021/bi0607406.

(171) De Acha, N.; Elosúa, C.; Corres, J. M.; Arregui, F. J. Fluorescent Sensors for the Detection of Heavy Metal Ions in Aqueous Media. *Sensors (Switzerland)* **2019**, *19* (3). https://doi.org/10.3390/s19030599.

(172) Huang, W.; Wu, T.; Shallan, A.; Kostecki, R.; Rayner, C. K.; Priest, C.; Ebendorff-Heidepriem, H.; Zhao, J. A Multiplexed Microfluidic Platform toward Interrogating Endocrine Function: Simultaneous Sensing of Extracellular Ca^{2+} and Hormone. *ACS Sensors* **2020**, *5* (2), 490–499. https://doi.org/10.1021/acssensors.9b02308.

(173) Hove-Madsen, L.; Baudet, S.; Bers, D. M. *Making and Using Calcium-Selective Mini- and Microelectrodes*; Elsevier Inc., 2010; Vol. 99. https://doi.org/10.1016/B978-0-12-374841-6.00003-7.

(174) Baudet, S.; Hove-Madsen, L.; Bers, D. M. How to Make and Use Calcium-Specific Mini- and Microelectrodes. *Methods Cell Biol.* **1994**, *40* (C), 93–113. https://doi.org/10.1016/S0091-679X(08)61111-5.

(175) Felle, H. Ca^{2+} -Selective Microelectrodes and Their Application to Plant Cells and Tissues . *Plant Physiol.* **1989**, *91* (4), 1239–1242. https://doi.org/10.1104/pp.91.4.1239.

(176) Moll, J. R. Designed Heterodimerizing Leucine Zippers with a Ranger of PIs and Stabilities up to 10-15 M. *Protein Sci.* **2001**, *10* (3), 649–655. https://doi.org/10.1110/ps.39401.

(177) Park, W. M.; Champion, J. A. Two-Step Protein Self-Assembly in the Extracellular Matrix. *Angew. Chemie - Int. Ed.* **2013**, *52* (31), 8098–8101. https://doi.org/10.1002/anie.201302331.

(178) Park, W. M.; Champion, J. A. Thermally Triggered Self-Assembly of Folded Proteins into Vesicles. *J. Am. Chem. Soc.* **2014**, *136* (52), 17906–17909. https://doi.org/10.1021/ja5090157.

(179) Tan, J. Y.; Li, Y.; Chamani, F.; Tharzeen, A.; Prakash, P.; Natarajan, B.; Sheth, R. A.; Park, W. M.; Kim, A.; Yoon, D.; Kim, J. Experimental Validation of Diffraction Lithography for Fabrication of Solid Microneedles. *Materials (Basel).* **2022**, *15* (24). https://doi.org/10.3390/ma15248934.

(180) Jang, Y.; Hsieh, M. C.; Dautel, D.; Guo, S.; Grover, M. A.; Champion, J. A. Understanding the Coacervate-to-Vesicle Transition of Globular Fusion Proteins to Engineer Protein Vesicle Size and Membrane Heterogeneity. *Biomacromolecules* **2019**, *20* (9), 3494–3503. https://doi.org/10.1021/acs.biomac.9b00773.

(181) Dautel, D. R.; Heller, W. T.; Champion, J. A. Protein Vesicles with PH-Responsive Disassembly. *Biomacromolecules* **2022**, *23* (9), 3678–3687.

https://doi.org/10.1021/acs.biomac.2c00562.

(182) Dautel, D. R.; Champion, J. A. Protein Vesicles Self-Assembled from Functional Globular Proteins with Different Charge and Size. *Biomacromolecules* **2021**, *22* (1), 116–125. https://doi.org/10.1021/acs.biomac.0c00671.

(183) Dautel, D. R.; Champion, J. A. Self-Assembly of Functional Protein Nanosheets from Thermoresponsive Bolaamphiphiles. *Biomacromolecules* **2022**, *23* (9), 3612–3620. https://doi.org/10.1021/acs.biomac.2c00525.

(184) Urry, D. W.; Trapane, T. L.; Prasad, K. U. Phase-structure Transitions of the Elastin Polypentapeptide–Water System within the Framework of Composition–Temperature Studies. *Biopolymers* **1985**, *24* (12), 2345–2356. https://doi.org/10.1002/bip.360241212.

(185) Cirulis, J. T.; Keeley, F. W. Kinetics and Morphology of Self-Assembly of an Elastin-like Polypeptide Based on the Alternating Domain Arrangement of Human Tropoelastin. *Biochemistry* **2010**, *49* (27), 5726–5733. https://doi.org/10.1021/bi100468v.

(186) Roberts, E. K.; Wong, K. M.; Lee, E. J.; Le, M. M.; Patel, D. M.; Paravastu, A. K. Post-Assembly α-Helix to β-Sheet Structural Transformation within SAF-P1/P2a Peptide Nanofibers. *Soft Matter* **2018**, *14* (44), 8986–8996. https://doi.org/10.1039/c8sm01754a.

(187) Cobb, J. S.; Zai-Rose, V.; Correia, J. J.; Janorkar, A. V. FT-IR Spectroscopic Analysis of the Secondary Structures Present during the Desiccation Induced Aggregation of Elastin-Like Polypeptide on Silica. *ACS Omega* **2020**, *5* (14), 8403–8413. https://doi.org/10.1021/acsomega.0c00271.

(188) Yeu-Chun, Kim; Jung-Hwan, P. M. R. P. Microneedles for Drug and Vaccine Delivery. *Adv. Drug Deliv. Rev.* **2012**, *64* (14), 1547–1568. https://doi.org/10.1016/j.addr.2012.04.005.Microneedles.

(189) Chen, J.; Ren, H.; Zhou, P.; Zheng, S.; Du, B.; Liu, X.; Xiao, F. Microneedle-Mediated Drug Delivery for Cutaneous Diseases. **2022**, No. October, 1–16. https://doi.org/10.3389/fbioe.2022.1032041.

(190) Dugam, S.; Tade, R.; Dhole, R.; Nangare, S. Emerging Era of Microneedle Array for Pharmaceutical and Biomedical Applications : Recent Advances and Toxicological Perspectives. **2021**, *1*, 1–26.

(191) Mcgrath, M. G.; Vrdoljak, A.; Mahony, C. O.; Oliveira, J. C.; Moore, A. C.; Crean, A. M. Determination of Parameters for Successful Spray Coating of Silicon Microneedle Arrays. *Int. J. Pharm.* **2011**, *415* (1–2), 140–149. https://doi.org/10.1016/j.ijpharm.2011.05.064.

(192) Chen, Y.; Chen, B. Z.; Wang, Q. L.; Jin, X.; Guo, X. D. Fabrication of Coated Polymer Microneedles for Transdermal Drug Delivery. *J. Control. Release* **2017**, *265* (March), 14–21. https://doi.org/10.1016/j.jconrel.2017.03.383.

(193) Chen, T.; Wardill, T. J.; Sun, Y.; Pulver, S. R.; Renninger, S. L.; Baohan, A.; Schreiter, E.

R.; Kerr, R. A.; Orger, M. B.; Jayaraman, V.; Looger, L. L.; Svoboda, K.; Kim, D. S. Ultra-Sensitive Fluorescent Proteins for Imaging Neuronal Activity. *Nature.* **2013**, *499* (7458), 295–300.

(194) Hofer, A. M.; Brown, E. M. Extracellular Calcium Sensing and Signalling. *Nat. Rev. Mol. Cell Biol.* **2003**, *4* (7), 530–538. https://doi.org/10.1038/nrm1154.

(195) Walker, M. D.; Shane, E. Hypercalcemia: A Review. *Jama* **2022**, *328* (16), 1624–1636. https://doi.org/10.1001/jama.2022.18331.

(196) Wang, M.; Kussrow, A. K.; Ocana, M. F.; Chabot, J. R.; Lepsy, C. S.; Bornhop, D. J.; O'Hara, D. M. Physiologically Relevant Binding Affinity Quantification of Monoclonal Antibody PF-00547659 to Mucosal Addressin Cell Adhesion Molecule for in Vitro in Vivo Correlation. *Br. J. Pharmacol.* **2017**, *174* (1), 70–81. https://doi.org/10.1111/bph.13654.

(197) Ishiwari, F.; Hasebe, H.; Matsumura, S.; Hajjaj, F.; Horii-Hayashi, N.; Nishi, M.; Someya, T.; Fukushima, T. Bioinspired Design of a Polymer Gel Sensor for the Realization of Extracellular Ca^{2+} Imaging. *Sci. Rep.* **2016**, *6*, 1–11. https://doi.org/10.1038/srep24275.

(198) Jarmoskaite, I.; Alsadhan, I.; Vaidyanathan, P. P.; Herschlag, D. How to Measure and Evaluate Binding Affinities. *Elife* **2020**, *9*, 1–34. https://doi.org/10.7554/ELIFE.57264.

(199) Tastanova, A.; Folcher, M.; Müller, M.; Camenisch, G.; Ponti, A.; Horn, T.; Tikhomirova, M. S.; Fussenegger, M. Synthetic Biology-Based Cellular Biomedical Tattoo for Detection of Hypercalcemia Associated with Cancer. *Sci. Transl. Med.* **2018**, *10* (437), 1–12. https://doi.org/10.1126/scitranslmed.aap8562.

(200) MARTIN, N. H.; PERKINS, D. J. The Interaction of Serum Albumins with Calcium. *Biochem. J.* **1950**, *47* (3), 323–326. https://doi.org/10.1042/bj0470323.

(201) Gao, M.; Li, Y.; Chen, X.; Li, S.; Ren, L.; Tang, B. Z. Aggregation-Induced Emission Probe for Light-Up and in Situ Detection of Calcium Ions at High Concentration. *ACS Appl. Mater. Interfaces* **2018**, *10* (17), 14410–14417. https://doi.org/10.1021/acsami.8b00952.

(202) Tang, S.; Wong, H. C.; Wang, Z. M.; Huang, Y.; Zou, J.; Zhuo, Y.; Pennati, A.; Gadda, G.; Delbono, O.; Yang, J. J. Design and Application of a Class of Sensors to Monitor Ca^{2+} Dynamics in High Ca^{2+} Concentration Cellular Compartments. *Proc. Natl. Acad. Sci. U. S. A.* **2011**, *108* (39), 16265–16270. https://doi.org/10.1073/pnas.1103015108.

(203) Zamani, M.; Robson, J. M.; Fan, A.; Bono, M. S.; Furst, A. L.; Klapperich, C. M. Electrochemical Strategy for Low-Cost Viral Detection. *ACS Cent. Sci.* **2021**, *7* (6), 963–972. https://doi.org/10.1021/acscentsci.1c00186.

(204) Zamani, M.; Klapperich, C. M.; Furst, A. L. Recent Advances in Gold Electrode Fabrication for Low-Resource Setting Biosensing. *Lab Chip* **2023**, *23* (5), 1410–1419. https://doi.org/10.1039/d2lc00552b.

(205) Greenwald, E. C.; Mehta, S.; Zhang, J. Genetically Encoded Fluorescent Biosensors Illuminate the Spatiotemporal Regulation of Signaling Networks. *Chem. Rev.* **2018**, *118* (24), 11707–11794. https://doi.org/10.1021/acs.chemrev.8b00333.

(206) Wang, Y.; Katyal, P.; Montclare, J. K. Protein-Engineered Functional Materials. *Adv. Healthc. Mater.* **2019**, *8* (11), 1–33. https://doi.org/10.1002/adhm.201801374.

(207) Voet, A. R.; Tame, J. R. Protein-Templated Synthesis of Metal-Based Nanomaterials. *Curr. Opin. Biotechnol.* **2017**, *46*, 14–19. https://doi.org/10.1016/j.copbio.2016.10.015.

(208) Solomonov, A.; Shimanovich, U. Self-Assembly in Protein-Based Bionanomaterials. *Isr. J. Chem.* **2020**, *60* (12), 1152–1170. https://doi.org/10.1002/ijch.201900083.

(209) Köhler, V.; Wilson, Y. M.; Lo, C.; Sardo, A.; Ward, T. R. Protein-Based Hybrid Catalysts-Design and Evolution. *Curr. Opin. Biotechnol.* **2010**, *21* (6), 744–752. https://doi.org/10.1016/j.copbio.2010.09.004.

(210) Lee, J. Y.; Kim, J. S.; Park, J. C.; Nam, Y. S. Protein-Quantum Dot Nanohybrids for Bioanalytical Applications. *Wiley Interdiscip. Rev. Nanomedicine Nanobiotechnology* **2016**, *8* (2), 178–190. https://doi.org/10.1002/wnan.1345.

(211) Elzoghby, A. O.; Hemasa, A. L.; Freag, M. S. Hybrid Protein-Inorganic Nanoparticles: From Tumor-Targeted Drug Delivery to Cancer Imaging. *J. Control. Release* **2016**, *243*, 303–322. https://doi.org/10.1016/j.jconrel.2016.10.023.

(212) Ge, J.; Neofytou, E.; Lei, J.; Beygui, R. E.; Zare, R. N. Protein-Polymer Hybrid Nanoparticles for Drug Delivery. *Small* **2012**, *8* (23), 3573–3578. https://doi.org/10.1002/smll.201200889.

(213) Abe, S.; Maity, B.; Ueno, T. Design of a Confined Environment Using Protein Cages and Crystals for the Development of Biohybrid Materials. *Chem. Commun.* **2016**, *52* (39), 6496–6512. https://doi.org/10.1039/c6cc01355d.

(214) Saveleva, M. S.; Eftekhari, K.; Abalymov, A.; Douglas, T. E. L.; Volodkin, D.; Parakhonskiy, B. V.; Skirtach, A. G. Hierarchy of Hybrid Materials-the Place of Inorganics-in-Organics in It, Their Composition and Applications. *Front. Chem.* **2019**, *7* (APR), 1–21. https://doi.org/10.3389/fchem.2019.00179.

(215) Wang, H. Y.; Zhang, Y. Q. Processing Silk Hydrogel and Its Applications in Biomedical Materials. *Biotechnol. Prog.* **2015**, *31* (3), 630–640. https://doi.org/10.1002/btpr.2058.

(216) Bale, J. B.; Gonen, S.; Liu, Y.; Sheffler, W.; Ellis, D.; Thomas, C.; Cascio, D.; Yeates, T. O.; Gonen, T.; King, N. P.; Baker, D. Accurate Design of Megadalton-Scale Two-Component Icosahedral Protein Complexes. *Science.* **2016**, *353* (6297), 389–395. https://doi.org/10.5061/dryad.8c65s.

(217) Rother, M.; Nussbaumer, M. G.; Renggli, K.; Bruns, N. Protein Cages and Synthetic Polymers: A Fruitful Symbiosis for Drug Delivery Applications, Bionanotechnology and

Materials Science. *Chem. Soc. Rev.* **2016**, *45* (22), 6213–6249. https://doi.org/10.1039/c6cs00177g.

(218) De La Escosura, A.; Nolte, R. J. M.; Cornelissen, J. J. L. M. Viruses and Protein Cages as Nanocontainers and Nanoreactors. *J. Mater. Chem.* **2009**, *19* (16), 2274–2278. https://doi.org/10.1039/b815274h.

(219) Aumiller, W. M.; Uchida, M.; Douglas, T. Protein Cage Assembly across Multiple Length Scales. *Chem. Soc. Rev.* **2018**, *47* (10), 3433–3469. https://doi.org/10.1039/c7cs00818j.

(220) Bhaskar, S.; Lim, S. Engineering Protein Nanocages as Carriers for Biomedical Applications. *NPG Asia Mater.* **2017**, *9* (4), 1–18. https://doi.org/10.1038/am.2016.128.

(221) Elzoghby, A. O.; Elgohary, M. M.; Kamel, N. M. *Implications of Protein- and Peptide-Based Nanoparticles as Potential Vehicles for Anticancer Drugs*, 1st ed.; Advances in Protein Chemistry and Structural Biology, 2015; Vol. 98. https://doi.org/10.1016/bs.apcsb.2014.12.002.

(222) Molino, N. M.; Wang, S. W. Caged Protein Nanoparticles for Drug Delivery. *Curr. Opin. Biotechnol.* **2014**, *28*, 75–82. https://doi.org/10.1016/j.copbio.2013.12.007.

(223) Schoonen, L.; Van Hest, J. C. M. Functionalization of Protein-Based Nanocages for Drug Delivery Applications. *Nanoscale* **2014**, *6* (13), 7124–7141. https://doi.org/10.1039/c4nr00915k.

(224) Zang, J.; Zheng, B.; Zhang, X.; Arosio, P.; Zhao, G. Design and Site-Directed Compartmentalization of Gold Nanoclusters within the Intrasubunit Interfaces of Ferritin Nanocage. *J. Nanobiotechnology* **2019**, *17* (1), 1–12. https://doi.org/10.1186/s12951-019-0512-0.

(225) Moon, H.; Lee, J.; Min, J.; Kang, S. Developing Genetically Engineered Encapsulin Protein Cage Nanoparticles as a Targeted Delivery Nanoplatform. *Biomacromolecules* **2014**, *15* (10), 3794–3801. https://doi.org/10.1021/bm501066m.

(226) Tarhini, M.; Greige-Gerges, H.; Elaissari, A. Protein-Based Nanoparticles: From Preparation to Encapsulation of Active Molecules. *Int. J. Pharm.* **2017**, *522* (1–2), 172–197. https://doi.org/10.1016/j.ijpharm.2017.01.067.

(227) Despanie, J.; Dhandhukia, J. P.; Hamm-Alvarez, S. F.; MacKay, J. A. Elastin-like Polypeptides: Therapeutic Applications for an Emerging Class of Nanomedicines. *J. Control. Release* **2016**, *240*, 93–108. https://doi.org/10.1016/j.jconrel.2015.11.010.

(228) Majithia, R.; Patterson, J.; Bondos, S. E.; Meissner, K. E. On the Design of Composite Protein-Quantum Dot Biomaterials via Self-Assembly. *Biomacromolecules* **2011**, *12* (10), 3629–3637. https://doi.org/10.1021/bm200889k.

(229) Allen, M.; Willits, D.; Mosolf, J.; Young, M.; Douglas, T. Protein Cage Constrained Synthesis of Ferrimagnetic Iron Oxide Nanoparticles. *Adv. Mater.* **2002**, *14* (21), 1562–

1565.

(230) Fan, K.; Cao, C.; Pan, Y.; Lu, D.; Yang, D.; Feng, J.; Song, L.; Liang, M.; Yan, X. Magnetoferritin Nanoparticles for Targeting and Visualizing Tumour Tissues. *Nat. Nanotechnol.* **2012**, *7* (7), 459–464. https://doi.org/10.1038/nnano.2012.90.

(231) Nabar, G. M.; Winter, J. O.; Wyslouzil, B. E. Nanoparticle Packing within Block Copolymer Micelles Prepared by the Interfacial Instability Method. *Soft Matter* **2018**, *14* (17), 3324–3335. https://doi.org/10.1039/c8sm00425k.

(232) Zhang, W. J.; Hong, C. Y.; Pan, C. Y. Polymerization-Induced Self-Assembly of Functionalized Block Copolymer Nanoparticles and Their Application in Drug Delivery. *Macromol. Rapid Commun.* **2019**, *40* (2), 1–10. https://doi.org/10.1002/marc.201800279.

(233) Mable, C. J.; Gibson, R. R.; Prevost, S.; McKenzie, B. E.; Mykhaylyk, O. O.; Armes, S. P. Loading of Silica Nanoparticles in Block Copolymer Vesicles during Polymerization-Induced Self-Assembly: Encapsulation Efficiency and Thermally Triggered Release. *J. Am. Chem. Soc.* **2015**, *137* (51), 16098–16108. https://doi.org/10.1021/jacs.5b10415.

(234) Urry, D. W.; Luan, C. H.; Parker, T. M.; Gowda, D. C.; Prasad, K. U.; Reid, M. C.; Safavy, A. Temperature of Polypeptide Inverse Temperature Transition Depends on Mean Residue Hydrophobicity. *J. Am. Chem. Soc.* **1991**, *113* (11), 4346–4348. https://doi.org/10.1021/ja00011a057.

(235) Molina, R. S.; Qian, Y.; Wu, J.; Shen, Y.; Campbell, R. E.; Drobizhev, M.; Hughes, T. E. Understanding the Fluorescence Change in Red Genetically Encoded Calcium Ion Indicators. *Biophys. J.* **2019**, *116* (10), 1873–1886. https://doi.org/10.1016/j.bpj.2019.04.007.

(236) Park, W. M.; Yee, C. M.; Champion, J. A. Self-Assembled Hybrid Supraparticles That Proteolytically Degrade Tumor Necrosis Factor-α. *J. Mater. Chem. B* **2016**, *4* (9), 1633–1639. https://doi.org/10.1039/c5tb01647a.

(237) Du, J.; Sun, H. Polymer/TiO2 Hybrid Vesicles for Excellent UV Screening and Effective Encapsulation of Antioxidant Agents. *ACS Appl. Mater. Interfaces* **2014**, *6* (16), 13535–13541. https://doi.org/10.1021/am502663j.

(238) Hasmath Farzana, M.; Meenakshi, S. Synergistic Effect of Chitosan and Titanium Dioxide on the Removal of Toxic Dyes by the Photodegradation Technique. *Ind. Eng. Chem. Res.* **2014**, *53* (1), 55–63. https://doi.org/10.1021/ie402347g.

(239) Xiao, J.; Chen, W.; Wang, F.; Du, J. Polymer/TiO_2 Hybrid Nanoparticles with Highly Effective UV-Screening but Eliminated Photocatalytic Activity. **2013**.

(240) Auger, J. C.; Stout, B. Dependent Light Scattering in White Paint Films: Clarification and Application of the Theoretical Concepts. *J. Coatings Technol. Res.* **2012**, *9* (3), 287–295. https://doi.org/10.1007/s11998-011-9371-9.

(241) Tolosana-Moranchel, A.; Pecharromán, C.; Faraldos, M.; Bahamonde, A. Strong Effect of Light Scattering by Distribution of TiO2 Particle Aggregates on Photocatalytic Efficiency in Aqueous Suspensions. *Chem. Eng. J.* **2021**, *403* (July 2020). https://doi.org/10.1016/j.cej.2020.126186.

(242) Kanehira, K.; Yano, Y.; Hasumi, H.; Fukuhara, H.; Inoue, K.; Hanazaki, K.; Yao, M. Fluorescence Enhancement Effect of TiO2 Nanoparticles and Application for Photodynamic Diagnosis. *Int. J. Mol. Sci.* **2019**, *20* (15). https://doi.org/10.3390/ijms20153698.

(243) Bers, D. M.; Patton, C. W.; Nuccitelli, R. A Practical Guide to the Preparation of Ca^{2+} Buffers. *Methods Cell Biol.* **2010**, *99* (C), 1–26. https://doi.org/10.1016/B978-0-12-374841-6.00001-3.

(244) Moorcroft, M. J.; Davis, J.; Compton, R. G. Detection and Determination of Nitrate and Nitrite: A Review. *Talanta* **2001**, *54* (5), 785–803. https://doi.org/10.1016/S0039-9140(01)00323-X.

(245) Cantera, J. J. L.; Stein, L. Y. Role of Nitrite Reductase in the Ammonia-Oxidizing Pathway of Nitrosomonas Europaea. *Arch. Microbiol.* **2007**, *188* (4), 349–354. https://doi.org/10.1007/s00203-007-0255-4.

(246) Liu, T.; Hu, S.; Guo, J. Enhancing Mainstream Nitrogen Removal by Employing Nitrate/Nitrite-Dependent Anaerobic Methane Oxidation Processes. *Crit. Rev. Biotechnol.* **2019**, *39* (5), 732–745. https://doi.org/10.1080/07388551.2019.1598333.

(247) Bellido-Pedraza, C. M.; Calatrava, V.; Llamas, A.; Fernandez, E.; Sanz-Luque, E.; Galvan, A. Nitrous Oxide Emissions from Nitrite Are Highly Dependent on Nitrate Reductase in the Microalga Chlamydomonas Reinhardtii. *Int. J. Mol. Sci.* **2022**, *23* (16). https://doi.org/10.3390/ijms23169412.

(248) Arp, D. J.; Sayavedra-Soto, L. A.; Hommes, N. G. Molecular Biology and Biochemistry of Ammonia Oxidation by Nitrosomonas Europaea. *Arch. Microbiol.* **2002**, *178* (4), 250–255. https://doi.org/10.1007/s00203-002-0452-0.

(249) Sayavedra-Soto, L. A.; Hommes, N. G.; Russell, S. A.; Arp, D. J. Induction of Ammonia Monooxygenase and Hydroxylamine Oxidoreductase MRNAs by Ammonium in Nitrosomonas Europaea. *Mol. Microbiol.* **1996**, *20* (3), 541–548. https://doi.org/10.1046/j.1365-2958.1996.5391062.x.

(250) Cabail, M. Z.; Pacheco, A. A. Selective One-Electron Reduction of Nitrosomonas Europaea Hydroxylamine Oxidoreductase with Nitric Oxide. *Inorg. Chem.* **2003**, *42* (2), 270–272. https://doi.org/10.1021/ic025779n.

(251) Akinnawo, S. O. Eutrophication: Causes, Consequences, Physical, Chemical and Biological Techniques for Mitigation Strategies. *Environ. Challenges* **2023**, *12* (March). https://doi.org/10.1016/j.envc.2023.100733.

(252) Shi, H.; Fu, L.; Chen, F.; Zhao, S.; Lai, G. Preparation of Highly Sensitive Electrochemical Sensor for Detection of Nitrite in Drinking Water Samples. *Environ. Res.* **2022**, *209* (December 2021), 3–8. https://doi.org/10.1016/j.envres.2022.112747.

(253) Keszler, A.; Piknova, B.; Schechter, A. N.; Hogg, N. The Reaction between Nitrite and Oxyhemoglobin: A Mechanistic Study. *J. Biol. Chem.* **2008**, *283* (15), 9615–9622. https://doi.org/10.1074/jbc.M705630200.

(254) Doyle, M. P.; Pickering, R. A.; DeWeert, T. M.; Hoekstra, J. W.; Pater, D. Kinetics and Mechanism of the Oxidation of Human Deoxyhemoglobin by Nitrites. *J. Biol. Chem.* **1981**, *256* (23), 12393–12398. https://doi.org/10.1016/s0021-9258(18)43285-1.

(255) Min, H.; Han, Z.; Wang, M.; Li, Y.; Zhou, T.; Shi, W.; Cheng, P. A Water-Stable Terbium Metal-Organic Framework as a Highly Sensitive Fluorescent Sensor for Nitrite. *Inorg. Chem. Front.* **2020**, *7* (18), 3379–3385. https://doi.org/10.1039/d0qi00780c.

(256) Nightingale, A. M.; Hassan, S. U.; Warren, B. M.; Makris, K.; Evans, G. W. H.; Papadopoulou, E.; Coleman, S.; Niu, X. A Droplet Microfluidic-Based Sensor for Simultaneous in Situ Monitoring of Nitrate and Nitrite in Natural Waters. *Environ. Sci. Technol.* **2019**, *53* (16), 9677–9685. https://doi.org/10.1021/acs.est.9b01032.

(257) Ensafi, A. A.; Amini, M. A Highly Selective Optical Sensor for Catalytic Determination of Ultra-Trace Amounts of Nitrite in Water and Foods Based on Brilliant Cresyl Blue as a Sensing Reagent. *Sensors Actuators, B Chem.* **2010**, *147* (1), 61–66. https://doi.org/10.1016/j.snb.2010.03.014.

(258) Li, D.; Wang, T.; Li, Z.; Xu, X.; Wang, C.; Duan, Y. Application of Graphene-Based Materials for Detection of Nitrate and Nitrite in Water—a Review. *Sensors (Switzerland)* **2020**, *20* (1), 1–35. https://doi.org/10.3390/s20010054.

(259) Sánchez, C.; Itakura, M.; Okubo, T.; Matsumoto, T.; Yoshikawa, H.; Gotoh, A.; Hidaka, M.; Uchida, T.; Minamisawa, K. The Nitrate-Sensing NasST System Regulates Nitrous Oxide Reductase and Periplasmic Nitrate Reductase in Bradyrhizobium Japonicum. *Environ. Microbiol.* **2014**, *16* (10), 3263–3274. https://doi.org/10.1111/1462-2920.12546.

(260) Webb, B.; Sali, A. Comparative Protein Structure Modeling Using MODELLER. *Curr. Protoc. Bioinforma.* **2016**, *2016*, 5.6.1-5.6.37. https://doi.org/10.1002/cpbi.3.

(261) Brownstein, M. J.; Khodursky, A. B.; Charlie, C.; Michael, J. *Functional Genomics-Methods in Molecular Biology*; 2003; Vol. 224.

(262) Seeliger, D.; De Groot, B. L. Ligand Docking and Binding Site Analysis with PyMOL and Autodock/Vina. *J. Comput. Aided. Mol. Des.* **2010**, *24* (5), 417–422. https://doi.org/10.1007/s10822-010-9352-6.

(263) Trott, O.; Olson, A. J. AutoDock Vina: Improving the Speed and Accuracy of Docking with a New Scoring Function, Efficient Optimization, and Multithreading. *J. Comput. Chem.* **2010**, *31* (2), 455–461. https://doi.org/10.1002/jcc.21334.

(264) Rana, P.; Panda, L.; Murmu, N.; Bag, B. P.; Sahu, S. N. Fluorometric Sensing of Hydroxylamine in an Aqueous Medium Utilizing a Diphenyl Imidazole-Based Probe. *Org. Biomol. Chem.* **2020**, *18* (30), 5963–5971. https://doi.org/10.1039/d0ob00608d.

(265) Sedgwick, A. C.; Chapman, R. S. L.; Gardiner, J. E.; Peacock, L. R.; Kim, G.; Yoon, J.; Bull, S. D.; James, T. D. A Bodipy Based Hydroxylamine Sensor. *Chem. Commun.* **2017**, *53* (75), 10441–10443. https://doi.org/10.1039/c7cc05872a.

(266) Wang, Y.; Wang, L.; Chen, H.; Hu, X.; Ma, S. Fabrication of Highly Sensitive and Stable Hydroxylamine Electrochemical Sensor Based on Gold Nanoparticles and Metal-Metalloporphyrin Framework Modified Electrode. *ACS Appl. Mater. Interfaces* **2016**, *8* (28), 18173–18181. https://doi.org/10.1021/acsami.6b04819.

(267) Seike, Y.; Fukumori, R.; Senga, Y.; Oka, H.; Fujinaga, K.; Okumura, M. A Simple and Sensitive Method for the Determination of Hydroxylamine in Fresh-Water Samples Using Hypochlorite Followed by Gas Chromatography. *Anal. Sci.* **2004**, *20* (1), 139–142. https://doi.org/10.2116/analsci.20.139.

(268) Rodrigues, C. H. M.; Pires, D. E. V.; Ascher, D. B. DynaMut2: Assessing Changes in Stability and Flexibility upon Single and Multiple Point Missense Mutations. *Protein Sci.* **2021**, *30* (1), 60–69. https://doi.org/10.1002/pro.3942.

(269) Jo, S.; Pearson, E.; Yoon, D.; Kim, J.; Park, W. M. Self-Assembly of Microstructured Protein Coatings with Programmable Functionality for Fluorescent Biosensors. *bioRxiv* **2024**, 2005–2024.

Appendix A - Copyrights Permissions

Appendix Figure A.1 Copyrights for Chapter 1 from ACS Publications

Appendix B - Protein Sequences

Protein	Sequence
Z_R-ELP	MKGSLEIRAAALRRRNTALRTRVAELRQRVQRLRNEVSQYETRYGPL$(G_4S)_2$G[$(VPGVG)_2$VPGFG$(VPGVG)_2]_5$VPGC
mCherry-Z_E	MGGSRSMVSKGEEDNMAIIKEFMRFKVHMEGSVNGHEFEIEGEGEGRPYEGTQTAKLKVTKGGPLPFAWDILSPQFMYGSKAYVKHPADIPDYLKLSFPEGFKWERVMNFEDGGVVTVTQDSSLQDGEFIYKVKLRGTNFPSDGPVMQKKTMGWEASSERMYPEDGALKGEIKQRLKLKDGGHYDAEVKTTYKAKKPVQLPGAYNVNIKLDITSHNEDYTIVEQYERAEGRHSTGGMDELYKSKLRGSGSLEIEAAALEQENTALETEVAELEQEVQRLENIVSQYRTRYGPLRSHHHHHH
EGFP-Z_E	MGGSRSMASKGEELFTGVVPILVELDGDVNGHKFSVSGEGEGDATYGKLTLKFICTTGKLPVPWPTLVTTLCYGVQCFSRYPDHMKRHDFFKSAMPEGYVQERTIFFKDDGNYKTRAEVKFEGDTLVNRIELKGIDFKEDGNILGHKLEYNYNSHNVYIMADKQKNGIKVNFKTRHNIEDGSVQLADHYQQNTPIGDGPVLLPDNHYLSTQSALSKDPNEKRDHMVLLEFVTAAGITHGMDELYNLRGSGSLEIEAAALEQENTALETEVAELEQEVQRLENIVSQYRTRYGPLRSHHHHHH
GCaMP6m-Z_E	MGGSSRRKWNKTGHAVRAIGRLSSLENVYIKADKQKNGIKANFKIRHNIEDGGVQLAYHYQQNTPIGDGPVLLPDNHYLSVQSKLSKDPNEKRDHMVLLEFVTAAGITLGMDELYKGGTGGSMVSKGEELFTGVVPILVELDGDVNGHKFSVSGEGEGDATYGKLTLKFICTTGKLPVPWPTLVTTLTYGVQCFSRYPDHMKQHDFFKSAMPEGYIQERTIFFKDDGNYKTRAEVKFEGDTLVNRIELKGIDFKEDGNILGHKLEYNLPDQLTEEQIAEFKEAFSLFDKDGDGTITTKELGTVMRSLGQNPTEAELQDMINEVDADGDGTIDFPEFLTMMARKGSYRDTEEEIREAFGVFDKDGNGYISAAELRHVMTNLGEKLTDEEVDEMIREADIDGDGQVNYEEFVQMMTAKGGSGGTGGSGGTGGSLEIEAAALEQENTALETEVAELEQEVQRLENIVSQYRTRYGPLRSHHHHHH
OGECO1-Z_E	MVDSSRRKWIKAGHAVRAIGRLSSPVVSERMYPEDGVLKSEIKKGLRLKDGGHYAAEVKTTYKAKKPVQLPGAYIVDIKLDIVSHNEDYTIVEQCERAEGRHPTGGRDELYKGGTGGSLVSKGEEDNMAIIKEFMRFKVHMEGSVNGHEFEIEGEGEGRPYEAFQTAKLKVTKGGPLPFAWDILSPQFTYGSKAYIKHPADIPDYFKLSFPEGFRWERVMNFEDGGIIHVNQDSSLQDGVFIYKVKLRGTNFPPDGPVMQKKTMGWEATRDQLTEEQIAEFKEAFSLFDKDGDGTITTKELGTVLRSLGQNPTEAELQDMINEVDADGDGTFDFPEFLTMMARRMNDTDSEVEIREAFRVFDNDGNGYIGAAELRHVMTDLGEKLTDEEVDEMIRVADIDGDGQVNYEEFVQM

	MTAKGGSGGTGGSGGTGGSLEIEAAALEQENTALETEVAELEQEVQ RLENIVSQYRTRYGPLRSHHHHHH
CFP-NasT	MVSKGEELFGGIVPILVELEGDVNGHKFSVSGEGEGDATYGKLTLK FICTTGKLPVPWPTLVTTLTWGVQCFSRYPDHMKQHDFFKSVMPEG YVQERTIFFKDDGNYKTRAEVKFEGDTLVNRIELKGIDFKEDGNILG HKLEYNYISHNVYITADKQKNGIKANFKARHNITDGSVQLADHYQQ NTPIGDGPVILPDNHYLSTQSKLSKDPNEKRDHMVLLEFVTAAGITH GMDELYKMSAEQSPKIVIVDESPIRAAILEEGLREAGFTQVAHIREM QSLLARIYAVDPDIILIDLENPSRDVLEAMFQVSRAVRRPIAMFVDQS DSASIQASVEAGVSAYIVDGLKKERIKPILDLCVSRFNAFAKLQEELE RTKSQLEDRKIIERAKGILMKVKGLTEDEAYVLLRSTAMREKKKIGE IAQSIITASEMLKKL
NasS-mVenus	MTGPLRIGFIPLVDAAALIVAVDKGFTAAEGLDVELVREVSWSNVR DKLNIGLFDAAHLLAPVAIASSLGLGHVKVPIAAPFNLGINGNAITVS PTLHAALMEEIDGDRFDPLVTAKALARVVARRRKLGADPLTFGMTF PFSTHNYQLRFWMAAAGVDPDEDVRLVVLPPPYMVDSLANGHVD AFCVGAPWNSIAVDLGIGHILHFVSDILVHAAEKVLAVRQTWADKN PDVVASLVRAAVKAAEFIEHPENRIEAARILAQPERIGVDAEVIQRTL TGRLKISPDGTFRESGRYLLVGREGAGRPDPVQAAWLYAQMVRWG QTALAPDGVKTAMAVFRPDLYDAALGSRAAPSEAPAAFGAFAGPV FDPDNIRGHLEAFEVGRWKALPDNHYLSYQSALSKDPNEKRDHMV LLEFVTAAGITLGMDELYKGGSGGMVSKGEELFTGVVPILVELDGD VNGHKFSVSGEGEGDATYGKLTLKLICTTGKLPVPWPTLVTTLGYG LQCFARYPDHMKQHDFFKSAMPEGYVQERTIFFKDDGNYKTRAEV KFEGDTLVNRIELKGIDFKEDGNILGHKLEYNYNSHNVYITADKQK NGIKANFKIRHNIEDGGVQLADHYQQNTPIGDGPVLRSHHHHHH

Appendix Table B.1 Amino acid sequences of the recombinant protein building blocks.

Z_R-ELP, mCherry- Z_E, EGFP-Z_E, GCaMP6m-Z_E, OGECO1-Z_E and nitrite sensor. The protein domains and motifs are colored: Z_R (blue), Z_E (red), ELP (gray), mCherry (pink), EGFP (green), and GCaMP6m (purple), OGECO1 (orange), NasS (magenta), NasT (Navy), CFP (cyan), mVenus (yellow).

Appendix C - DNA Sequences and Plasmid Maps

C.1 pQE60-GCAMP6m-Z_E

Plasmid Map

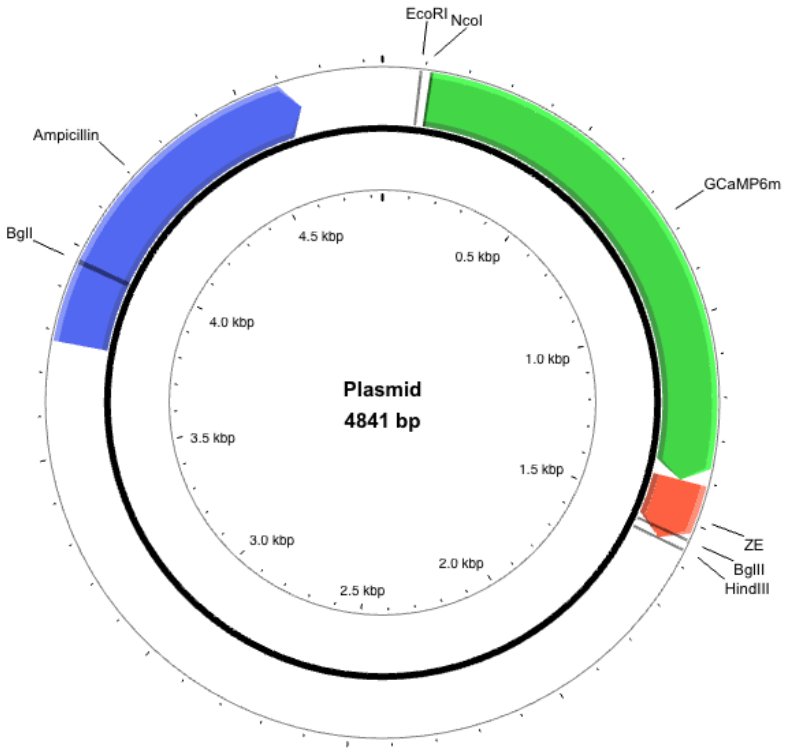

Appendix Figure C.1 Plasmid map of pQE60-GCaMP6m-Z_E

DNA sequence

CTCGAGAAATCATAAAAAATTTATTTGCTTTGTGAGCGGATAACAATTATAATAGAT

TCAATTGTGAGCGGATAACAATTTCACACAGAATTCATTAAAGAGGAGAAATTAAC

CATGGGAGGATCCTCACGTCGTAAGTGGAATAAGACAGGTCACGCAGTCAGAGCTA

TAGGTCGGCTGAGCTCACTCGAGAACGTCTATATCAAGGCCGACAAGCAGAAGAAC

GGCATCAAGGCGAACTTCAAGATCCGCCACAACATCGAGGACGGCGGCGTGCAGCT

CGCCTACCACTACCAGCAGAACACCCCCATCGGCGACGGCCCCGTGCTGCTGCCCG

ACAACCACTACCTGAGCGTGCAGTCCAAACTTTCGAAAGACCCCAACGAGAAGCGC

GATCACATGGTCCTGCTGGAGTTCGTGACCGCCGCCGGGATCACTCTCGGCATGGAC

GAGCTGTACAAGGGCGGTACCGGAGGGAGCATGGTGAGCAAGGGCGAGGAGCTGT

TCACCGGGGTGGTGCCCATCCTGGTCGAGCTGGACGGCGACGTAAACGGCCACAAG

TTCAGCGTGTCCGGCGAGGGTGAGGGCGATGCCACCTACGGCAAGCTGACCCTGAA

GTTCATCTGCACCACCGGCAAGCTGCCCGTGCCCTGGCCCACCCTCGTGACCACCCT

GACCTACGGCGTGCAGTGCTTCAGCCGCTACCCCGACCACATGAAGCAGCACGACT

TCTTCAAGTCCGCCATGCCCGAAGGCTACATCCAGGAGCGCACCATCTTCTTCAAGG

ACGACGGCAACTACAAGACCCGCGCCGAGGTGAAGTTCGAGGGCGACACCCTGGTG

AACCGCATCGAGCTGAAGGGCATCGACTTCAAGGAGGACGGCAACATCCTGGGGCA

CAAGCTGGAGTACAACCTGCCGGACCAACTGACTGAAGAGCAGATCGCAGAATTTA

AAGAGGCTTTCTCCCTATTTGACAAGGACGGGGATGGGACAATAACAACCAAGGAG

CTGGGGACGGTGATGCGGTCTCTGGGGCAGAACCCCACAGAAGCAGAGCTGCAGGA

CATGATCAATGAAGTAGATGCCGACGGTGACGGCACAATCGACTTCCCTGAGTTCCT

GACAATGATGGCAAGAAAAGGGAGCTACAGGGACACGGAAGAAGAAATTAGAGAA

GCGTTCGGTGTGTTTGATAAGGATGGCAATGGCTACATCAGTGCAGCAGAGCTTCGC

CACGTGATGACAAACCTTGGAGAGAAGTTAACAGATGAAGAGGTTGATGAAATGAT

CAGGGAAGCAGACATCGATGGGGATGGTCAGGTAAACTACGAAGAGTTTGTACAAA

TGATGACAGCGAAGGGCGGTAGCGGTGGCACCGGTGGCTCTGGCGGTACCGGCGGA

TCCCTGGAAATCGAAGCGGCGGCGCTGGAACAGGAAAACACCGCGCTGGAAACCG

AAGTTGCGGAACTGGAACAGGAAGTTCAGCGTCTGGAAAACATCGTTTCTCAGTAC

CGTACCCGTTACGGTCCGCTGAGATCTCATCACCATCACCATCACTAAGCTTAATTA

GCTGAGCTTGGACTCCTGTTGATAGATCCAGTAATGACCTCAGAACTCCATCTGGAT

TTGTTCAGAACGCTCGGTTGCCGCCGGGCGTTTTTTATTGGTGAGAATCCAAGCTAG

CTTGGCGAGATTTTCAGGAGCTAAGGAAGCTAAAATGGAGAAAAAAATCACTGGAT

ATACCACCGTTGATATATCCCAATGGCATCGTAAAGAACATTTTGAGGCATTTCAGT

CAGTTGCTCAATGTACCTATAACCAGACCGTTCAGCTGGATATTACGGCCTTTTTAA

AGACCGTAAAGAAAAATAAGCACAAGTTTTATCCGGCCTTTATTCACATTCTTGCCC

GCCTGATGAATGCTCATCCGGAATTTCGTATGGCAATGAAAGACGGTGAGCTGGTG

ATATGGGATAGTGTTCACCCTTGTTACACCGTTTTCCATGAGCAAACTGAAACGTTTT

CATCGCTCTGGAGTGAATACCACGACGATTTCCGGCAGTTTCTACACATATATTCGC

AAGATGTGGCGTGTTACGGTGAAAACCTGGCCTATTTCCCTAAAGGGTTTATTGAGA

ATATGTTTTTCGTCTCAGCCAATCCCTGGGTGAGTTTCACCAGTTTTGATTTAAACGT

GGCCAATATGGACAACTTCTTCGCCCCCGTTTTCACCATGCATGGGCAAATATTATA

CGCAAGGCGACAAGGTGCTGATGCCGCTGGCGATTCAGGTTCATCATGCCGTCTGTG

ATGGCTTCCATGTCGGCAGAATGCTTAATGAATTACAACAGTACTGCGATGAGTGGC

AGGGCGGGGCGTAATTTTTTTAAGGCAGTTATTGGTGCCCTTAAACGCCTGGGGTAA

TGACTCTCTAGCTTGAGGCATCAAATAAAACGAAAGGCTCAGTCGAAAGACTGGGC

CTTTCGTTTTATCTGTTGTTTGTCGGTGAACGCTCTCCTGAGTAGGACAAATCCGCCG

CTCTAGAGCTGCCTCGCGCGTTTCGGTGATGACGGTGAAAACCTCTGACACATGCAG

CTCCCGGAGACGGTCACAGCTTGTCTGTAAGCGGATGCCGGGAGCAGACAAGCCCG

TCAGGGCGCGTCAGCGGGTGTTGGCGGGTGTCGGGGCGCAGCCATGACCCAGTCAC

GTAGCGATAGCGGAGTGTATACTGGCTTAACTATGCGGCATCAGAGCAGATTGTACT

GAGAGTGCACCATATGCGGTGTGAAATACCGCACAGATGCGTAAGGAGAAAATACC

GCATCAGGCGCTCTTCCGCTTCCTCGCTCACTGACTCGCTGCGCTCGGTCGTTCGGCT

GCGGCGAGCGGTATCAGCTCACTCAAAGGCGGTAATACGGTTATCCACAGAATCAG

GGGATAACGCAGGAAAGAACATGTGAGCAAAAGGCCAGCAAAAGGCCAGGAACCG

TAAAAAGGCCGCGTTGCTGGCGTTTTTCCATAGGCTCCGCCCCCCTGACGAGCATCA

CAAAAATCGACGCTCAAGTCAGAGGTGGCGAAACCCGACAGGACTATAAAGATACC

AGGCGTTTCCCCCTGGAAGCTCCCTCGTGCGCTCTCCTGTTCCGACCCTGCCGCTTAC

CGGATACCTGTCCGCCTTTCTCCCTTCGGGAAGCGTGGCGCTTTCTCATAGCTCACGC

TGTAGGTATCTCAGTTCGGTGTAGGTCGTTCGCTCCAAGCTGGGCTGTGTGCACGAA

CCCCCCGTTCAGCCCGACCGCTGCGCCTTATCCGGTAACTATCGTCTTGAGTCCAAC

CCGGTAAGACACGACTTATCGCCACTGGCAGCAGCCACTGGTAACAGGATTAGCAG

AGCGAGGTATGTAGGCGGTGCTACAGAGTTCTTGAAGTGGTGGCCTAACTACGGCT

ACACTAGAAGGACAGTATTTGGTATCTGCGCTCTGCTGAAGCCAGTTACCTTCGGAA

AAAGAGTTGGTAGCTCTTGATCCGGCAAACAAACCACCGCTGGTAGCGGTGGTTTTT

TTGTTTGCAAGCAGCAGATTACGCGCAGAAAAAAAGGATCTCAAGAAGATCCTTTG

ATCTTTTCTACGGGGTCTGACGCTCAGTGGAACGAAAACTCACGTTAAGGGATTTTG

GTCATGAGATTATCAAAAAGGATCTTCACCTAGATCCTTTTAAATTAAAAATGAAGT

TTTAAATCAATCTAAAGTATATATGAGTAAACTTGGTCTGACAGTTACCAATGCTTA

ATCAGTGAGGCACCTATCTCAGCGATCTGTCTATTTCGTTCATCCATAGTTGCCTGAC

TCCCCGTCGTGTAGATAACTACGATACGGGAGGGCTTACCATCTGGCCCCAGTGCTG

CAATGATACCGCGAGACCCACGCTCACCGGCTCCAGATTTATCAGCAATAAACCAG

CCAGCCGGAAGGGCCGAGCGCAGAAGTGGTCCTGCAACTTTATCCGCCTCCATCCA

GTCTATTAATTGTTGCCGGGAAGCTAGAGTAAGTAGTTCGCCAGTTAATAGTTTGCG

CAACGTTGTTGCCATTGCTACAGGCATCGTGGTGTCACGCTCGTCGTTTGGTATGGCT

TCATTCAGCTCCGGTTCCCAACGATCAAGGCGAGTTACATGATCCCCCATGTTGTGC

AAAAAAGCGGTTAGCTCCTTCGGTCCTCCGATCGTTGTCAGAAGTAAGTTGGCCGCA

GTGTTATCACTCATGGTTATGGCAGCACTGCATAATTCTCTTACTGTCATGCCATCCG

TAAGATGCTTTTCTGTGACTGGTGAGTACTCAACCAAGTCATTCTGAGAATAGTGTA

TGCGGCGACCGAGTTGCTCTTGCCCGGCGTCAATACGGGATAATACCGCGCCACATA

GCAGAACTTTAAAAGTGCTCATCATTGGAAAACGTTCTTCGGGGCGAAAACTCTCAA

GGATCTTACCGCTGTTGAGATCCAGTTCGATGTAACCCACTCGTGCACCCAACTGAT

CTTCAGCATCTTTTACTTTCACCAGCGTTTCTGGGTGAGCAAAAACAGGAAGGCAAA

ATGCCGCAAAAAAGGGAATAAGGGCGACACGGAAATGTTGAATACTCATACTCTTC

CTTTTTCAATATTATTGAAGCATTTATCAGGGTTATTGTCTCATGAGCGGATACATAT

TTGAATGTATTTAGAAAAATAAACAAATAGGGGTTCCGCGCACATTTCCCCGAAAA

GTGCCACCTGACGTCTAAGAAACCATTATTATCATGACATTAACCTATAAAAATAGG

CGTATCACGAGGCCCTTTCGTCTTCAC

C.2 pQE60-O-GECO1-Z_E

Plasmid Map

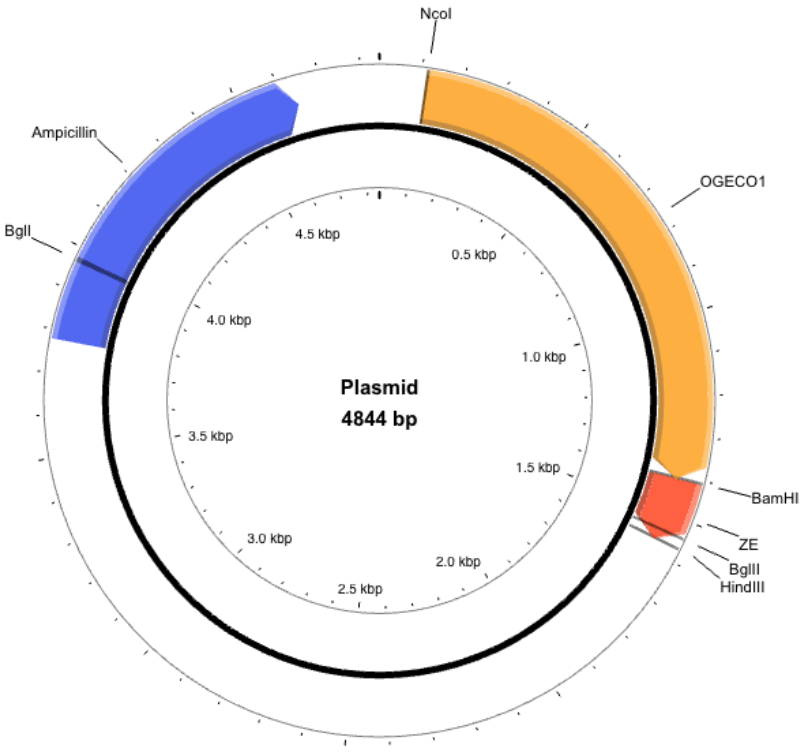

Appendix Figure C.2 Plasmid map of pQE60-OGECO1-Z_E

DNA sequence

CTCGAGAAATCATAAAAAATTTATTTGCTTTGTGAGCGGATAACAATTATAATAGAT

TCAATTGTGAGCGGATAACAATTTCACACAGAATTCATTAAAGAGGAGAAATTAAC

CATGGTCGACTCTTCACGTCGTAAGTGGATTAAGGCAGGTCACGCAGTCAGAGCTAT

AGGTCGGCTGAGCTCACCCGTGGTTTCCGAGCGGATGTACCCCGAGGACGGCGTCCT

GAAGAGCGAGATCAAGAAGGGGCTGAGGCTGAAGGACGGCGGCCACTACGCCGCC

GAGGTCAAGACCACCTACAAGGCCAAGAAGCCCGTGCAGCTGCCCGGCGCCTACAT

CGTCGACATAAAGTTGGACATCGTGTCCCACAACGAGGACTACACCATCGTGGAAC

AGTGCGAACGCGCCGAGGGCCGCCACCCCACCGGCGGCAGGGACGAGCTGTACAA

GGGAGGTACAGGAGGGAGTCTGGTGAGCAAGGGCGAGGAGGATAACATGGCCATC

ATCAAGGAGTTCATGCGCTTCAAGGTGCACATGGAGGGCTCCGTGAACGGCCACGA

GTTCGAGATCGAGGGCGAGGGCGAGGGCCGCCCCTACGAGGCCTTTCAGACCGCTA

AGCTGAAGGTGACCAAGGGTGGCCCCCTGCCCTTCGCCTGGGACATCCTGTCCCCTC

AGTTCACATACGGCTCCAAGGCCTACATTAAGCACCCAGCCGACATCCCCGACTACT

TTAAGCTGTCCTTCCCCGAGGGCTTCAGGTGGGAGCGCGTGATGAACTTCGAGGACG

GCGGCATTATTCACGTTAACCAGGACTCCTCCCTGCAGGACGGCGTATTCATCTACA

AGGTGAAGCTGCGCGGCACCAACTTCCCCCCCGACGGCCCCGTAATGCAGAAGAAG

ACAATGGGCTGGGAGGCTACGCGTGACCAACTGACTGAAGAGCAGATCGCAGAATT

TAAAGAGGCTTTCTCCCTATTTGACAAGGACGGGGATGGGACGATAACAACCAAGG

AGCTGGGGACGGTGTTGCGGTCTCTGGGGCAGAACCCCACAGAAGCAGAGCTGCAG

GACATGATCAATGAAGTAGATGCCGACGGTGACGGCACATTCGACTTCCCTGAGTTC

CTGACGATGATGGCAAGAAGAATGAATGACACAGACAGTGAAGTGGAAATTAGAG

AAGCGTTCCGCGTGTTTGATAATGACGGCAATGGCTACATCGGCGCAGCAGAGCTTC

GCCACGTGATGACAGACCTTGGAGAGAAGTTAACAGATGAGGAGGTTGATGAAATG

ATCAGGGTAGCAGACATCGATGGGGATGGTCAGGTAAACTACGAAGAGTTTGTACA

AATGATGACAGCGAAGGGCGGTAGCGGTGGCACCGGTGGCTCTGGCGGTACCGGCG

GATCCCTGGAAATCGAAGCGGCGGCGCTGGAACAGGAAAACACCGCGCTGGAAAC

CGAAGTTGCGGAACTGGAACAGGAAGTTCAGCGTCTGGAAAACATCGTTTCTCAGT

ACCGTACCCGTTACGGTCCGCTGAGATCTCATCACCATCACCATCACTAAGCTTAAT

TAGCTGAGCTTGGACTCCTGTTGATAGATCCAGTAATGACCTCAGAACTCCATCTGG

ATTTGTTCAGAACGCTCGGTTGCCGCCGGGCGTTTTTTATTGGTGAGAATCCAAGCT

AGCTTGGCGAGATTTTCAGGAGCTAAGGAAGCTAAAATGGAGAAAAAAATCACTGG

ATATACCACCGTTGATATATCCCAATGGCATCGTAAAGAACATTTTGAGGCATTTCA

GTCAGTTGCTCAATGTACCTATAACCAGACCGTTCAGCTGGATATTACGGCCTTTTTA

AAGACCGTAAAGAAAAATAAGCACAAGTTTTATCCGGCCTTTATTCACATTCTTGCC

CGCCTGATGAATGCTCATCCGGAATTTCGTATGGCAATGAAAGACGGTGAGCTGGTG

ATATGGGATAGTGTTCACCCTTGTTACACCGTTTTCCATGAGCAAACTGAAACGTTTT

CATCGCTCTGGAGTGAATACCACGACGATTTCCGGCAGTTTCTACACATATATTCGC

AAGATGTGGCGTGTTACGGTGAAAACCTGGCCTATTTCCCTAAAGGGTTTATTGAGA

ATATGTTTTTCGTCTCAGCCAATCCCTGGGTGAGTTTCACCAGTTTTGATTTAAACGT

GGCCAATATGGACAACTTCTTCGCCCCCGTTTTCACCATGCATGGGCAAATATTATA

CGCAAGGCGACAAGGTGCTGATGCCGCTGGCGATTCAGGTTCATCATGCCGTCTGTG

ATGGCTTCCATGTCGGCAGAATGCTTAATGAATTACAACAGTACTGCGATGAGTGGC

AGGGCGGGGCGTAATTTTTTTAAGGCAGTTATTGGTGCCCTTAAACGCCTGGGGTAA

TGACTCTCTAGCTTGAGGCATCAAATAAAACGAAAGGCTCAGTCGAAAGACTGGGC

CTTTCGTTTTATCTGTTGTTTGTCGGTGAACGCTCTCCTGAGTAGGACAAATCCGCCG

CTCTAGAGCTGCCTCGCGCGTTTCGGTGATGACGGTGAAAACCTCTGACACATGCAG

CTCCCGGAGACGGTCACAGCTTGTCTGTAAGCGGATGCCGGGAGCAGACAAGCCCG

TCAGGGCGCGTCAGCGGGTGTTGGCGGGTGTCGGGGCGCAGCCATGACCCAGTCAC

GTAGCGATAGCGGAGTGTATACTGGCTTAACTATGCGGCATCAGAGCAGATTGTACT

GAGAGTGCACCATATGCGGTGTGAAATACCGCACAGATGCGTAAGGAGAAAATACC

GCATCAGGCGCTCTTCCGCTTCCTCGCTCACTGACTCGCTGCGCTCGGTCGTTCGGCT

GCGGCGAGCGGTATCAGCTCACTCAAAGGCGGTAATACGGTTATCCACAGAATCAG

GGGATAACGCAGGAAAGAACATGTGAGCAAAAGGCCAGCAAAAGGCCAGGAACCG

TAAAAAGGCCGCGTTGCTGGCGTTTTTCCATAGGCTCCGCCCCCCTGACGAGCATCA

CAAAAATCGACGCTCAAGTCAGAGGTGGCGAAACCCGACAGGACTATAAAGATACC

AGGCGTTTCCCCCTGGAAGCTCCCTCGTGCGCTCTCCTGTTCCGACCCTGCCGCTTAC

CGGATACCTGTCCGCCTTTCTCCCTTCGGGAAGCGTGGCGCTTTCTCATAGCTCACGC

TGTAGGTATCTCAGTTCGGTGTAGGTCGTTCGCTCCAAGCTGGGCTGTGTGCACGAA

CCCCCCGTTCAGCCCGACCGCTGCGCCTTATCCGGTAACTATCGTCTTGAGTCCAAC

CCGGTAAGACACGACTTATCGCCACTGGCAGCAGCCACTGGTAACAGGATTAGCAG

AGCGAGGTATGTAGGCGGTGCTACAGAGTTCTTGAAGTGGTGGCCTAACTACGGCT

ACACTAGAAGGACAGTATTTGGTATCTGCGCTCTGCTGAAGCCAGTTACCTTCGGAA

AAAGAGTTGGTAGCTCTTGATCCGGCAAACAAACCACCGCTGGTAGCGGTGGTTTTT

TTGTTTGCAAGCAGCAGATTACGCGCAGAAAAAAAGGATCTCAAGAAGATCCTTTG

ATCTTTTCTACGGGGTCTGACGCTCAGTGGAACGAAAACTCACGTTAAGGGATTTTG

GTCATGAGATTATCAAAAAGGATCTTCACCTAGATCCTTTTAAATTAAAAATGAAGT

TTTAAATCAATCTAAAGTATATATGAGTAAACTTGGTCTGACAGTTACCAATGCTTA

ATCAGTGAGGCACCTATCTCAGCGATCTGTCTATTTCGTTCATCCATAGTTGCCTGAC

TCCCCGTCGTGTAGATAACTACGATACGGGAGGGCTTACCATCTGGCCCCAGTGCTG

CAATGATACCGCGAGACCCACGCTCACCGGCTCCAGATTTATCAGCAATAAACCAG

CCAGCCGGAAGGGCCGAGCGCAGAAGTGGTCCTGCAACTTTATCCGCCTCCATCCA

GTCTATTAATTGTTGCCGGGAAGCTAGAGTAAGTAGTTCGCCAGTTAATAGTTTGCG

CAACGTTGTTGCCATTGCTACAGGCATCGTGGTGTCACGCTCGTCGTTTGGTATGGCT

TCATTCAGCTCCGGTTCCCAACGATCAAGGCGAGTTACATGATCCCCCATGTTGTGC

AAAAAAGCGGTTAGCTCCTTCGGTCCTCCGATCGTTGTCAGAAGTAAGTTGGCCGCA

GTGTTATCACTCATGGTTATGGCAGCACTGCATAATTCTCTTACTGTCATGCCATCCG

TAAGATGCTTTTCTGTGACTGGTGAGTACTCAACCAAGTCATTCTGAGAATAGTGTA

TGCGGCGACCGAGTTGCTCTTGCCCGGCGTCAATACGGGATAATACCGCGCCACATA

GCAGAACTTTAAAAGTGCTCATCATTGGAAAACGTTCTTCGGGGCGAAAACTCTCAA

GGATCTTACCGCTGTTGAGATCCAGTTCGATGTAACCCACTCGTGCACCCAACTGAT

CTTCAGCATCTTTTACTTTCACCAGCGTTTCTGGGTGAGCAAAAACAGGAAGGCAAA

ATGCCGCAAAAAAGGGAATAAGGGCGACACGGAAATGTTGAATACTCATACTCTTC

CTTTTTCAATATTATTGAAGCATTTATCAGGGTTATTGTCTCATGAGCGGATACATAT

TTGAATGTATTTAGAAAAATAAACAAATAGGGGTTCCGCGCACATTTCCCCGAAAA

GTGCCACCTGACGTCTAAGAAACCATTATTATCATGACATTAACCTATAAAAATAGG

CGTATCACGAGGCCCTTTCGTCTTCAC

C.3 pQE60-CFP-NasT/NasS-YFP

Plasmid Map

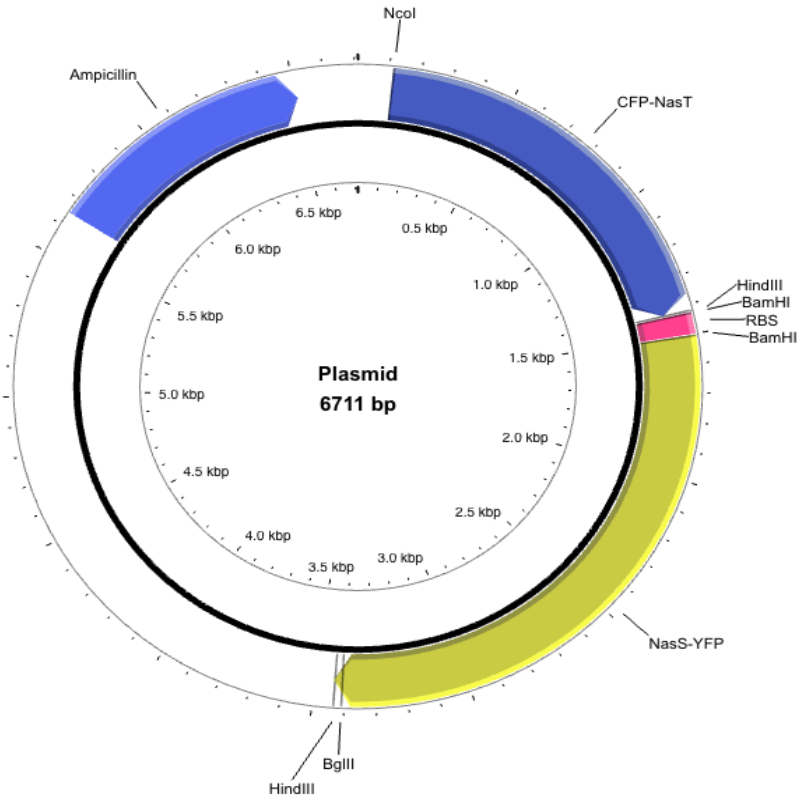

Appendix Figure C.3 Plasmid map of pQE60-CFP-NasT/NasS-YFP

DNA sequence

CTCGAGAAATCATAAAAAATTTATTTGCTTTGTGAGCGGATAACAATTATAATAGAT

TCAATTGTGAGCGGATAACAATTTCACACAGAATTCATTAAAGAGGAGAAATTAAC

CATGGTGTCAAAAGGAGAAGAGCTATTTGGGGGGATCGTGCCGATCCTGGTTGAAT

TAGAGGGCGATGTCAACGGCCACAAATTCAGCGTGTCCGGTGAAGGCGAGGGCGAC

GCTACCTATGGTAAACTGACGCTGAAGTTCATTTGCACGACCGGTAAATTGCCAGTT

CCGTGGCCGACCCTGGTCACCACCTTGACCTGGGGTGTTCAATGTTTTAGTCGCTATC

CGGACCACATGAAACAGCACGATTTTTTCAAGAGCGTTATGCCGGAGGGCTACGTA

CAAGAGAGAACAATTTTTTTCAAGGATGATGGCAACTACAAGACCCGTGCGGAAGT

GAAGTTCGAAGGTGATACCTTAGTTAATCGTATCGAATTGAAGGGCATCGACTTCAA

GGAGGACGGTAACATTCTGGGTCATAAATTGGAGTACAATTACATTAGCCATAATGT

TTATATCACCGCGGATAAACAAAAAAACGGCATTAAAGCGAATTTTAAGGCGCGTC

ATAACATCACTGACGGCAGCGTCCAACTGGCTGATCACTACCAGCAGAACACCCCG

ATCGGTGATGGTCCAGTGATCCTGCCGGACAACCACTACCTGAGCACCCAGTCCAA

GTTGTCCAAGGACCCGAATGAAAAGCGCGACCACATGGTTCTGTTGGAGTTCGTGAC

TGCGGCGGGTATCACGCATGGTATGGACGAACTGTATAAAATGAGCGCCGAACAGA

GCCCTAAAATTGTGATCGTGGACGAGAGCCCGATTAGAGCTGCAATCTTGGAGGAG

GGCCTGCGCGAAGCCGGTTTTACCCAAGTTGCACATATCCGCGAGATGCAGTCTCTG

TTGGCGCGTATTTATGCCGTTGACCCGGACATCATTCTGATTGACCTGGAGAACCCG

AGCCGTGACGTGCTCGAGGCAATGTTCCAGGTTTCTAGGGCGGTTCGTCGTCCGATA

GCCATGTTCGTTGATCAGTCAGATTCCGCTTCGATTCAGGCATCCGTCGAAGCGGGT

GTGAGCGCGTACATCGTGGACGGCCTTAAGAAAGAGCGCATTAAGCCGATTCTGGA

TCTTTGCGTTTCTCGTTTTAACGCGTTTGCGAAACTGCAAGAGGAGTTGGAGCGCAC

GAAATCGCAACTGGAGGATCGTAAAATCATCGAACGTGCGAAAGGTATCTTGATGA

AGGTGAAAGGTCTGACCGAAGACGAAGCCTATGTGCTGCTGCGTAGCACGGCTATG

CGTGAAAAAAAGAAGATTGGCGAAATTGCACAGTCTATTATCACCGCGAGCGAAAT

GCTGAAGAAGCTTTAAGGATCCGTCGACCTGCAGCCAATTAGCTGAGCCGGATAAC

AATTTCACACAGAATTCATTAAAGAGGAGAAATTAAGGATCCATGACAGGGCCCCT

AAGGATAGGATTTATTCCGCTGGTGGACGCAGCCGCCCTGATCGTTGCGGTAGACAA

AGGATTTACTGCGGCGGAAGGCCTGGATGTCGAGTTGGTGAGAGAAGTGAGCTGGA

GCAATGTTCGTGACAAGTTGAACATTGGCCTGTTTGATGCCGCCCATCTGCTTGCTCC

GGTGGCGATCGCCTCTTCCCTGGGTCTGGGTCACGTTAAGGTTCCGATTGCTGCTCC

ATTCAACCTGGGCATTAACGGCAACGCAATCACCGTTTCGCCGACTCTTCACGCGGC

GTTAATGGAAGAAATCGATGGCGATCGTTTTGATCCATTAGTCACCGCCAAAGCGCT

GGCGCGTGTTGTAGCTCGCCGTCGTAAATTGGGTGCTGACCCGTTGACCTTCGGTAT

GACCTTTCCGTTTAGCACCCATAATTACCAGCTGCGTTTCTGGATGGCGGCGGCAGG

TGTGGACCCGGACGAGGATGTCCGGCTGGTCGTTCTGCCTCCGCCGTATATGGTCGA

CAGCCTGGCAAACGGTCACGTGGATGCGTTCTGCGTTGGTGCGCCGTGGAATAGTAT

TGCGGTTGATCTGGGTATCGGCCACATTTTGCACTTTGTTAGCGATATCTTGGTGCAC

GCGGCTGAGAAAGTGCTGGCAGTGCGCCAGACCTGGGCAGATAAAAACCCGGATGT

TGTTGCTTCGTTGGTTCGTGCAGCCGTGAAAGCGGCGGAATTTATCGAACATCCGGA

AAATCGCATCGAAGCAGCGCGTATCTTGGCGCAGCCGGAGCGTATAGGCGTGGACG

CCGAGGTGATTCAGCGTACCCTTACCGGTAGGCTGAAGATTAGCCCGGACGGCACG

TTCCGCGAAAGCGGCCGCTATCTGCTCGTGGGCCGTGAAGGTGCGGGTCGTCCGGA

CCCGGTGCAGGCAGCGTGGCTGTATGCACAAATGGTACGTTGGGGTCAGACTGCGC

TGGCGCCGGACGGCGTTAAGACCGCGATGGCGGTCTTTCGTCCAGACCTATACGAC

GCCGCGCTGGGTTCCCGTGCGGCACCGTCTGAAGCTCCGGCTGCCTTCGGCGCATTC

GCTGGTCCGGTGTTCGATCCGGACAACATTCGTGGTCATCTTGAGGCGTTTGAGGTG

GGTCGCTGGAAAGCGCTGCCGGATAATCATTACCTGAGCTATCAAAGCGCGCTTAGC

AAGGACCCGAATGAGAAGCGCGACCACATGGTGCTGCTGGAGTTCGTGACCGCAGC

GGGGATTACCTTAGGCATGGATGAACTGTACAAGGGTGGTTCCGGCGGCATGGTTTC

CAAGGGCGAGGAACTGTTCACCGGTGTGGTGCCGATCCTCGTAGAGCTGGATGGTG

ATGTGAACGGCCACAAATTCTCCGTGTCTGGTGAAGGCGAAGGCGACGCGACGTAC

GGCAAACTGACGCTGAAACTCATCTGCACCACAGGTAAATTGCCAGTGCCGTGGCC

TACGCTGGTGACCACGTTGGGTTATGGTCTGCAGTGTTTTGCTCGTTACCCGGACCAT

ATGAAACAACATGATTTCTTCAAGAGCGCTATGCCGGAGGGCTATGTTCAAGAAAG

AACAATTTTTTTTAAAGATGATGGTAATTACAAAACCCGTGCGGAGGTTAAGTTCGA

GGGCGATACCCTCGTCAACCGCATTGAGCTGAAGGGCATCGACTTCAAAGAAGATG

GCAACATCTTGGGCCACAAGTTGGAGTATAACTACAATTCACATAACGTTTACATCA

CCGCTGACAAGCAGAAAAACGGCATTAAGGCGAACTTTAAGATCCGCCACAACATC

GAGGACGGAGGTGTTCAGCTGGCCGACCACTACCAACAAAACACCCCGATCGGGGA

CGGTCCGGTTCTGAGATCTCATCACCATCACCATCACTAAGCTTAATTAGCTGAGCT

TGGACTCCTGTTGATAGATCCAGTAATGACCTCAGAACTCCATCTGGATTTGTTCAG

AACGCTCGGTTGCCGCCGGGCGTTTTTTATTGGTGAGAATCCAAGCTAGCTTGGCGA

GATTTTCAGGAGCTAAGGAAGCTAAAATGGAGAAAAAAATCACTGGATATACCACC

GTTGATATATCCCAATGGCATCGTAAAGAACATTTTGAGGCATTTCAGTCAGTTGCT

CAATGTACCTATAACCAGACCGTTCAGCTGGATATTACGGCCTTTTTAAAGACCGTA

AAGAAAAATAAGCACAAGTTTTATCCGGCCTTTATTCACATTCTTGCCCGCCTGATG

AATGCTCATCCGGAATTTCGTATGGCAATGAAAGACGGTGAGCTGGTGATATGGGA

TAGTGTTCACCCTTGTTACACCGTTTTCCATGAGCAAACTGAAACGTTTTCATCGCTC

TGGAGTGAATACCACGACGATTTCCGGCAGTTTCTACACATATATTCGCAAGATGTG

GCGTGTTACGGTGAAAACCTGGCCTATTTCCCTAAAGGGTTTATTGAGAATATGTTT

TTCGTCTCAGCCAATCCCTGGGTGAGTTTCACCAGTTTTGATTTAAACGTGGCCAATA

TGGACAACTTCTTCGCCCCCGTTTTCACCATGCATGGGCAAATATTATACGCAAGGC

GACAAGGTGCTGATGCCGCTGGCGATTCAGGTTCATCATGCCGTCTGTGATGGCTTC

CATGTCGGCAGAATGCTTAATGAATTACAACAGTACTGCGATGAGTGGCAGGGCGG

GGCGTAATTTTTTTAAGGCAGTTATTGGTGCCCTTAAACGCCTGGGGTAATGACTCT

CTAGCTTGAGGCATCAAATAAAACGAAAGGCTCAGTCGAAAGACTGGGCCTTTCGT

TTTATCTGTTGTTTGTCGGTGAACGCTCTCCTGAGTAGGACAAATCCGCCGCTCTAGA

GCTGCCTCGCGCGTTTCGGTGATGACGGTGAAAACCTCTGACACATGCAGCTCCCGG

AGACGGTCACAGCTTGTCTGTAAGCGGATGCCGGGAGCAGACAAGCCCGTCAGGGC

GCGTCAGCGGGTGTTGGCGGGTGTCGGGGCGCAGCCATGACCCAGTCACGTAGCGA

TAGCGGAGTGTATACTGGCTTAACTATGCGGCATCAGAGCAGATTGTACTGAGAGTG

CACCATATGCGGTGTGAAATACCGCACAGATGCGTAAGGAGAAAATACCGCATCAG

GCGCTCTTCCGCTTCCTCGCTCACTGACTCGCTGCGCTCGGTCGTTCGGCTGCGGCGA

GCGGTATCAGCTCACTCAAAGGCGGTAATACGGTTATCCACAGAATCAGGGGATAA

CGCAGGAAAGAACATGTGAGCAAAAGGCCAGCAAAAGGCCAGGAACCGTAAAAAG

GCCGCGTTGCTGGCGTTTTTCCATAGGCTCCGCCCCCCTGACGAGCATCACAAAAAT

CGACGCTCAAGTCAGAGGTGGCGAAACCCGACAGGACTATAAAGATACCAGGCGTT

TCCCCCTGGAAGCTCCCTCGTGCGCTCTCCTGTTCCGACCCTGCCGCTTACCGGATAC

CTGTCCGCCTTTCTCCCTTCGGGAAGCGTGGCGCTTTCTCATAGCTCACGCTGTAGGT

ATCTCAGTTCGGTGTAGGTCGTTCGCTCCAAGCTGGGCTGTGTGCACGAACCCCCCG

TTCAGCCCGACCGCTGCGCCTTATCCGGTAACTATCGTCTTGAGTCCAACCCGGTAA

GACACGACTTATCGCCACTGGCAGCAGCCACTGGTAACAGGATTAGCAGAGCGAGG

TATGTAGGCGGTGCTACAGAGTTCTTGAAGTGGTGGCCTAACTACGGCTACACTAGA

AGGACAGTATTTGGTATCTGCGCTCTGCTGAAGCCAGTTACCTTCGGAAAAAGAGTT

GGTAGCTCTTGATCCGGCAAACAAACCACCGCTGGTAGCGGTGGTTTTTTTGTTTGC

AAGCAGCAGATTACGCGCAGAAAAAAAGGATCTCAAGAAGATCCTTTGATCTTTTCT

ACGGGGTCTGACGCTCAGTGGAACGAAAACTCACGTTAAGGGATTTTGGTCATGAG

ATTATCAAAAAGGATCTTCACCTAGATCCTTTTAAATTAAAAATGAAGTTTTAAATC

AATCTAAAGTATATATGAGTAAACTTGGTCTGACAGTTACCAATGCTTAATCAGTGA

GGCACCTATCTCAGCGATCTGTCTATTTCGTTCATCCATAGTTGCCTGACTCCCCGTC

GTGTAGATAACTACGATACGGGAGGGCTTACCATCTGGCCCCAGTGCTGCAATGATA

CCGCGAGACCCACGCTCACCGGCTCCAGATTTATCAGCAATAAACCAGCCAGCCGG

AAGGGCCGAGCGCAGAAGTGGTCCTGCAACTTTATCCGCCTCCATCCAGTCTATTAA

TTGTTGCCGGGAAGCTAGAGTAAGTAGTTCGCCAGTTAATAGTTTGCGCAACGTTGT

TGCCATTGCTACAGGCATCGTGGTGTCACGCTCGTCGTTTGGTATGGCTTCATTCAGC

TCCGGTTCCCAACGATCAAGGCGAGTTACATGATCCCCCATGTTGTGCAAAAAAGCG

GTTAGCTCCTTCGGTCCTCCGATCGTTGTCAGAAGTAAGTTGGCCGCAGTGTTATCA

CTCATGGTTATGGCAGCACTGCATAATTCTCTTACTGTCATGCCATCCGTAAGATGCT

TTTCTGTGACTGGTGAGTACTCAACCAAGTCATTCTGAGAATAGTGTATGCGGCGAC

CGAGTTGCTCTTGCCCGGCGTCAATACGGGATAATACCGCGCCACATAGCAGAACTT

TAAAAGTGCTCATCATTGGAAAACGTTCTTCGGGGCGAAAACTCTCAAGGATCTTAC

CGCTGTTGAGATCCAGTTCGATGTAACCCACTCGTGCACCCAACTGATCTTCAGCAT

CTTTTACTTTCACCAGCGTTTCTGGGTGAGCAAAAACAGGAAGGCAAAATGCCGCAA

AAAAGGGAATAAGGGCGACACGGAAATGTTGAATACTCATACTCTTCCTTTTTCAAT

ATTATTGAAGCATTTATCAGGGTTATTGTCTCATGAGCGGATACATATTTGAATGTAT

TTAGAAAAATAAACAAATAGGGGTTCCGCGCACATTTCCCCGAAAAGTGCCACCTG

ACGTCTAAGAAACCATTATTATCATGACATTAACCTATAAAAATAGGCGTATCACGA

GGCCCTTTCGTCTTCAC

C.4.pQE60-CFP-NasS-YFP (CNasSY)

Plasmid map

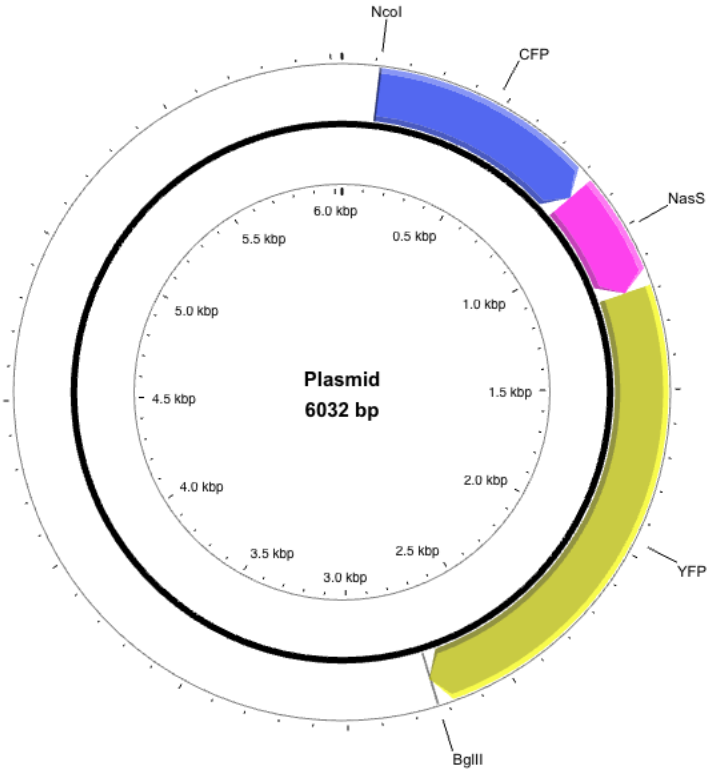

Appendix Figure C.4 Plasmid map of pQE60-CFP-NasS-YFP

DNA sequence

CTCGAGAAATCATAAAAAATTTATTTGCTTTGTGAGCGGATAACAATTATAATAGAT
TCAATTGTGAGCGGATAACAATTTCACACAGAATTCATTAAAGAGGAGAAATTAAC
CATGGTGTCAAAAGGAGAAGAGCTATTTGGGGGGATCGTGCCGATCCTGGTTGAAT
TAGAGGGCGATGTCAACGGCCACAAATTCAGCGTGTCCGGTGAAGGCGAGGGCGAC
GCTACCTATGGTAAACTGACGCTGAAGTTCATTTGCACGACCGGTAAATTGCCAGTT
CCGTGGCCGACCCTGGTCACCACCTTGACCTGGGGTGTTCAATGTTTTAGTCGCTATC
CGGACCACATGAAACAGCACGATTTTTTCAAGAGCGTTATGCCGGAGGGCTACGTA
CAAGAGAGAACAATTTTTTTCAAGGATGATGGCAACTACAAGACCCGTGCGGAAGT

GAAGTTCGAAGGTGATACCTTAGTTAATCGTATCGAATTGAAGGGCATCGACTTCAA
GGAGGACGGTAACATTCTGGGTCATAAATTGGAGTACAATTACATTAGCCATAATGT
TTATATCACCGCGGATAAACAAAAAAACGGCATTAAAGCGAATTTTAAGGCGCGTC
ATAACATCACTGACGGCAGCGTCCAACTGGCTGATCACTACCAGCAGAACACCCCG
ATCGGTGATGGTCCAGTGATCCTGCCGGACAACCACTACCTGAGCACCCAGTCCAA
GTTGTCCAAGGACCCGAATGAAAAGCGCGACCACATGGTTCTGTTGGAGTTCGTGAC
TGCGGCGGGTATCACGCATGGTATGGACGAACTGTATAAAATGACAGGGCCCCTAA
GGATAGGATTTATTCCGCTGGTGGACGCAGCCGCCCTGATCGTTGCGGTAGACAAAG
GATTTACTGCGGCGGAAGGCCTGGATGTCGAGTTGGTGAGAGAAGTGAGCTGGAGC
AATGTTCGTGACAAGTTGAACATTGGCCTGTTTGATGCCGCCCATCTGCTTGCTCCG
GTGGCGATCGCCTCTTCCCTGGGTCTGGGTCACGTTAAGGTTCCGATTGCTGCTCCAT
TCAACCTGGGCATTAACGGCAACGCAATCACCGTTTCGCCGACTCTTCACGCGGCGT
TAATGGAAGAAATCGATGGCGATCGTTTTGATCCATTAGTCACCGCCAAAGCGCTGG
CGCGTGTTGTAGCTCGCCGTCGTAAATTGGGTGCTGACCCGTTGACCTTCGGTATGA
CCTTTCCGTTTAGCACCCATAATTACCAGCTGCGTTTCTGGATGGCGGCGGCAGGTG
TGGACCCGGACGAGGATGTCCGGCTGGTCGTTCTGCCTCCGCCGTATATGGTCGACA
GCCTGGCAAACGGTCACGTGGATGCGTTCTGCGTTGGTGCGCCGTGGAATAGTATTG
CGGTTGATCTGGGTATCGGCCACATTTTGCACTTTGTTAGCGATATCTTGGTGCACGC
GGCTGAGAAAGTGCTGGCAGTGCGCCAGACCTGGGCAGATAAAAACCCGGATGTTG
TTGCTTCGTTGGTTCGTGCAGCCGTGAAAGCGGCGGAATTTATCGAACATCCGGAAA
ATCGCATCGAAGCAGCGCGTATCTTGGCGCAGCCGGAGCGTATAGGCGTGGACGCC
GAGGTGATTCAGCGTACCCTTACCGGTAGGCTGAAGATTAGCCCGGACGGCACGTTC
CGCGAAAGCGGCCGCTATCTGCTCGTGGGCCGTGAAGGTGCGGGTCGTCCGGACCC
GGTGCAGGCAGCGTGGCTGTATGCACAAATGGTACGTTGGGGTCAGACTGCGCTGG
CGCCGGACGGCGTTAAGACCGCGATGGCGGTCTTTCGTCCAGACCTATACGACGCC
GCGCTGGGTTCCCGTGCGGCACCGTCTGAAGCTCCGGCTGCCTTCGGCGCATTCGCT
GGTCCGGTGTTCGATCCGGACAACATTCGTGGTCATCTTGAGGCGTTTGAGGTGGGT
CGCTGGAAAGCGCTGCCGGATAATCATTACCTGAGCTATCAAAGCGCGCTTAGCAA
GGACCCGAATGAGAAGCGCGACCACATGGTGCTGCTGGAGTTCGTGACCGCAGCGG
GGATTACCTTAGGCATGGATGAACTGTACAAGGGTGGTTCCGGCGGCATGGTTTCCA
AGGGCGAGGAACTGTTCACCGGTGTGGTGCCGATCCTCGTAGAGCTGGATGGTGAT

GTGAACGGCCACAAATTCTCCGTGTCTGGTGAAGGCGAAGGCGACGCGACGTACGG
CAAACTGACGCTGAAACTCATCTGCACCACAGGTAAATTGCCAGTGCCGTGGCCTAC
GCTGGTGACCACGTTGGGTTATGGTCTGCAGTGTTTTGCTCGTTACCCGGACCATAT
GAAACAACATGATTTCTTCAAGAGCGCTATGCCGGAGGGCTATGTTCAAGAAAGAA
CAATTTTTTTTAAAGATGATGGTAATTACAAAACCCGTGCGGAGGTTAAGTTCGAGG
GCGATACCCTCGTCAACCGCATTGAGCTGAAGGGCATCGACTTCAAAGAAGATGGC
AACATCTTGGGCCACAAGTTGGAGTATAACTACAATTCACATAACGTTTACATCACC
GCTGACAAGCAGAAAAACGGCATTAAGGCGAACTTTAAGATCCGCCACAACATCGA
GGACGGAGGTGTTCAGCTGGCCGACCACTACCAACAAAACACCCCGATCGGGGACG
GTCCGGTTCTGAGATCTCATCACCATCACCATCACTAAGCTTAATTAGCTGAGCTTG
GACTCCTGTTGATAGATCCAGTAATGACCTCAGAACTCCATCTGGATTTGTTCAGAA
CGCTCGGTTGCCGCCGGGCGTTTTTTATTGGTGAGAATCCAAGCTAGCTTGGCGAGA
TTTTCAGGAGCTAAGGAAGCTAAAATGGAGAAAAAAATCACTGGATATACCACCGT
TGATATATCCCAATGGCATCGTAAAGAACATTTTGAGGCATTTCAGTCAGTTGCTCA
ATGTACCTATAACCAGACCGTTCAGCTGGATATTACGGCCTTTTTAAAGACCGTAAA
GAAAAATAAGCACAAGTTTTATCCGGCCTTTATTCACATTCTTGCCCGCCTGATGAA
TGCTCATCCGGAATTTCGTATGGCAATGAAAGACGGTGAGCTGGTGATATGGGATA
GTGTTCACCCTTGTTACACCGTTTTCCATGAGCAAACTGAAACGTTTTCATCGCTCTG
GAGTGAATACCACGACGATTTCCGGCAGTTTCTACACATATATTCGCAAGATGTGGC
GTGTTACGGTGAAAACCTGGCCTATTTCCCTAAAGGGTTTATTGAGAATATGTTTTTC
GTCTCAGCCAATCCCTGGGTGAGTTTCACCAGTTTTGATTTAAACGTGGCCAATATG
GACAACTTCTTCGCCCCCGTTTTCACCATGCATGGGCAAATATTATACGCAAGGCGA
CAAGGTGCTGATGCCGCTGGCGATTCAGGTTCATCATGCCGTCTGTGATGGCTTCCA
TGTCGGCAGAATGCTTAATGAATTACAACAGTACTGCGATGAGTGGCAGGGCGGGG
CGTAATTTTTTTAAGGCAGTTATTGGTGCCCTTAAACGCCTGGGGTAATGACTCTCTA
GCTTGAGGCATCAAATAAAACGAAAGGCTCAGTCGAAAGACTGGGCCTTTCGTTTTA
TCTGTTGTTTGTCGGTGAACGCTCTCCTGAGTAGGACAAATCCGCCGCTCTAGAGCT
GCCTCGCGCGTTTCGGTGATGACGGTGAAAACCTCTGACACATGCAGCTCCCGGAG
ACGGTCACAGCTTGTCTGTAAGCGGATGCCGGGAGCAGACAAGCCCGTCAGGGCGC
GTCAGCGGGTGTTGGCGGGTGTCGGGGCGCAGCCATGACCCAGTCACGTAGCGATA
GCGGAGTGTATACTGGCTTAACTATGCGGCATCAGAGCAGATTGTACTGAGAGTGC

ACCATATGCGGTGTGAAATACCGCACAGATGCGTAAGGAGAAAATACCGCATCAGG
CGCTCTTCCGCTTCCTCGCTCACTGACTCGCTGCGCTCGGTCGTTCGGCTGCGGCGAG
CGGTATCAGCTCACTCAAAGGCGGTAATACGGTTATCCACAGAATCAGGGGATAAC
GCAGGAAAGAACATGTGAGCAAAAGGCCAGCAAAAGGCCAGGAACCGTAAAAAGG
CCGCGTTGCTGGCGTTTTTCCATAGGCTCCGCCCCCCTGACGAGCATCACAAAAATC
GACGCTCAAGTCAGAGGTGGCGAAACCCGACAGGACTATAAAGATACCAGGCGTTT
CCCCCTGGAAGCTCCCTCGTGCGCTCTCCTGTTCCGACCCTGCCGCTTACCGGATACC
TGTCCGCCTTTCTCCCTTCGGGAAGCGTGGCGCTTTCTCATAGCTCACGCTGTAGGTA
TCTCAGTTCGGTGTAGGTCGTTCGCTCCAAGCTGGGCTGTGTGCACGAACCCCCCGT
TCAGCCCGACCGCTGCGCCTTATCCGGTAACTATCGTCTTGAGTCCAACCCGGTAAG
ACACGACTTATCGCCACTGGCAGCAGCCACTGGTAACAGGATTAGCAGAGCGAGGT
ATGTAGGCGGTGCTACAGAGTTCTTGAAGTGGTGGCCTAACTACGGCTACACTAGAA
GGACAGTATTTGGTATCTGCGCTCTGCTGAAGCCAGTTACCTTCGGAAAAAGAGTTG
GTAGCTCTTGATCCGGCAAACAAACCACCGCTGGTAGCGGTGGTTTTTTTGTTTGCA
AGCAGCAGATTACGCGCAGAAAAAAAGGATCTCAAGAAGATCCTTTGATCTTTTCTA
CGGGGTCTGACGCTCAGTGGAACGAAAACTCACGTTAAGGGATTTTGGTCATGAGA
TTATCAAAAAGGATCTTCACCTAGATCCTTTTAAATTAAAAATGAAGTTTTAAATCA
ATCTAAAGTATATATGAGTAAACTTGGTCTGACAGTTACCAATGCTTAATCAGTGAG
GCACCTATCTCAGCGATCTGTCTATTTCGTTCATCCATAGTTGCCTGACTCCCCGTCG
TGTAGATAACTACGATACGGGAGGGCTTACCATCTGGCCCCAGTGCTGCAATGATAC
CGCGAGACCCACGCTCACCGGCTCCAGATTTATCAGCAATAAACCAGCCAGCCGGA
AGGGCCGAGCGCAGAAGTGGTCCTGCAACTTTATCCGCCTCCATCCAGTCTATTAAT
TGTTGCCGGGAAGCTAGAGTAAGTAGTTCGCCAGTTAATAGTTTGCGCAACGTTGTT
GCCATTGCTACAGGCATCGTGGTGTCACGCTCGTCGTTTGGTATGGCTTCATTCAGCT
CCGGTTCCCAACGATCAAGGCGAGTTACATGATCCCCCATGTTGTGCAAAAAAGCG
GTTAGCTCCTTCGGTCCTCCGATCGTTGTCAGAAGTAAGTTGGCCGCAGTGTTATCA
CTCATGGTTATGGCAGCACTGCATAATTCTCTTACTGTCATGCCATCCGTAAGATGCT
TTTCTGTGACTGGTGAGTACTCAACCAAGTCATTCTGAGAATAGTGTATGCGGCGAC
CGAGTTGCTCTTGCCCGGCGTCAATACGGGATAATACCGCGCCACATAGCAGAACTT
TAAAAGTGCTCATCATTGGAAAACGTTCTTCGGGGCGAAAACTCTCAAGGATCTTAC
CGCTGTTGAGATCCAGTTCGATGTAACCCACTCGTGCACCCAACTGATCTTCAGCAT

CTTTTACTTTCACCAGCGTTTCTGGGTGAGCAAAAACAGGAAGGCAAAATGCCGCAA
AAAAGGGAATAAGGGCGACACGGAAATGTTGAATACTCATACTCTTCCTTTTTCAAT
ATTATTGAAGCATTTATCAGGGTTATTGTCTCATGAGCGGATACATATTTGAATGTAT
TTAGAAAAATAAACAAATAGGGGTTCCGCGCACATTTCCCCGAAAAGTGCCACCTG
ACGTCTAAGAAACCATTATTATCATGACATTAACCTATAAAAATAGGCGTATCACGA
GGCCCTTTCGTCTTCAC